Tunning cation occupancy in $MgFe_2O_4$ spinel and effect of interfacial voltage drop on catalytic efficiency in photoelectrochemical water splitting

Doctoral thesis

for

the award of the doctoral degree

of the Faculty of Mathematics and Natural Sciences

of the University of Cologne

submitted by

Hyeonkwon Lee

accepted in the year 2026

Abstract

Applying an external magnetic field during chemical vapor deposition of thin films can induce texturing effects that are beneficial in photoelectrochemical (PEC) water splitting. In this work, thin films of $MgFe_2O_4$ spinel were grown in a chemical vapor deposition (CVD) reactor operating under external magnetic field (0 – 1 T). The X-ray diffraction analyses suggested that the degree of inversion (structural disorder due to movement of cations from tetrahedral into octahedral holes) in $MgFe_2O_4$ can be controlled by varying the magnetic field intensity during CVD. The $MgFe_2O_4$ films with a normal spinel configuration show a broader absorption range in the UV-visible spectra compared to the inverse counterpart, indicating the potential tunability of degree of inversion for enhanced PEC water splitting performance.

Despite extensive efforts to develop efficient photocatalysts by structural and compositional modulations, evaluation frameworks for PEC water splitting primarily rely on current-based parameters, such as the onset potential and current density at 1.23 V versus the reversible hydrogen electrode. Functional performance in PEC water splitting is typically evaluated using current density. However, such measurements often underestimate activity due to voltage losses arising from resistances (iR) within the PEC cell, compounded by the absence of standardized iR compensation protocols. In this work, the voltage drops associated with charge transfer (V_{ct}) and pH gradient (V_{pH}) voltage drops at the solid/liquid interface are quantitatively analyzed as direct indicators of PEC oxygen evolution performance. While open circuit potential (OCP) decay transients have previously been employed to monitor interfacial pH changes during hydrogen evolution reaction (HER) on a platinum electrode involving two electrons, this work extends the approach to the more complex oxygen evolution reaction (OER) on an illuminated TiO_2 semiconductor photoanode involving four electrons. The individual roles of V_{ct} and V_{pH}, examined across various pH values and illumination intensities, reveal

that V_{ct} reflects intrinsic interfacial voltage loss under bias, whereas V_{pH} serves as a complementary descriptor to photocurrent density for evaluating catalytic activity in PEC systems.

This work demonstrates that the degree of inversion in $MgFe_2O_4$ can be systematically tuned by applying an external magnetic field, thereby linking cation disorder to improved spectral response. In addition, the quantitative evaluation V_{ct} and V_{pH} provides a diagnostic framework for assessing catalytic efficiencies beyond conventional current-based parameters, thus offering practical guidelines for the rational design and optimization of high performance PEC water splitting systems.

Table of Contents

1. Introduction **1**

1.1. Overview of photoelectrochemical (PEC) water splitting 1

1.2. Degree of inversion in oxide spinels 14

1.3. Underestimated Current-based parameters by voltage losses 15

1.4. pH-gradient voltagedrop (V_{pH}) as a direct indicator for water splitting 18

1.5. State-of-the-art for V_{pH} measurenemts 19

2. Theoretical background **22**

2.1. Semiconductor and electrolyte interface in PEC water splitting 22

2.2. Charge transfer at the semiconductor/electrolyte interface 24

2.3. Current-voltage characteristics representing PEC water splitting 32

2.4. Low frequency capacitance 36

2.5. Voltage drop formation at the semiconductor/electrolyte interface 40

3. Results and discussion **45**

3.1. Controlling degree of inversion in the $MgFe_2O_4$ film 45

3.1.1. Synthesis of single source precursor for $MgFe_2O_4$ 45

3.1.2. Characterization of $MgFe_2O_4$ films grown in magnetic field-assisted chemical vapor deposition (mfCVD) 47

3.1.3. Spectroscopic investigations of the effects of magnetic field on the $MgFe_2O_4$ film 53

3.2. Interfacial voltage drop ($V_{interface}$) characteristics in non-faradaic and faradaic reactions 58

3.2.1. $V_{interface}$ in non-faradaic reaction 59

3.2.2. Time constant in discharging process 69

3.2.3. $V_{interface}$ in faradaic reaction 72

3.2.4. V_{pH} estimation in various conditions with TiO_2 photoanode 77

3.2.5. Estimation of charge transfer voltage drop (V_{ct}) and V_{pH} using WO_3 as a photoanode 83

4. Conclusions&Outlook **88**

5. Methods and materials **91**

5.1. Synthesis of $[Mg\{Fe(O^tBu)_4\}_2]$ precursor 91

5.2. magnetic field-assisted chemical vapor deposition 92

5.3. Physicochemical characterization of the $MgFe_2O_4$ films 93

5.4. Photoanodes TiO_2 and WO_3 synthesis and characterization 93

5.5. Electrochemical measurements 94

6. References **96**

1. Introduction

1.1 Overview of photoelectrochemical (PEC) water splitting

Hydrogen is widely recognized as an important energy carrier owing to its high gravimetric energy density of approximately 122 kJ g^{-1}, which is about 2.75 times higher than that of conventional hydrocarbon-based fuels.[1] Consequently, hydrogen as an energy source is necessary to meet the increasing energy consumption over year (**figure 1(a)**). Conventionally, hydrogen has been produced through several thermochemical routes, including coal gasification, partial oxidation of hydrocarbons, and steam reforming of natural gas (**figure 1(b)**).[2] These fossil fuel-based hydrogen production processes have emerged as major contributors to global warming and air pollution due to the emission of greenhouse gases such as carbon dioxide, methane, and nitrous oxide.[3]

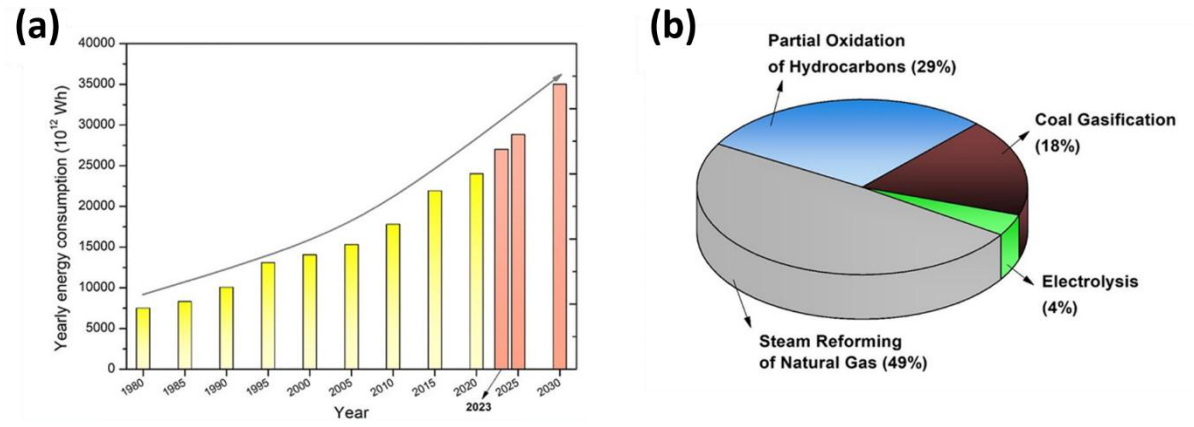

Figure 1 (a) Increasing energy consumption over year and (b) hydrogen production sources. Adapted from ref. [2].

These environmental concerns necessitate the transition from fossil fuel-derived hydrogen toward renewable and sustainable production routes. Among various alternatives, sea water

(H_2O) is considered an ideal feedstock for clean hydrogen generation, as it contains hydrogen intrinsically and is abundantly available.[4,5] Hydrogen gas is evolved when water decomposes under the application of external energy. In the case of thermal water splitting, steam must be heated to extremely high temperature (up to ~3000 °C) to achieve thermal dissociation in to H^+, H_2, O^{2-}, OH^- and O_2.[6] However, maintaining such elevated temperature makes the process energetically demanding and economically inefficient.

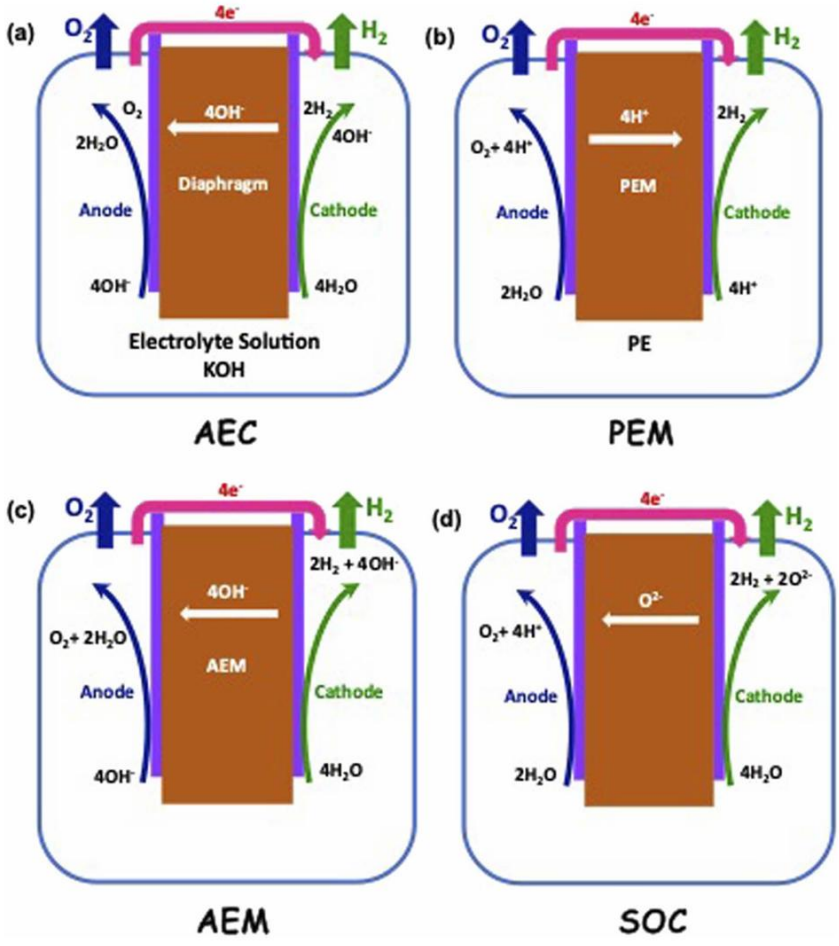

Figure 2 Schematic images of four different types of electrolysers representing (a) alkaline liquid electrolyser (AEC), (b) polymer electrolyte membrane (PEM) electrolyser, (c) anion exchange membrane (AEM) electrolyser and (d) solid oxide electrolyte (SOC) electrolyser. Adapted from ref. [6].

To overcome the high energy input required for thermochemical decomposition, water electrolysis has been explored as a more feasible alternative. Unlike thermal processes, electrolysis produces hydrogen by applying an external potential or current, typically corresponding to 1.23 V versus the normal hydrogen electrode (V_{NHE}). The fundamental half-cell reactions involved in water electrolysis are as follows.

In acidic conditions,

$$2H_2O \rightarrow O_2 + 4H^+ + 4e^- \quad (E^o = 1.23\, V_{NHE}) \qquad (1.1)$$

$$2H^+ + 2e^- \rightarrow H_2 \quad (E^o = 0\, V_{NHE}) \qquad (1.2)$$

In alkaline conditions,

$$4OH^- \rightarrow O_2 + 2H_2O + 4e^- \quad (E^o = 0.401\, V_{NHE}) \qquad (1.3)$$

$$2H_2O + 2e^- \rightarrow H_2 + 2OH^- \quad (E^o = -0.828\, V_{NHE}) \qquad (1.4)$$

There are four types of water electrolysers for the oxygen evolution reaction (OER), classified according to the nature of their electrolytes as shown in **figure 2**: alkaline liquid electrolyser (AEC), polymer electrolyte membrane (PEM) electrolyser, anion exchange membrane (AEM) electrolyser and solid oxide electrolyte (SOC) electrolyser systems.[7] The selection of a suitable electrolysis system depends on the physicochemical properties of the catalysts and their stability under specific operating conditions.

Although electrolysis represents a promising alternative to conventional fossil fuel-based hydrogen production and has been extensively investigated, it still suffers from significant overpotentials. These overpotentials arise from sluggish charge transfer kinetics resulting from sequential transfer four electrons at the electrocatalyst and electrolyte interface, thus requiring additional energy input beyond the theoretical potential of 1.23 V_{NHE} at pH 0. The issue

becomes more pronounced when using non-noble metal-based catalysts. Owing to their superior charge transfer characteristics and durability, noble metals such as Ir, Ru, Rh and Pt are preferred as electrocatalysts.[8] However, their high cost and scarcity impose limitations on the large-scale development of cost-effective electrocatalytic systems.

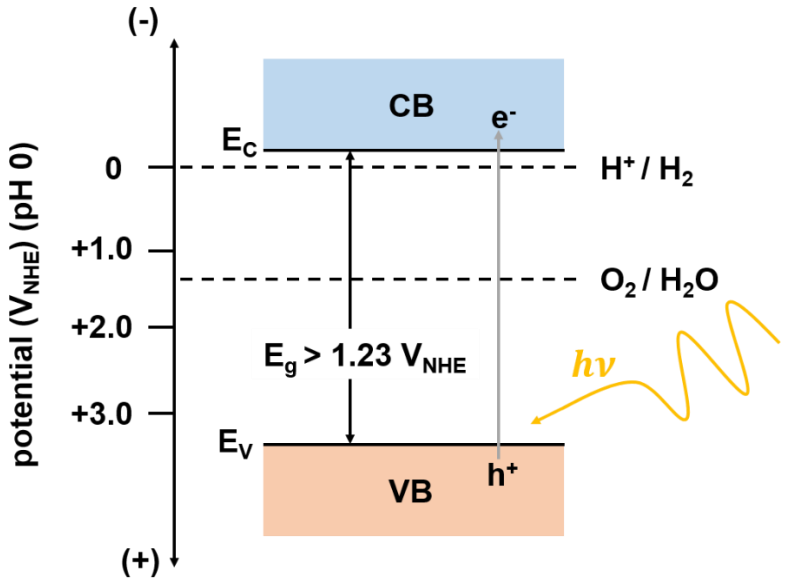

Figure 3 Energy band diagram of a semiconductor enabling photocatalytic overall water splitting (CB: conduction band, VB: valence band, E_C: electronic energy at CBM, E_V: electronic energy at VBM, E_g: band gap energy and hν: incident photon energy)

In parallel to electrocatalysis, photocatalytic water splitting has been proposed to overcome the overpotential issue in conventional electrolysis. The concept of photocatalytic overall water splitting was first demonstrated by Fujishima and honda using a TiO_2 semiconductor electrode.[9] For photo-assisted water splitting, an ideal photocatalyst is a semiconductor with an appropriate electronic band structure. Specifically, the conduction band minimum (CBM) is positioned at a potential more negative that of the hydrogen evolution reaction (HER) corresponding to $2H^+ + 2e^- \rightarrow H_2$ at 0.0 V_{NHE} (pH 0), while the valence band maximum

(VBM) is more positive than that of the OER corresponding to $2H_2O \rightarrow O_2 + 4H^+ + 4e^-$ at 1.23 V_{NHE} (pH 0) as shown in **figure 3**.

Photocatalytic overall water splitting proceeds with the following steps:

(i) The photocatalyst absorbs photon with energy hν greater than the band gap energy E_g.

(ii) Photoexcited electrons are promoted to the conduction band, leaving holes in the valence band.

(iii) The photogenerated charge carriers migrate to the semiconductor/electrolyte interface, where electrons reduce H^+ ions to form H_2 gas and holes oxidize water moelcules to produce O_2 gas.

In the early study, particulate TiO_2 photocatalysts were either immobilized on supports or dispersed in water under illumination to achieve overall water splitting.[10,11] Furthermore, oxygen vacancy formation in TiO_2 produces black TiO_2 which shows enhanced photocatalytic performances due to better light absorption and conductivity as compared to pristine TiO_2 (**figure 4**).[12]

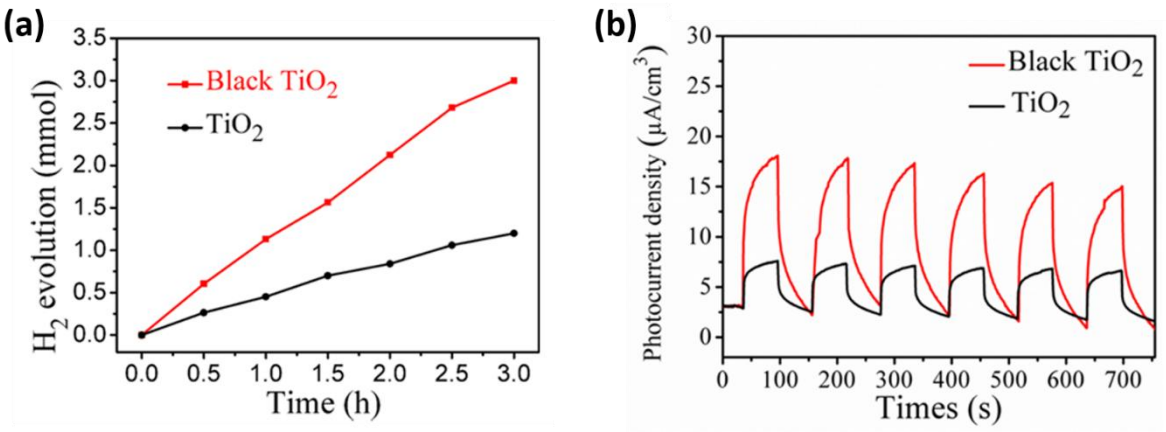

Figure 4 (a) Photocatalytic hydrogen gas evolution and (b) chronoamperometric photocurrent density of pristine TiO_2 and black TiO_2. Adapted from ref. [12].

While both hydrogen and oxygen evolution occur in this process, the OER generally dominates the reaction kinetics because it involves a complex multi-electron transfer. Consequently, the OER is considered the rate-determining step in water splitting. The reaction sequence for the OER under acidic conditions is as follows.[13]

$$H_2O + * \rightarrow OH_{ads} + H^+ + e^-, \quad (1.5)$$

$$OH_{ads} \rightarrow O_{ads} + H^+ + e^-, \quad (1.6)$$

$$O_{ads} + H_2O \rightarrow OOH_{ads} + H^+ + e^-, \quad (1.7)$$

$$OOH_{ads} \rightarrow * + O_2 + H^+ + e^-. \quad (1.8)$$

The OER process in alkaline condition follows the steps below.[8]

$$OH^- + * \rightarrow OH_{ads} + e^-, \quad (1.9)$$

$$OH_{ads} + OH^- \rightarrow O_{ads} + H_2O + e^-, \quad (1.10)$$

$$O_{ads} + OH^- \rightarrow OOH_{ads} + e^-, \quad (1.11)$$

$$OOH_{ads} + OH^- \rightarrow * + O + H_2O + e^-. \quad (1.12)$$

The symbol, $*$ denotes activated site by holes, and O_{ads}, OH_{ads} and OOH_{ads} are the adsorbed reaction intermediates on the photocatalyst surface.

The advance in OER has been a development of OER catalysts having a proper binding energy of the O_{ads} intermediate to be located at the top of the volcano plot. Yan et al. synthesized Co-doped TiO_2 decreasing the activation energies of the reaction steps (1.5) – (1.8), confirming the Co-Ti atomic arrangements provide suitable adsorption energy for oxygen intermediates.[14]

In contrast, the HER proceeds through two possible reaction pathways: the Volmer-Tafel mechanism or the Volmer-Heyrovsky mechanism,[15] which consists of combinations of each mechanism corresponding to Volmer, Heyrovsky and Tafel step.

In acidic condition,

$$\text{Volmer step: } H^+ + e^- \rightarrow H^*, \tag{1.13}$$

$$\text{Heyrovsky step: } H^* + H^+ + e^- \rightarrow H_2, \tag{1.14}$$

$$\text{Tafel step: } H^* + H^* \rightarrow H_2. \tag{1.15}$$

Whereas, in alkaline condition,

$$\text{Volmer step: } H_2O + e^- \rightarrow H^* + OH^-, \tag{1.16}$$

$$\text{Heyrovsky step: } H_2O + e^- + H^* \rightarrow H_2 + OH^-, \tag{1.17}$$

$$\text{Tafel step: } H^* + H^* \rightarrow H_2. \tag{1.18}$$

Here H^* denotes a hydrogen atom adsorbed on the catalyst surface.

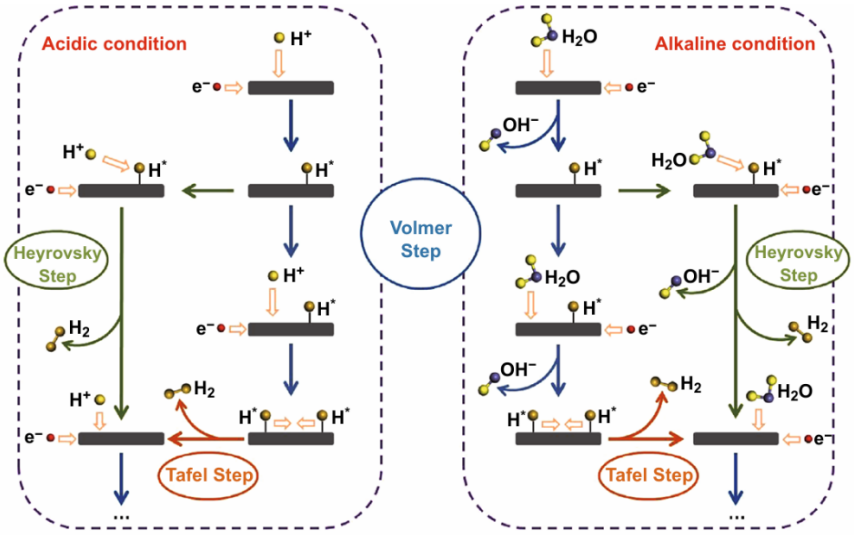

Figure 5 Schematic image representing two possible HER mechanisms corresponding to Volmer-Tafel mechanism and Volmer-Heyrovsky mechanism in acidic and alkaline conditions.

Volmer-Tafel mechanism represents initial adsorbed proton (H^+) is formed on catalyst surface by reduction and subsequently another proton is adsorbed on the surface (**figure 5**). Hydrogen gas is evolved by the bonding of the two adsorbed protons. Volmer-Heyrovsky is distinguished from the reaction after the adsorption of initial proton. Another proton coming from a water molecule is bonded to the already adsorbed proton, evolving hydrogen gas.

Because the HER involves relatively simple reaction steps, it exhibits a high exchange current density, reflecting fast kinetics and high reversibility.[16] Therefore, photocatalysts evolving OER are selectively investigated in photoelectrochemical (PEC) water splitting by employing the photocatalysts as an anode (photoanode).

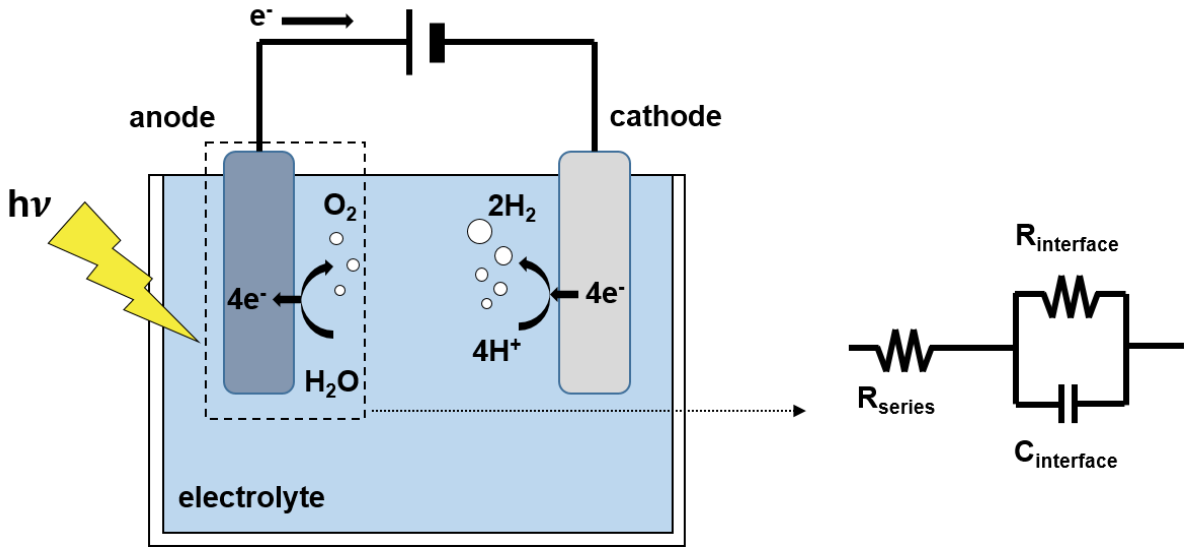

Figure 6 Schematic images of a PEC water splitting cell and an equivalent circuit representing anode and electrolyte as a Randle's circuit consisting of a series resistance (R_{series}), interfacial resistance ($R_{interface}$) and capacitance ($C_{interface}$)

A PEC water splitting cell consists of a photoanode and a counter electrode, typically platinum, connected through an external circuit and immersed in an electrolyte, as illustrated in **figure 6**. The photoanode has an electronic band structure corresponding to the schematic shown in **figure 7**.

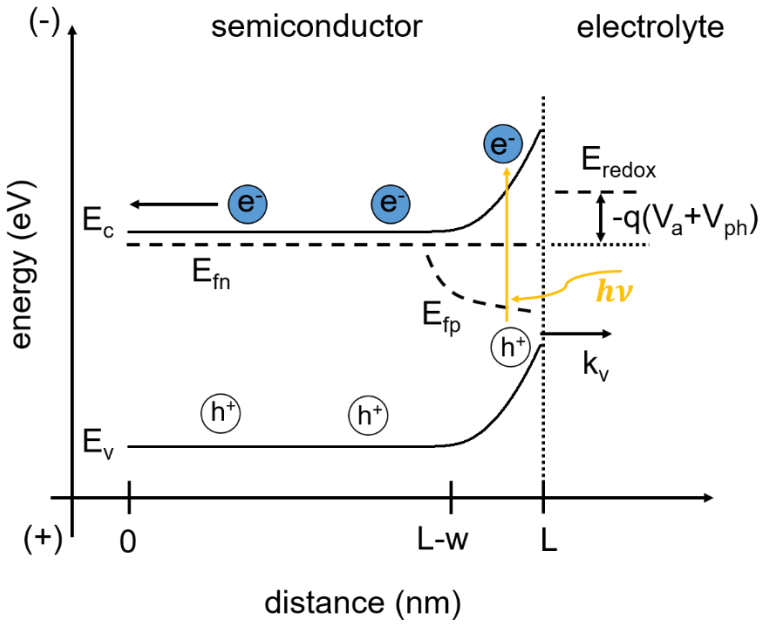

Figure 7 Energy band diagram of an n-type semiconductor in contact with electrolyte following direct hole transfer for PEC water splitting. E_c and E_v are energy levels of conduction band and valence band edge. E_{fn} and E_{fp} are quasi-electron and hole Fermi levels. E_{redox} is redox level of the electrolyte. V_a and V_{ph} are the applied voltage and photo-induced voltage. k_v is hole transfer rate at the semiconductor/electrolyte interface. q is elementary charge.

The semiconductor used as the photoanode is typically n-type, forming an ohmic junction with the back contact and a Schottky junction with the electrolyte to enable selective hole transfer. When an anodic bias is applied under sun light, photogenerated holes and electrons move

toward the semiconductor/electrolyte interface and the back contact electrode, respectively, as illustrated in **figure 7**. The electrons collected at the cathode participate in the HER, while the holes in the photoanode oxidize water molecules, driving the OER. Some examples of various types of photoanodes are introduced in table 1.

Table 1 Semiconductors used for photocatalysts

Sulfide		**Phosphide**	
Material	Ref.	Material	Ref.
CdS	[17]	CoP	[18]
MoS_2	[19]		
Nitride		**Oxide**	
Ta_3N_5	[20]	Fe_2O_3	[21]
		Co_3O_4	[22]

To enhance OER activity, photoanodes with narrow band gap that allow absorption of visible light have been investigated since the pioneering work of Fujishima and Honda on TiO_2. However, many semiconductors exhibit limited photocatalytic performance due to low conductivity and short lifetimes of photogenerated charge carriers. Corby *et al*. manipulated the density of oxygen vacancies in WO_3 films grown by chemical vapor depositing through controlled annealing time of pristine WO_3 and reported that oxygen vacancies act as dopants, improving photocurrent density.[23] Makimizu *et al.* found the optimized nanostructured α-Fe_2O_3 overcoming intrinsic life time (< 10 ps), short diffusion length (2 – 4 nm) and poor carrier mobility (10^{-2} cm^2 V^{-1} s^{-1}) by controlling annealing temperature.[24]

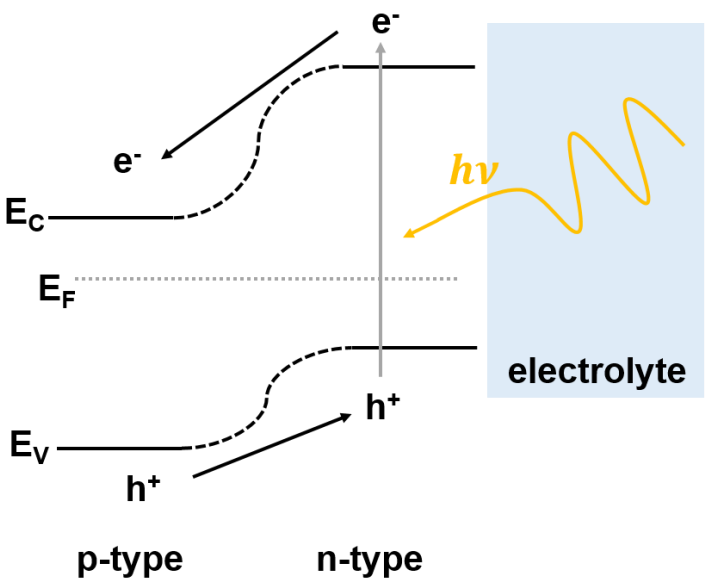

Figure 8 A schematic image of a type II heterostructure photoanode representing $WO_3/BiVO_4$ as described in ref. [25].

Another strategy to improve photoanode performance is the construction of heterostructure consisting of two semiconductors with different electronic properties, such as p-n or n-n junctions. In such heterostructures, an internal built-in electric field is generated due to band bending that arises from the alignment of Fermi levels between the two semiconductors. This built-in field at the heterojunction interface suppresses recombination of photogenerated electrons and holes, as illustrated in **figure 8**. For example, $WO_3/BiVO_4$ heterostructure has been developed to induce an internal electric field that facilitates charge separation.[26] The heterostructure also influences the onset potential, which represents the minimum external bias required to initiate water splitting. A positive shift in onset potential indicates a larger energy barrier for charge transfer. Huang *et al*. and Hatagami *et al*. performed numerical analyses on the effect of interfacial modification layers by varying parameters such as VBM energy (E_V), doping density and layer thickness, thereby elucidating the charge separation mechanism at

heterostructure interfaces.[27,28] Peter *et al*. compared onset potentials of various heterostructures by combining numerical simulations with experimental current-voltage characteristics to establish design principles for optimized HER systems.[29]

In addition to improving charge separation in $WO_3/BiVO_4$ heterostructure, passivating WO_3 overlayer protects the underlying light-absorbing $BiVO_4$ layer. While $BiVO_4$ is considered a promising photoanode material because of its narrow band gap, which enables visible light absorption. However, $BiVO_4$ suffers from V^{5+} dissociation at the semiconductor/electrolyte interface during operation.[30] For another example of a passivation layer, TiO_2 layer has been deposited as a passivation coating on $BiVO_4$ to prevent degradation due to its high chemical stability and photocatalytic activity. Park *et al*. demonstrated enhanced photocurrent density in $WO_3/BiVO_4$ heterostructure by introducing a single crystalline TiO_2 passivation layer that suppressed surface defects and improved corrosion resistance, stability, and electron transfer efficiency.[31]

Beyond the extrinsic modification of photoanodes, tunable magnetic property by external magnetic field can enhance PEC water splitting performance according to the following works. Pyeon *et al*. reported that Fe_2O_3 films deposited by magnetic field-assisted plasma chemical vapor deposition exhibited improved PEC performance, as magnetic field orientation during deposition promoted (110)-preferred growth with higher electrical conductivity.[32] Stadler *et al.* showed that magnetic field strength during chemical vapor deposition affects on-substrate nucleation and grain growth of Fe_2O_3, leading to reduced microstructural defects and enhanced charge transport and photoelectrochemically active surface area.[33]

Although previous studies have revealed how the external magnetic field influences film growth and catalytic performance, the underlying mechanisms from an electronic structure perspective remain unclear. To understand effects of the external magnetic field on PEC water

splitting at perspective of atomic arrangement, spinel ferrites (MFe_2O_4) deserve to be investigated because the spinel ferrites are thermally and chemically stable enough to be photocatalysts, and cationic disorder in spinel ferrites are quantified as degree of inversion, enabling to investigate effects of individual cation (M^{2+} and Fe^{3+}) on PEC water splitting. Particularly, $MgFe_2O_4$ has a narrow band gap energy, 1.9 eV responsive for visible light.[34]

In this work, $MgFe_2O_4$ film is synthesized by chemical vapor deposition (CVD) and external magnetic fields varying intensities at 0 – 1 T are applied during the deposition. Various X-ray spectroscopies are employed to elucidate correlation between the external magnetic field and degree of inversion in the $MgFe_2O_4$ films. The UV-vis spectra suggest that potential application of the tunable degree of inversion by an external magnetic field to PEC water splitting.

While many efforts have focused on developing efficient photocatalysts, performance evaluation in PEC systems has relied on current-based parameters. The current density in PEC water splitting reflects the reaction rate, particularly the anodic current associated with the OER at the semiconductor/electrolyte interface. However, this value is underestimated due to voltage losses arising from circuit elements within the PEC cell. Consequently, current density alone does not provide an accurate measure of catalytic efficiency. This work explains the underestimation of current density in detail. Furthermore, to more accurately assess catalytic performance, additional output parameters, specifically, the charge transfer and pH-gradient voltage drops (V_{ct} and V_{pH}, respectively) at the semiconductor/electrolyte interface, are introduced. The V_{pH}, when combined with current density, yields an interfacial output power efficiency that serves as a more comprehensive evaluation framework for PEC catalytic performance.

1.2 Degree of inversion in oxide spinels

The spinel ferrite structure consists of oxygen anions (O^{2-}) forming a face-centered cubic (FCC) lattice with two types of cations such as M^{2+} and Fe^{3+} occupying interstitial tetrahedral and octahedral sites within the lattice (**figure 9**). A key structural feature of spinel ferrites is cation disorder, quantified by the degree of inversion, which describes the exchange of M^{2+} cations from tetrahedral to octahedral sites normally occupied by Fe^{3+} in a normal spinel.[35] Because magnetic moments of tetrahedral and octahedral sites are antiparallel, degree of inversion determines net magnetic moment of spinel ferrites and consequently affects their magnetic property.

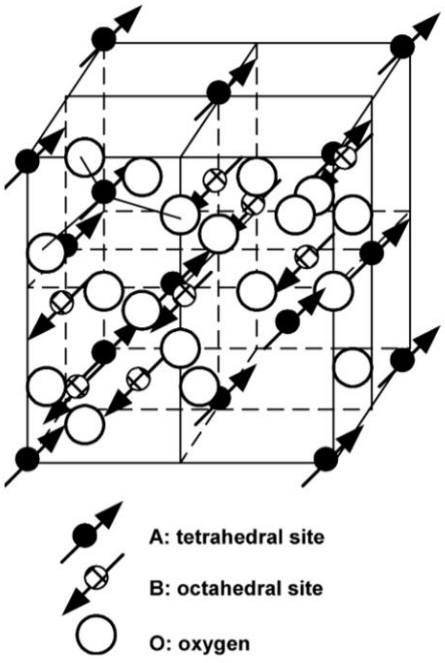

Figure 9 An unit cell of a face-centered cubic structure of oxygen atoms with tetrahedral and octahedral interstitials. Adapted from ref. [36].

The ferrimagnetic behavior and net magnetic moment of a Fe_3O_4 with ideal inverse spinel ferrite originate from antiferromagnetic coupling between Fe^{3+} ions occupying the tetrahedral and octahedral sites through bridging oxygen orbitals.[37,38] When Fe^{2+} ions at octahedral sites

partially migrate to tetrahedral sites, forming a structure closer to a normal spinel, the magnetic moments at the two sublattices partially cancel each other. $MgFe_2O_4$ is a mixed spinel ferrite with a partial degree of inversion. Because its magnetic moment arises only from Fe^{3+} ions, $MgFe_2O_4$ exhibits ferrimagnetic behavior with a relatively low degree of inversion. The degree of inversion strongly depends on the nature of the precursors and the processing conditions during synthesis, and reported values for the degree of inversion range broadly between 0.1 and 0.9.[39]

Zhu *et al.* reported that a higher degree of inversion in $ZnFe_2O_4$ spinel yields greater photocurrent than a lower degree of inversion, attributing this behavior to cationic disorder that generates a net magnetic moment and thereby enhances electrical conductivity.[40] Thus, the degree of inversion in spinel ferrites is a critical parameter for optimizing photocatalytic performance. While many spinel ferrites adopt either normal or inverse spinel structures in their thermodynamically stable states, $MgFe_2O_4$ naturally forms a mixed spinel configuration, allowing its degree of inversion to be tuned through synthetic conditions for specific functional purposes.[41]

Previous studies have shown that an external magnetic field can act as an additional synthetic parameter during chemical vapor deposition (CVD), with field-assisted growth yielding textured Fe_2O_3 films.[32,33] In a similar manner, $MgFe_2O_4$ films in this work were deposited under external magnetic fields ranging from 0 to 1 T. The influence of the magnetic field on the degree of inversion was subsequently examined through spectroscopic analyses.

1.3 Underestimated current-based parameters by voltage losses

A PEC system is typically evaluated based on the photocurrent density measured at 1.23 V versus the reversible hydrogen electrode (V_{RHE}) and the onset potential, where the current

begins to increase in the system.[27,42,43] Although extensive efforts have been made to develop efficient light absorbers that enhance these metrics, the underestimation of measured current density (explained below) and methods to rectify it has barely received attention.

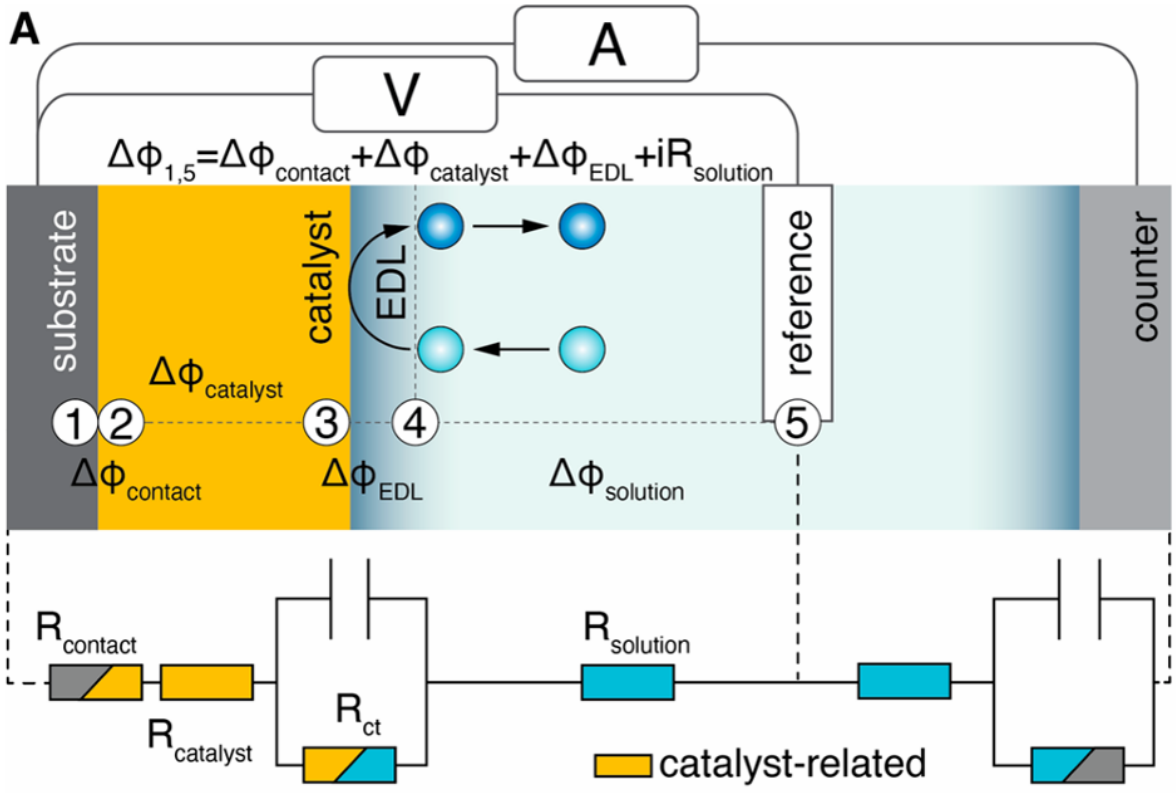

Figure 10 Schematic image representing a photoelectrochemical (PEC) water splitting cell and Randle circuit ($\Delta\phi_{1,5}$: voltage drop between the point 1 and 5, $\Delta\phi_{contact}$ and $R_{contact}$: voltage drop and resistance at the substrate/catalyst interface, $\Delta\phi_{catalyst}$ and $R_{catalyst}$: voltage drop and resistance across the catalyst, $\Delta\phi_{EDL}$ and R_{ct}: voltage drop and resistance at electrical double layer (EDL), $\Delta\phi_{solution}$ and $R_{solution}$: voltage drop and resistance across the solution). Adapted from ref. [44].

As illustrated in **figure 10**, the half-cell reaction for the oxygen evolution reaction (OER) in a photoelectrochemical (PEC) water splitting cell is represented by a simplified equivalent circuit, known as the Randle's circuit.[45] The uncompensated resistance (R_u) is the sum of the series

resistances from the solution, catalyst and back contact in this case. Since current density corresponding to the OER occurring at the solid/liquid interface passes through the entire cell with various the voltage losses, the interfacial current density is measured to be underestimated.

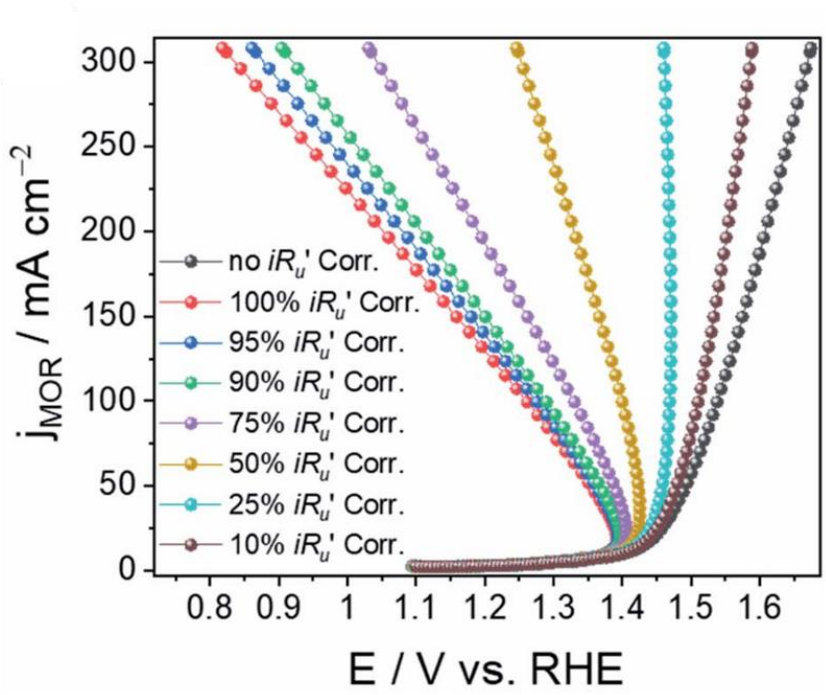

Figure 11 LSV curves resulting from methanol oxidation reaction (MOR) depending on the extent of iR correction. Adapted from ref. [46].

To obtain a more accurate representation of the interfacial current density, iR compensation is commonly applied by correcting the voltage drop across R_u, isolating the voltage drop that occurs only at the interface.[45] Typically, the uncompensated resistance is estimated using the high-frequency resistance (R_{HF}) derived from electrochemical impedance spectroscopy (EIS), assuming R_{HF} partially represents R_u. However, there is no clear guideline on the appropriate fraction of R_{HF} that needs to be compensated.[44] Besides, overcompensation results in overestimated current values showing bend back linear sweep voltammetry (LSV) curve as shown in **figure 11**.

As an alternative, interfacial resistance ($R_{interface}$) can be estimated directly by fitting the equivalent circuit model obtained from EIS measurements. Nevertheless, this approach is also limited because the depletion region at the solid/liquid interface varies with the applied voltage (V_a), implying that $R_{interface}$ is a function of V_a.[47–50] Consequently, EIS measurements must be performed at each V_a used during linear sweep voltammetry (LSV) to accurately determine the voltage drop at the interface, which requires substantial computational efforts.

1.4 pH-gradient voltage drop (V_{pH}) as a direct indicator for water splitting

As previously discussed, accurately determining the actual current and voltage drop at the solid/liquid interface, where photoelectrochemical (PEC) water splitting occurs, remains challenging. Furthermore, when current values under different conditions or for different materials are not distinctly comparable, it becomes difficult to assess which system exhibits superior performance. Hence, evaluating the efficiency of a PEC system using a single output parameter is insufficient.

To address this limitation, the pH-gradient voltage drop (V_{pH}) generated during the oxygen evolution reaction (OER) serves as an additional output parameter. During the OER (eq. (1.1)), protons (H^+) are generated together with oxygen and electrons. When the OER occurs in electrolytes containing abundant proton donors or acceptors such as buffered, acidic and basic solutions, the accumulation of protons near the electrode surface induces a pH gradient. This gradient results in a V_{pH} as expressed in eq. (1.19).[51,52]

$$V_{pH} = \frac{RT}{nF}(pH_{final} - pH_{initial}) \qquad (1.19)$$

where R is the ideal gas constant (8.314 J mol^{-1} K^{-1}), T is the absolute temperature, n is the number of moles of electrons transferred in a reaction, and F is the Faraday constant (96485 C

mol^{-1}). According to eq. (1.2) at the room temperature (T = 298 K), the V_{pH} shifts approximately 0.6 mV per unit of pH change.

If V_{pH} can be isolated from the total voltage drop across the PEC cell formed by applied voltage (V_a), it serves as a direct indicator of PEC water splitting activity. Voltage drop at the solid/liquid interface ($V_{interface}$) is expressed as the sum of V_{pH}, charge transfer voltage drop (V_{ct}) and equilibrium potential for OER ($E_{eq,\ OER}$). The $E_{eq,\ OER}$ is theoretically 1.23 V_{RHE} for both non-faradaic and faradaic reaction (OER), involving a four-electron transfer process.[8,53,54] The V_{ct} represents the kinetic overpotential required for charge transfer across the solid/liquid interface. Consequently, under the faradaic condition, the $V_{interface}$ varies with V_a as the sum of V_{ct} and V_{pH}, whereas in non-faradaic reaction, it is determined only by V_{ct}.[55] These relationship is expressed by the following equations.

$$V_{interface} = V_{ct} \text{ (in non-faradaic reaction)} \qquad (1.20)$$

$$V_{interface} = V_{ct} + V_{pH} \text{ (in faradaic reaction (OER))} \qquad (1.21)$$

1.5 State-of-the-art in V_{pH} measurements

One of the most commonly used techniques for measuring pH-gradient voltage drop (V_{pH}) is rotating ring-disk electrode (RRDE) voltammetry.[56] In this method, electrochemical reactions occur at the disk electrode, while reaction products or intermediates in the electrolyte are transported to the ring electrode through convection and diffusion. The protons generated at the disk electrode are subsequently detected at the ring electrode as a Nernstian potential shift, reflecting the local pH change that can be calculated using eq. (1.19) as shown in **figure 12**.

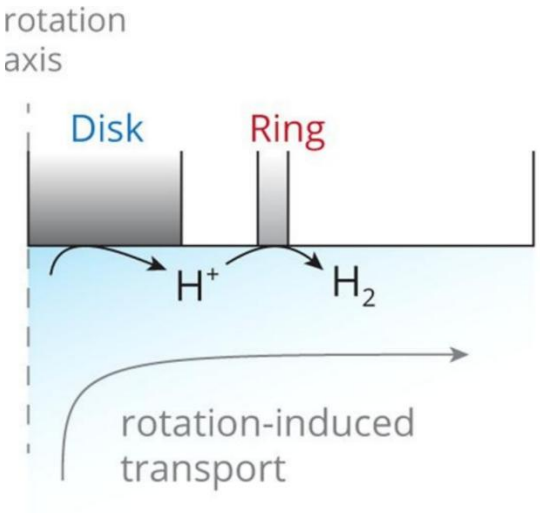

Figure 12 Configuration a rotating ring disk electrode. Adapted from ref. [57].

Fluorescence spectroscopy has also been employed to visualize pH variations using fluorescent dyes or sensors.[58] In addition, scanning electrochemical microscopy (SECM) has been explored for local V_{pH} measurement. However, these analytical techniques require complex instrumentation and therefore are unsuitable for practical photoelectrochemical (PEC) system evaluation.[52] Furthermore, while some measurements are performed under hydrodynamic conditions, PEC water splitting is generally carried out in a hydrostatic electrolyte environment.[59]

To overcome these limitations, an electrochemically measurable approach for V_{pH} quantification is needed. Sauvé *et al.* developed a method to quantify interfacial pH by analyzing post-electrolysis open-circuit potential (OCP) decay transients.[52] This technique enables direct measurement of V_{pH} resulting from electrocatalytic hydrogen evolution reaction (HER) by determining the pH-induced potential shift from the equilibrium potential during OCP decay. In their study, interfacial pH variations were quantified using a platinum electrode under various electrolyte conditions. However, for PEC overall water splitting, OER must be primarily considered and a semiconductor photoanode is required to absorb photons. The introduction of a semiconductor makes the OER process more complex, as charge transfer

kinetics at the solid/liquid interface must be considered in this multi-electron reaction. In this work, the OCP decay technique is extended to PEC water splitting for the OER. Specifically, OCP decays are measured after applying voltages inducing non-faradaic reaction to quantify V_{ct} which is not considered in the previous work (Sauvé *et al.*[52]). Afterwards, OCP decays resulting from faradaic reactions (OER) are measured to quantify interfacial voltage drop ($V_{interface}$). V_{pH} is calculated by subtracting the obtained charge transfer voltage drop (V_{ct}) from non-faradaic reaction from the obtained $V_{interface}$ from faradaic reaction according to eq. (1.20) and (1.21). The principle quantifying V_{ct} and $V_{interface}$ from OCP decay is explained in detail in the section 2.5 and section 3.2.

The interfacial voltage components (V_{ct} and V_{pH}) are examined under various pH conditions (pH 0.7, 7 and 14), and voltage drop distributions are qualitatively revealed depending on H^+ concentration. In addition, the effect of illumination intensity on both V_{ct} and V_{pH} is investigated. The results indicate that the interfacial properties are primarily governed by the intrinsic contact between the solid and liquid phases, regardless of illumination intensity. Based on these observations, a power efficiency metric is proposed for evaluating electrocatalytic performance, where the extracted V_{pH} is combined with the photocurrent density as a conventional output parameter to provide a more comprehensive assessment. Finally, the applicability of the developed approach for V_{pH} extraction, initially demonstrated using TiO_2, is successfully extended to WO_3 photoanode.

2. Theoretical background

2.1 Semiconductor and electrolyte for PEC water splitting

The photoelectrochemical (PEC) water splitting reaction occurs at the semiconductor/electrolyte interface, where the electronic structure undergoes rearrangement. The electronic structure also responds dynamically to the externally applied potential. Therefore, understanding the changes in the interfacial energy band bending provides valuable insight into charge carrier dynamics relevant to PEC water splitting.

In a PEC water-splitting cell, contact between the semiconductor and the electrolyte results in Fermi-level alignment at the solid–liquid interface, establishing thermal equilibrium through charge redistribution. During this process in an n-type semiconductor, electrons flow from the semiconductor where the Fermi level is initially higher toward the electrolyte, which has a lower Fermi level corresponding to its redox potential, until equilibrium is achieved.[60–63]

As a consequence of this charge redistribution, the majority carriers (electrons in the case of n-type semiconductors) are depleted near the interface, forming a region known as the depletion layer or space-charge region.[64–66]

The interfacial charge is counterbalanced by adsorbed ionic species in the electrolyte, forming the Helmholtz layer and inducing a potential drop expressed as, $V_H = -0.06\Delta pHq^{-1}$ (where q is elementary charge and ΔpH is pH shift).[67–69]

Across the depletion region of thickness (w) in an n-type semiconductor, the potential distribution (ϕ) is obtained by solving Poisson's equation below

$$\frac{dE(x)}{dx} = \frac{d^2\phi(x)}{dx^2} = \frac{qN_D}{\varepsilon_0\varepsilon_r} \qquad (2.1)$$

where E is electric field, N_D is donor density, ε_0 is vacuum permittivity and ε_r is relative permittivity.

The boundary conditions for eq. (2.1) are $\frac{d\phi(x)}{dx} = \frac{qN_D}{\varepsilon_0\varepsilon_r}(w - x)$ within the depletion region and $\mathrm{E(x)} = 0$ in the bulk. Therefore, the solution is followed by

$$\phi(\mathrm{x}) = -\frac{qN_D}{2\varepsilon_0\varepsilon_r}(wx - \frac{1}{2}x^2) \qquad (2.2)$$

The thickness of depletion region is obtained by rearranging eq. (2.2) at x = w

$$\mathrm{w} = \sqrt{\frac{2\varepsilon_0\varepsilon_r V_{sc}}{qN_D}} \qquad (2.3)$$

where V_{sc} is potential formed at the depletion region edge given by

$$V_{sc} = V_a - V_{fb} \qquad (2.4)$$

and flat band potential, V_{fb}. When V_{fb} is applied ($V_a = V_{fb}$), $V_{sc} = 0$.

The thickness of depletion region is altered by applied bias as seen in the voltage-dependent form, which will be discussed in detail, afterwards.

Since the depletion region in semiconductor and Helmholtz layer in electrolyte are connected in series at the semiconductor/electrolyte interface, the interfacial capacitance, $C_{interface}$ is expressed by[44,70,71]

$$\frac{1}{C_{interface}} = \frac{1}{C_{sc}} + \frac{1}{C_H} \qquad (2.5)$$

where C_{sc} and C_H denote capacitances of the depletion region and Helmholtz layer, respectively. In general assumption, C_{sc} approximates $C_{interface}$ and C_{sc} is ignored because C_{sc} encompasses wide range according to energy band bending while C_H remains constant between 0.1 F m^{-2}

and 0.2 F m^{-2}.[70] Therefore, most of voltage drop formed at the semiconductor/electrolyte interface originates from the semiconductor side of the interface.[48,72–75]

The depletion region capacitance, C_{sc}, is the capacitance of a parallel plate capacitor and depends on the depletion region width, w

$$C_{sc} = \frac{\varepsilon_0 \varepsilon_r}{w} \tag{2.6}$$

By substituting eq. (2.3) into eq. (2.6), the Mott-Schotkky relationship is obtained

$$\frac{1}{C_{sc}^2} = \frac{V_{sc}}{qN_D}\frac{1}{\varepsilon_0 \varepsilon_r} \tag{2.7}$$

By plotting C_{sc}^{-2} as a function of applied potential yields the flat-band potential from the x-axis intercept and the donor density from the slope of the Mott–Schottky plot.

Understanding the formation and behavior of the depletion region is crucial. When holes are generated by photon absorption within the depletion region, they are driven toward the semiconductor/electrolyte interface by the built-in potential across the space-charge layer. These photo-generated holes then participate in the oxidation of water molecules, thereby enabling the overall PEC water-splitting reaction.

2.2 charge transfer at the semiconductor/electrolyte interface

So far, the fundamental principle governing the formation of the depletion region has been discussed. While holes transferred across the depletion layer initiate the water-splitting reaction, two possible charge transfer pathways are involved in the photoelectrochemical (PEC) oxygen evolution reaction (OER), indicating direct and indirect hole transfer at the semiconductor/electrolyte interface.[76–80] The hole transfer rate through the interface depends strongly on the dominant transfer mechanism, which ultimately determines the PEC water

splitting performance. Therefore, identifying which transfer pathway governs a given system is of crucial importance.

In the direct hole transfer mechanism, photogenerated holes in the valence band are directly transferred to semiconductor/eletrolyte interface, where they participate in water oxidation (**figure 13(a)**). Simultaneously, photogenerated holes recombine with conduction band electrons, a process referred to as band-to-band recombination.

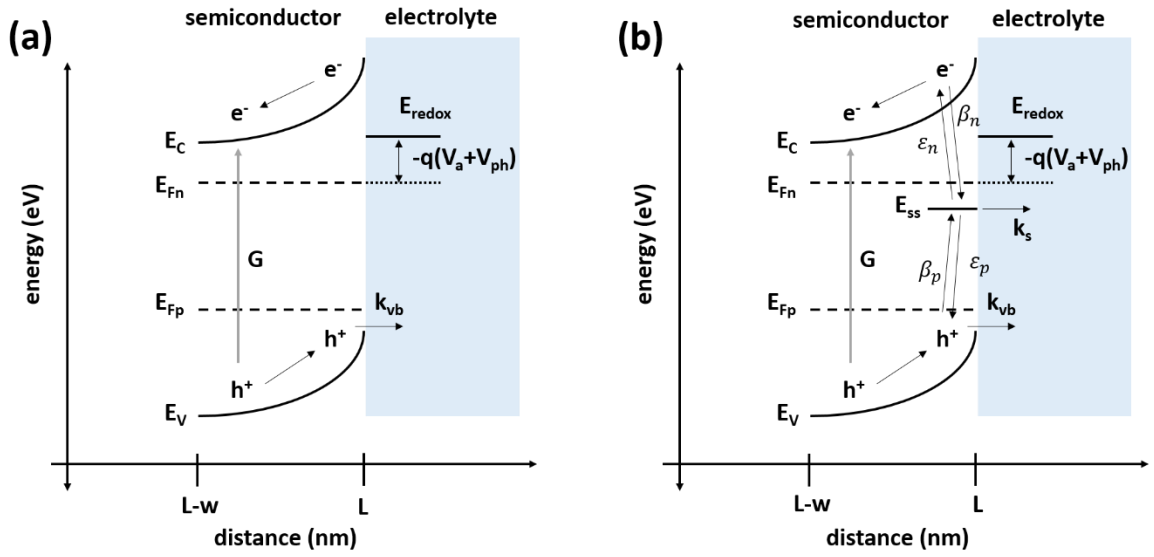

Figure 13 Energy band diagram showing (a) direct hole transfer and (b) indirect hole transfer at the semiconductor/electrolyte interface (EC: energy level of conduction band edge, E_V: energy level of valence band edge, E_{Fn}: electron quasi-Fermi level, E_{Fp}: hole quasi-Fermi level, G: photogeneration rate, K_{vb}: hole transfer at valence band, E_{redox}: redox level of electrolyte, q: elementary charge, V_a: applied bias, V_{ph}: photovoltage, E_{ss}: energy level of surface state, K_s: hole transfer at surface state, β_n and ε_n: probability of trapping and detrapping for electrons in conduction band, β_p and ε_p: probability of trapping and detrapping for holes in valence band, w: thickness of depletion region).

In contrast, indirect hole transfer occurs in semiconductors possessing surface states whose energy levels lie within the bandgap between the conduction band minimum (CBM) and valence band maximum (VBM), as shown in **figure 13(b)**. Photogenerated holes are trapped in these surface states and transferred through them to the interface where they drive the OER. The trapped charge carriers also recombine with conduction band electrons through trap-assisted recombination.[27,28,81] Although the direct and indirect transfer pathways compete with one another, they can also occur simultaneously. The direct and indirect hole transfer mechanisms are distinguished by low frequency capacitance in the section 2.4.

Under an applied anodic bias, additional holes accumulate at surface states, contributing to the anodic current during the OER.[82] However, the recombination kinetics associated with these surface states are directly correlated with the evolution of the anodic current rather than merely their presence.[83] Even in the absence of surface states, recombination dynamics play a significant role in determining the overall current–voltage behavior. Moreover, the interplay between charge transfer and recombination at surface states profoundly influences the onset potential, offering an effective handle to optimize photoanode performance for efficient PEC water splitting.[84]

In this section, the direct hole transfer across the depletion region, along with the associated band-to-band recombination, is investigated through a full drift–diffusion numerical simulation (numerical calculation solving the drift and diffusion equations of charge carriers). The resulting current–voltage characteristics, interfacial hole concentrations, and energy band diagrams under both forward and reverse bias conditions are analyzed to elucidate the mechanism of PEC water splitting governed by direct hole transfer, regarding the system in **figure 13(a)**.

For the simulation, the governing equations describing charge transport and production are Poisson's equation for electrostatic potential (ϕ), the continuity equations and drift-diffusion equation for electron (n) and hole (p),

$$\frac{d^2\phi}{dx^2} = -\frac{q(N_D - N_A + p - n)}{\varepsilon_0 \varepsilon_r} \quad (2.8)$$

$$\frac{\partial n}{\partial t} = \frac{1}{q}\frac{\partial J_n}{\partial x} + G - R \quad (2.9)$$

$$\frac{\partial p}{\partial t} = -\frac{1}{q}\frac{\partial J_p}{\partial x} + G - R \quad (2.10)$$

$$J_n = \mathrm{q}D_n \frac{\partial n}{\partial x} - q\mu_n n \frac{\partial \phi}{\partial x} \quad (2.11)$$

$$J_p = -\mathrm{q}D_p \frac{\partial p}{\partial x} - q\mu_p p \frac{\partial \phi}{\partial x} \quad (2.12)$$

where N_D are N_A are density of donor and acceptor, J_n and J_p are electron and hole current density, D_n and D_p are diffusion coefficient of electron and hole, μ_n and μ_p are mobility of electron and hole, and q is elementary charge.

In eq. (2.9) and (2.10), G and R denote the photo-induced charge generation rate described by the Lambert-Beer law, $\mathrm{G} = \alpha I_0 e^{-\alpha x}$ (α: absorption coefficient and I_0: photon flux) and the band-to-band recombination rate, $\mathrm{R} = \mathrm{B}(\mathrm{np} - n_i^2)$ (B: recombination constant and n_i : intrinsic donor density), respectively. Under steady state, $\frac{\partial n}{\partial t} = \frac{\partial p}{\partial t} = 0$ is assumed. The total current density is the sum of J_n and J_p.

The boundary conditions for the system in **figure 13(a)** are given below. The electrostatic potentials at each interface are

$$\phi(0) = V_a \quad (2.13)$$

$$\phi(\mathrm{L}) = 0 \quad (2.14)$$

In eq. (2.13), V_a is the applied voltage. Two additional boundary conditions for current are given from thermionic emission at the Schottky contact

$$J_n = -\mathrm{q}v_n(n - n_0) \tag{2.15}$$

$$J_p = \mathrm{q}v_p(p - p_0) \tag{2.16}$$

where n_0 and p_0 are equilibrium electron and hole concentration, respectively. In eq. (2.15) and (2.16), v_n and v_p are the recombination velocity of electron and hole, respectively given by

$$v_n = \frac{A_n T^2}{qN_c} \tag{2.17}$$

$$v_p = \frac{A_p T^2}{qN_v} \tag{2.18}$$

where A_n, A_p, N_c, N_v and T are Richardson constants for electron and hole, effective density of states in conduction band and valence band, and temperature, respectively.

The equilibrium electron concentration (n_0) and hole concentration (p_0) are

$$n_0 = N_c \exp(-\frac{q\Phi_B}{k_B T}) \tag{2.19}$$

$$p_0 = N_v \exp(-\frac{q(E_g - \Phi_B)}{k_B T}) \tag{2.20}$$

where E_g, Φ_B and k_B are band gap energy, barrier height at the semiconductor/electrolyte interface and Boltzmann constant, respectively.

The carrier concentrations at the back contact electrode forming ideal ohmic contact satisfy

$$\mathrm{n}(0) = n_0 = N_D \tag{2.21}$$

$$\mathrm{p}(0) = p_0 = \frac{n_i^2}{N_D} \tag{2.22}$$

where n_i denotes intrinsic electron concentration given by

$$n_i = \sqrt{N_c N_v \exp(-\frac{E_g}{k_B T})} \qquad (2.23)$$

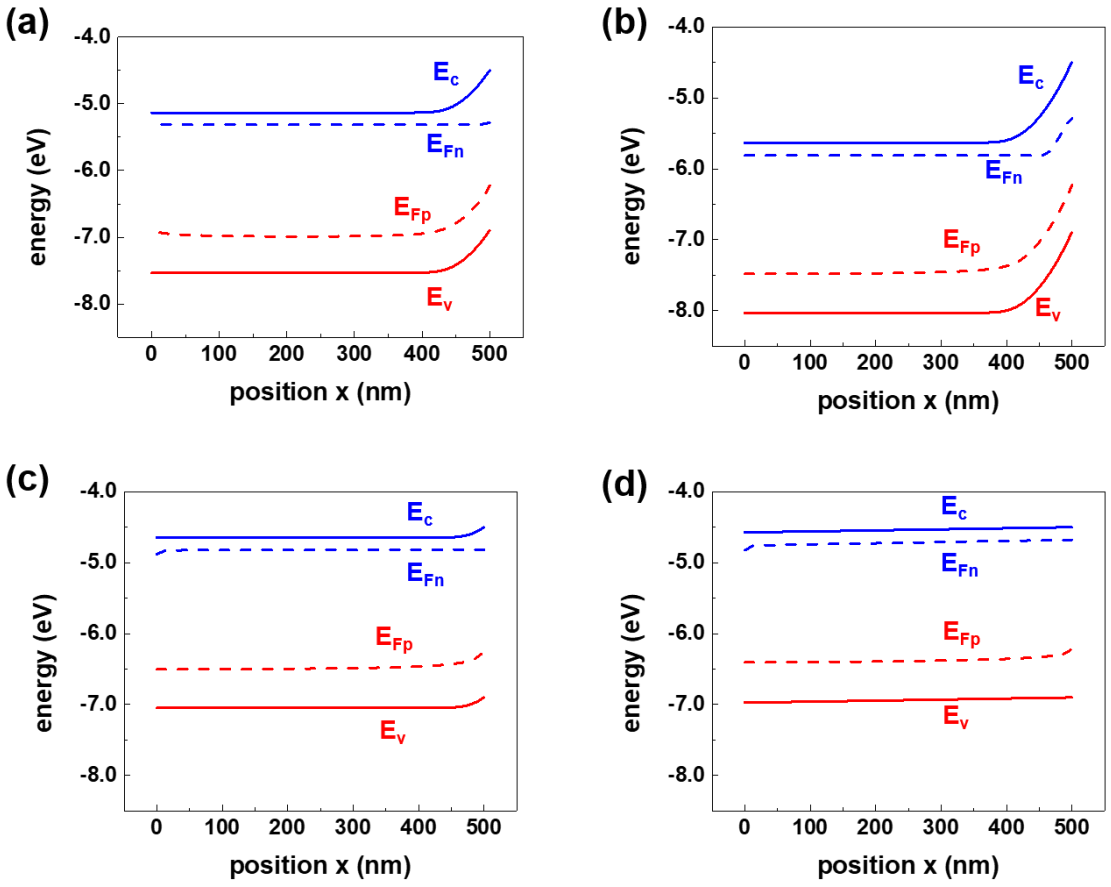

Figure 14 Simulated energy band diagrams of n-type semiconductor in junction with electrolyte under illumination at (a) no bias, (b) reverse bias, (c) forward bias and (d) flat band potential. E_c and E_v are energy levels of conduction band and valence band edge. The back contact electrode/semiconductor interface is at $x = 0$ nm and the semiconductor/electrolyte interface is at $x = 500$ nm where light is illuminated. E_{Fn} and E_{Fp} are quasi-Fermi levels of electron and hole.

Energy band bending at the semiconductor/electrolyte interface under different bias conditions is illustrated in **figure 14**. Overall, Fermi level splits into E_{Fn} and E_{Fp} due to the photogeneration of electron-hole pair.

In equilibrium, a Schottky contact is established at the semiconductor/electrolyte interface (**figure 14(a)**). When a reverse (anodic) bias is applied, the depletion region extends deeper into the bulk according to eq. (2.3), resulting in an increased barrier height (**figure 14(b)**). Conversely, under forward (cathodic) bias, the depletion region narrows and the barrier height decreases (**figure 14(c)**). Upon further increasing the forward bias, the energy bands become flat (**figure 14(d)**). This condition is referred to as the flat-band potential or built-in potential, where the solid/liquid interface becomes effectively open-circuited.

The flat-band potential is formed at the Schottky contact, and its magnitude is determined by the difference in work functions between the solid and the liquid phases.[29] It is a crucial parameter for photoanode optimization, as the separation of photogenerated charge carriers in the depletion region is governed by the flat band potential.[85]

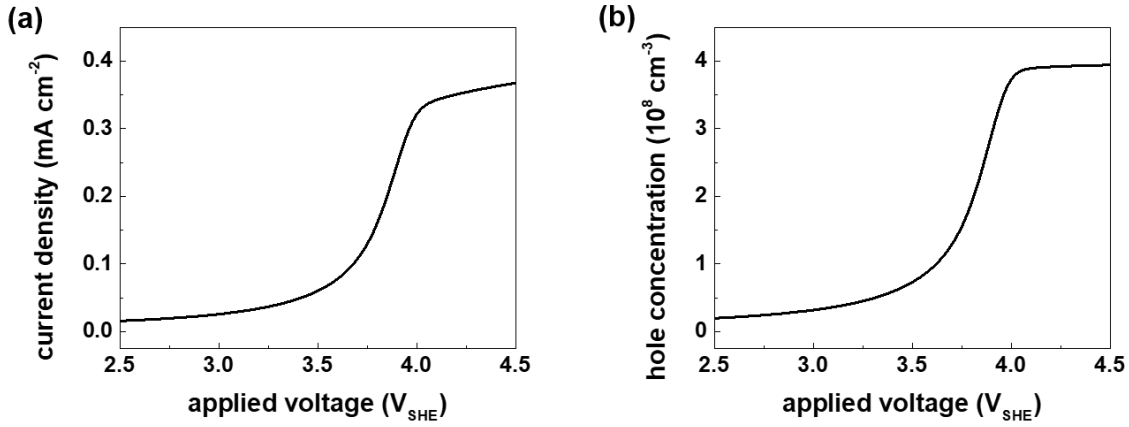

Figure 15 (a) Simulated current-voltage characteristics representing PEC water splitting by direct hole transfer. V_{SHE} is the voltage versus standard hydrogen electrode. (b) Simulated hole concentration at the solid/liquid interface

Under reverse bias, holes are preferentially driven across the semicondcutor/electrolyte interface, as reflected in the increase of current density with increasing reverse bias shown in **figure 15(a)**, which follows the typical diode relationship

$$j = I_s(exp\frac{V_a}{V_T} - 1) \qquad (2.24)$$

where I_s is the reverse saturation current density, and V_T is the thermal voltage. The current remains nearly constant while holes are blocked at the solid/liquid interface until the flat-band potential is reached, approximately at 3.8 V_{SHE}. Beyond this potential, the current density begins to rise, indicating that the flat-band potential determines the onset potential of photocurrent generation.

As shown in **figure 15(b)**, the hole concentration at the solid/liquid interface increases with the applied reverse bias but eventually saturates at higher bias values. This saturation accounts for the limited increase in current density under strong reverse bias, as observed in **figure 15(a)**.

The results presented in **figure 14** and **figure 15** suggest that, in the direct hole transfer mechanism, the enhancement of the depletion region leads to an increase in hole concentration at the semiconductor/electrolyte interface, thereby increasing the photocurrent density. Consequently, parameters influencing the hole transfer rate such as the interfacial boundary condition for hole current density (eq. (2.16)) can be tuned by adjusting intrinsic material properties (E_g and Φ_B in eq. (2.20)) to improve PEC water splitting.[71] According to Bertoluzzi *et al.*[82], since indirect hole transfer competes with direct hole transfer, the hole concentration alone does not solely determine the current density in the indirect mechanism. The presence of surface states, characteristic of the indirect pathway, enhances recombination-driven charge transfer kinetics, thereby increasing the maximum achievable photocurrent density.

2.3 Current-voltage characteristics representing PEC water splitting

The simulation study describing the direct hole transfer quantitatively analyzes the current density and hole concentration at the semiconductor/electrolyte interface as a function of changes in the energy band structure. It is found that the hole concentration directly contributes to the current density. Since the anodic current density represents the rate of water splitting, understanding its evolution is essential. Therefore, in this section, the current–voltage characteristics governed by direct hole transfer are derived to clarify the factors that determine the current density, following the Reichman model.

The hole transfer rate (eq. (2.10)) in an n-type semiconductor under illumination is solved at steady-state as follows

$$\frac{\partial p}{\partial t} = -\frac{\partial}{\partial x}\frac{J_p}{q} + G - R = 0 \qquad (2.25)$$

In the depletion region, photogenerated electrons and holes are separated by the built-in electric field. Thus, only generation is considered while recombination is neglected.

The generation rate, G, in the depletion region follows Lambert-Beer law as below

$$\mathrm{G} = \alpha_\lambda I_\lambda e^{-\alpha_\lambda x} \qquad (2.26)$$

where α_λ and I_λ denote monochromatic absorption coefficient and photon flux, and λ is wavelength. For simplicity, G is considered for monochromatic incident light.

The monochromatic photon flux, I_λ, is given as

$$I_\lambda = \frac{\lambda P_0}{hc} \qquad (2.27)$$

where P_0 is light intensity, h is Planck's constant and c is speed of light.

The recombination rate, R, in the bulk is given as

$$\mathrm{r} = \frac{p - p_0}{\tau_p} \tag{2.28}$$

where p_0 is hole concentration in equilibrium and τ_p is hole life time.

The hole current is defined by hole gradient with diffusion coefficient, D_p

$$J_p = -\mathrm{q} D_p \frac{dp}{dx} \tag{2.29}$$

By substituting eq. (2.29) into eq. (2.25), the hole transfer rate is rewritten as

$$D_p \frac{\partial^2 p}{\partial x^2} + \alpha_\lambda I_\lambda e^{-\alpha_\lambda x} - \frac{p - p_0}{\tau_p} = 0 \tag{2.30}$$

The boundary conditions for the system in **figure 13(a)** for eq. (2.30) are given as $\mathrm{p}(\infty) = p_0$ and $\mathrm{p}(\mathrm{L} - \mathrm{w}) = p_w$ which mean the hole concentration in the bulk is same to the hole concentration in equilibrium and the hole concentration at the edge of the depletion region is p_w. Therefore, the analytic solution is

$$\mathrm{p} = p_0 + \frac{\alpha_\lambda I_\lambda \tau_p \exp(-\alpha_\lambda x)}{1 - \alpha_\lambda^2 L_p^2} + Kexp(-\frac{x}{L_p}) \tag{2.31}$$

with $L_p^2 = D_p \tau_p$ (L_p: hole diffusion length).

The constant K corresponds to

$$\mathrm{K} = \exp(\frac{\mathrm{w}}{L_p})(p_w - p_0 - \frac{\alpha_\lambda I_\lambda \tau_p \exp(-\alpha_\lambda w)}{1 - \alpha_\lambda^2 L_p^2}) \tag{2.32}$$

by substituting eq. (2.32) to eq. (2.29), the diffusion current j_{diff} is obtained as

$$j_{diff} = -j_0 \left(\frac{p_w}{p_0} - 1\right) + \frac{q I_\lambda \alpha_\lambda L_p \exp(-\alpha_\lambda w)}{1 + \alpha L_p} \tag{2.33}$$

where j_0 is the saturation current following $j_0 = \frac{q p_0 D_p}{L_p}$.

The photogenerated current in the depletion region is obtained by integrating the generation rate, G, over the depletion region thickness, w,

$$j_{sc} = \mathrm{q}I_{\lambda}(1 - \exp(-\alpha_{\lambda}w)) \qquad (2.34)$$

implying that all photogenerated holes are transferred to the semicondcutor/electrolyte interface without recombination.

The total hole current, j_v, is obtained by summation of j_{diff} and j_{sc} in valence band

$$j_v = j_{diff} + j_{sc} = -j_0\left(\frac{p_w}{p_0} - 1\right) + qI_{\lambda}(1 - \frac{\exp(-\alpha_{\lambda}w)}{1+\alpha_{\lambda}L_p}) \qquad (2.35)$$

The j_v is also expressed in terms of the hole concentration at the solid/liquid interface, p_s

$$j_v = j_v^0(\frac{p_s}{p_s^0} - 1) \qquad (2.36)$$

where j_v^0 is equilibrium valence band current and p_s^0 is equilibrium hole concentration at the solid/liquid interface.

The hole concentration at the semiconductor/electrolyte interface, p_s is expressed by

$$p_s = p_w\exp(\frac{qV_{sc}}{kT}) \qquad (2.37)$$

Combining eq. (2.35) - (2.37) yields the Reichman model, which describes current-voltage characteristics for direct hole transfer in PEC water splitting[76,77,86–88]

$$j_v = \frac{j_g - j_0\exp(-\frac{qV_{sc}}{kT})}{1+\frac{j_0}{j_v^0}\exp(-\frac{qV_{sc}}{kT})} \qquad (2.38)$$

When $p_w = 0$ in eq. (2.33), the generation current, j_g, is given by

$$j_g = j_0 + qI_{\lambda}(1 - \frac{\exp(-\alpha_{\lambda}w)}{1+\alpha_{\lambda}L_p}) \qquad (2.39)$$

which is also obtained by solving eq. (2.30) with the boundary condition $p(L - w) = 0$. The current-voltage characteristics in eq. (2.39) is designated as Gartner model.[89] Particularly, the second term in eq. (2.39) is Gartner photocurrent,[90] j_G

$$j_G = qI_\lambda(1 - \frac{\exp(-\alpha_\lambda w)}{1+\alpha_\lambda L_p}) \qquad (2.40)$$

If the Gartner photocurrent is removed from eq. (2.38), the Reichman model in dark condition is evolved

$$j_v^{dark} = \frac{j_0 - j_0\exp(-\frac{qV_{sc}}{kT})}{1+\frac{j_0}{j_v^0}\exp(-\frac{qV_{sc}}{kT})} \qquad (2.41)$$

According to the Peter *et al.*[76], the Gartner photocurrent represents the converged value of the Reichman model, further increasing the applied voltage. The evolution of the Gartner photocurrent depends solely on the depletion region thickness, assuming that hole transfer is enhanced as the depletion region widens. Therefore, the simulation results in the previous section show good agreement with the derived model, confirming that the current density originates purely from hole transfer in the direct hole transfer.

Although the fundamental aspects of anodic current evolution have been elucidated, the anodic current itself corresponding to the catalytic rate has limitations as a direct measure of catalytic performance. The current-voltage characteristics represent measured current as a function of applied potential. To accurately evaluate catalytic efficiency, the anodic current should instead be analyzed with respect to the output potential, which will be discussed in the section 3.2.

2.4 Low frequency capacitance

Determining the type of low frequency capacitance allows distinguishing between direct and indirect hole transfer mechanisms. Since low-frequency capacitance is a crucial parameter to reveal the charge transfer mechanism, the fundamentals of low frequency capacitance and its characteristics in each mechanism are discussed in this section, following the approach introduced by Bertoluzzi *et al.*[82].

In the case of direct hole transfer, the low frequency capacitance can be derived by solving the continuity equations (eq. (2.9) and eq. (2.10)) for the system illustrated in **figure 13(a)**.

Assuming a transport-limited condition, the electron and hole concentrations are position-independent and can be represented by their values at the edge of the depletion region, such as $\mathrm{n(L-w)} = n_w$ and $\mathrm{p(L-w)} = p_w$. n_w is given by

$$n_w = n_0 \exp(-\frac{qV}{kT}) \qquad (2.42)$$

where n_0 is electron concentration in equilibrium, k is Boltzmann constant and T is temperature. Eq. (2.9) is simply integrated over the semiconductor thickness, L

$$L\frac{\partial n_w}{\partial t} = \frac{1}{q}(J_n(L) - J_n(0)) + L(G-R) \qquad (2.43)$$

The boundary conditions are $J_n(\mathrm{L}) = 0$ and $J_n(0) = J_n$ indicating that the entire electron current flows through the back contact forming an ohmic contact, while no electron current flows at the semicondcutor/electrolyte interface (Schottky contact). Therefore,

$$\mathrm{qL}\frac{\partial n_w}{\partial t} = -j_n + qL(G-R) \qquad (2.44)$$

In the same way, eq. (2.10) is integrated with the boundary conditions, $J_p(\mathrm{L}) = k_{vb}w(p_w - p_0)$ and $J_p(0) = 0$ which mean holes are transferred with the kinetic constant (k_{vb}) depending

on difference between p_w and hole concentration in equilibrium, p_0 , at the semiconductor/electrolyte interface, and no hole current flows at the back contact

$$\mathrm{L}\frac{\partial p_w}{\partial t} = L(G-R) - k_{vb}w(p_w - p_0) \qquad (2.45)$$

A small perturbation is applied to the voltage, and the affected parameters are expressed using the steady-state (overbar) and frequency-dependent (tilde) components. The resulting concentrations of electron and hole at the depletion region edge are $n_w = \bar{n}_w + \tilde{n}$ and $p_w = \bar{p}_w + \tilde{p}$, respectively. The frequency-dependent electron concentration is obtained by rearranging n_w with Taylor expansion

$$n_w = \bar{n}_w + \tilde{n} = n_0 \exp\left(-\frac{q\bar{V}}{kT}\right)\exp(-\frac{q\tilde{V}}{kT}) \qquad (2.46)$$

The steady-state electron concentration, $\bar{n}_w$, is expressed as $\bar{n}_w = n_0 \exp\left(-\frac{q\bar{V}}{kT}\right)$. Therefore, eq. (2.42) is

$$n_w = \bar{n}_w \exp(-\frac{q\tilde{V}}{kT}) \qquad (2.47)$$

Because of small perturbation ($\tilde{V} \ll 1$), the exponential factor is linearized with respect to the frequency factor[47,50,82,83]

$$n_w \approx \bar{n}_w \left(1 - \frac{q\tilde{V}}{kT}\right) \qquad (2.48)$$

By combining eq. (2.46) and (2.48), we obtain

$$\tilde{n} = -\bar{n}_w \frac{q\tilde{V}}{kT} \qquad (2.49)$$

The same principle is applied to p_w to obtain $\tilde{p}$

$$\tilde{p} = \bar{p}_w \frac{q\tilde{V}}{kT} \qquad (2.50)$$

By the small perturbation, eq. (2.44) and (2.45) are given by

$$\mathrm{qLj}\omega\tilde{n} = -\tilde{j}_n - qL\tilde{R} \tag{2.51}$$

$$\mathrm{j}\omega\tilde{p} = -B\bar{p}_w\tilde{n} - B\bar{n}_w\tilde{p} - k_{vb}\frac{w}{L}\tilde{p} \tag{2.52}$$

where ω is frequency of the small perturbation and j is imaginary unit. The generation rate is unaffected by the perturbation and thus neglected. By rearranging eq. (2.52), $\tilde{p}$ is obtained by

$$\tilde{p} = \frac{-B\bar{p}_w}{\mathrm{j}\omega+\mathrm{B}\bar{n}_w+k_{vb}\frac{w}{L}}\tilde{n} \tag{2.53}$$

The recombination rate by the perturbation is expressed as the form of the band-to-band recombination with recombination constant, B

$$\mathrm{R} = \mathrm{B}(n_w p_w - n_o p_0) = B(\bar{n}_w\bar{p}_w - n_o p_0) + B(\tilde{n}\bar{p}_w + \bar{n}_w\tilde{p} + \tilde{n}\tilde{p}) \tag{2.54}$$

The term having factors with overbar is steady-state recombination rate, $\bar{R}$, and the term with tilde is frequency-dependent recombination rate, $\tilde{R}$. With eq. (2.49) and (2.50), $\tilde{R}$ is given by

$$\tilde{R} = B(\tilde{n}\bar{p}_w + \bar{n}_w\tilde{p}) \tag{2.55}$$

Because $\tilde{V} \ll 1$, $\tilde{n}\tilde{p} \approx 0$. The combination of eq. (2.51) and (2.55) yields $\tilde{j}_n$

$$\tilde{j}_n = -qL(\mathrm{j}\omega\tilde{n} + B(\tilde{n}\bar{p}_w + \bar{n}_w\tilde{p})) \tag{2.56}$$

By substituting eq. (2.49) and (2.53) in eq. (2.56), $\tilde{j}_n$ is expressed with respect to $\tilde{V}$

$$\tilde{j}_n = \frac{q^2L}{kT}\bar{n}_w(\mathrm{j}\omega + \mathrm{B}\bar{p}_w - \frac{B^2\bar{n}_w\bar{p}_w}{\mathrm{j}\omega+\mathrm{B}\bar{n}_w+k_{vb}\frac{w}{L}})\,\tilde{V} \tag{2.57}$$

The inverse impedance of the system in **figure 13(a)** is obtained by eq. (2.57)

$$Z^{-1} = \frac{\tilde{j}_n}{\tilde{V}} = \mathrm{j}\omega\frac{q^2L}{kT}\bar{n}_w + \frac{1}{\frac{1}{\frac{q^2L}{kT}B\bar{n}_w\bar{p}_w} + \frac{1}{\mathrm{j}\omega\frac{q^2L}{kT}\bar{p}_w + k_{vb}w\frac{q^2L}{kT}\bar{p}_w}} \tag{2.58}$$

Each term represents following element such as electron capacitance in conduction band, C_n, hole capacitance in valence band, C_p, recombination resistance, R_{rec}, and charge transfer resistance, R_{ct}

$$C_n = \frac{q^2 L}{kT} \bar{n}_w \tag{2.59}$$

$$C_p = \frac{q^2 L}{kT} \bar{p}_w \tag{2.60}$$

$$R_{rec} = (\frac{q^2 L}{kT} B \bar{n}_w \bar{p}_w)^{-1} \tag{2.61}$$

$$R_{ct} = (k_{vb} \frac{w}{L} C_p)^{-1} \tag{2.62}$$

The geometric capacitance, C_g, is connected to C_n in parallel. Therefore, the semiconductor capacitance over the thickness, C_{layer}, formed by majority carrier is

$$C_{out} = \frac{C_n C_g}{C_n + C_g} \tag{2.63}$$

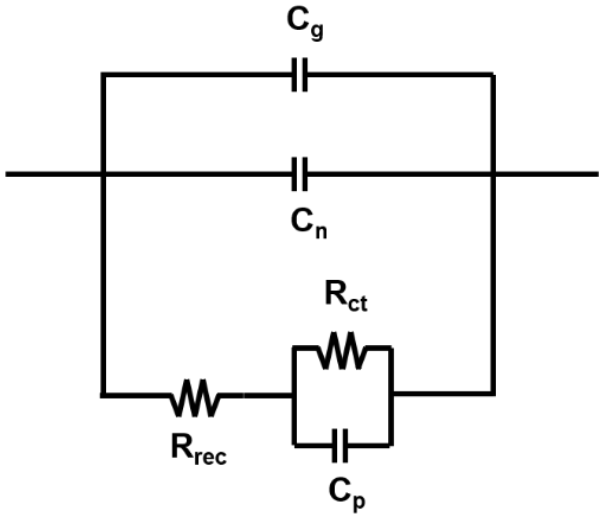

Figure 16 The derived equivalent circuit model (C_g: geometric capacitance, C_n: electron capacitance in conduction band, C_p: hole capacitance in valence band, R_{ct}: charge transfer resistance and R_{rec}: recombination resistance).

The equivalent circuit model derived from eq. (2.58) and (2.63) is shown in **figure 16**. In the model, C_p is the low frequency capacitance associated with direct hole transfer. According to eq. (2.60), C_p depends on $\bar{p}_w$, indicating that C_p increases under stronger reverse bias, as the hole concentration at the solid/liquid interface ($\bar{p}_w$) increases in **figure 15(b)**. In contrast, the low-frequency capacitance observed in the case of indirect hole transfer is related to the electron occupation probability of surface states, exhibiting a voltage-independent behavior.[82] Therefore, the charge transfer mechanism can be identified by examining whether the low frequency capacitance is governed by the applied voltage.

As shown in **figure 10**, the evolution of photocurrent density originates from the oxygen evolution reaction (OER) occurring at the semiconductor/electrolyte interface. The two mechanisms, direct and indirect hole transfer, explain how the OER proceeds at this interface. In a practical PEC water-splitting system (represented here by an OER half-cell), it is desirable to measure the interfacial current generated by either direct or indirect hole transfer to evaluate the OER rate. However, the current generated at the semiconductor/electrolyte interface is partially consumed by various voltage losses throughout the photoelectrochemical (PEC) system, leading to an underestimated measurement. This underestimation becomes more pronounced as the number of components causing voltage loss increases or as the effect of each component grows. Therefore, an alternative approach for accurately measuring catalytic efficiency is needed, which will be discussed in the section 3.2.

2.5 Voltage drop formation at the semiconductor/electrolyte interface

As mentioned in the section 1.5, in photoelectrochemical (PEC) water splitting, the voltage drop formed at the semiconductor/electrolyte interface ($V_{interface}$) can be divided into the charge

transfer voltage drop (V_{ct}) and the pH-gradient voltage drop (V_{pH}). The latter, V_{pH}, serves as an indicator of the oxygen evolution reaction (OER) described by eq. (1.1) and is employed for evaluating catalytic efficiency. The extraction of V_{pH} was originally developed by Sauvé *et al.* [52] through post-electrolysis open-circuit potential (OCP) decay transients during the hydrogen evolution reaction (HER). The principle is to monitor the OCP shift induced by proton (H^+) consumption from equilibrium, following the reaction given in eq. (1.19). In this work, the OCP decay technique used in electrocatalytic HER on Pt is extended to PEC water splitting for the OER with a semiconductor as a photoanode. To systematically quantify V_{ct} and V_{pH} from the OCP decay, the discharge behavior of a parallel plate capacitor is considered as an analogous model to the discharge process at the semiconductor/electrolyte interface in PEC water splitting.

During charging at the parallel plate capacitor, electrons accumulate on the parallel plate as voltage is applied, as illustrated in **figure 17(a)**. If resistive elements are present, a portion of the applied voltage (V_a) is consumed by the resistance, and the resulting voltage drop across the capacitor reaches V_c. When the fully charged capacitor discharges, the stored charge is released, and V_c decays through the resistor R, as shown in **figure 17(b)**. The time-dependent decay of the formed voltage drop at the interface is obtained by solving the differential equation derived from Kirchhoff's voltage law and given as a mono-exponential form

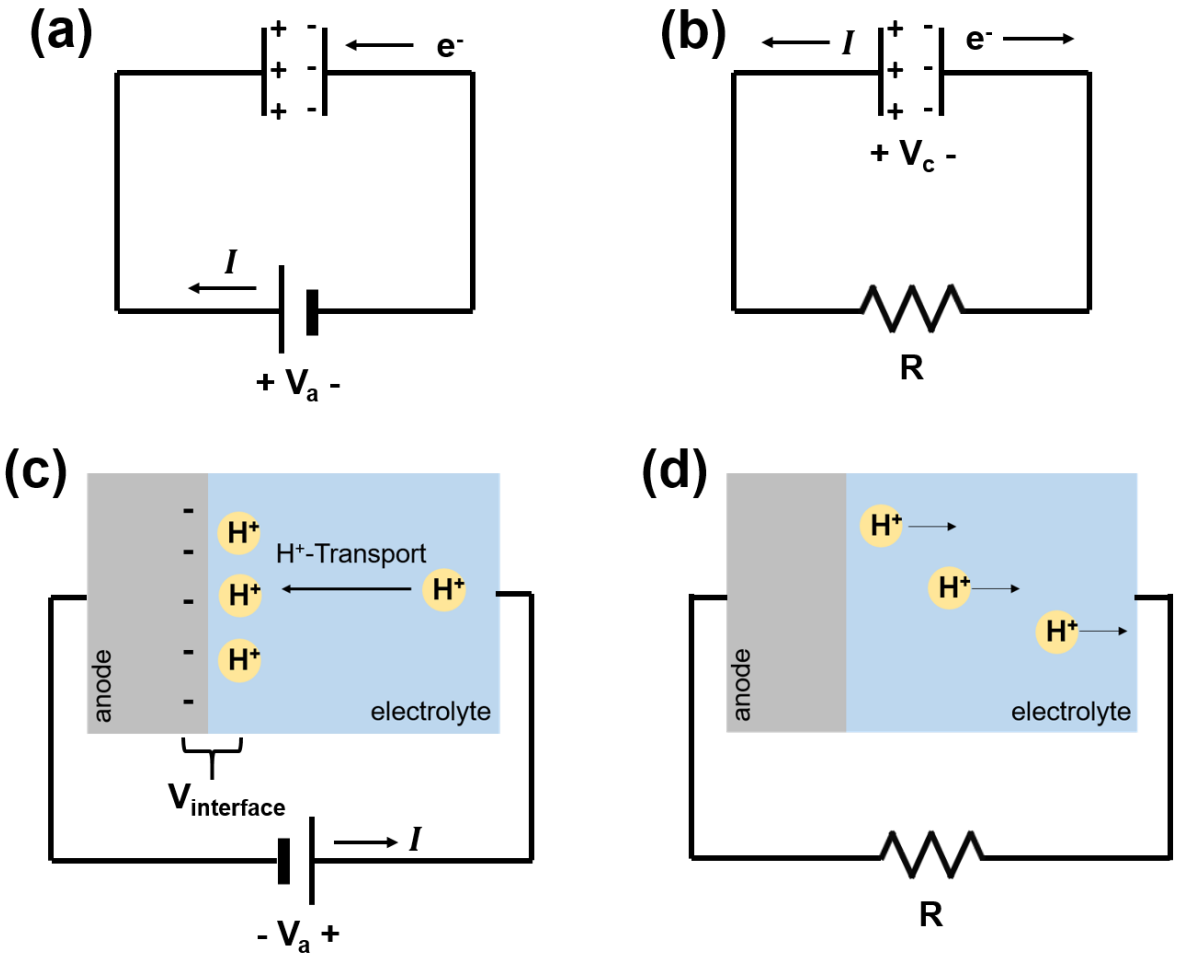

Figure 17 (a) charging and (b) discharging process in RC circuit. (c) charging and (d) discharging process at the solid/liquid interface in PEC water splitting (V_a: applied voltage, V_c: voltage drop formed at the parallel plate capacitor and $V_{interface}$: voltage drop formed at the semiconductor/electrolyte interface).

$$RC\frac{dv_c(t)}{dt} + v_c(t) = 0 \qquad (2.64)$$

$$v_c(t) = v_c(0)e^{-\frac{t}{RC}} \qquad (2.65)$$

where C and t are capacitance of the capacitor and time, respectively.

The same principle applies to the semiconductor/electrolyte interface. Upon contact, a depletion region forms in the semiconductor, while an electrical double layer is established in the electrolyte, together acting analogously to a parallel plate capacitor. As depicted in **figure 17(c)**, due to internal cell resistances, a portion of the applied potential ($V_{interface}$) is used to drive ionic species toward the interface. Among these, proton (H^+) transfer is dominant because of its high diffusion coefficient in aqueous electrolytes.[59] Once H^+ accumulation is completed under negative bias, $V_{interface}$ is established at the interface, analogous to the charged state in **figure 17(a)**. For the accumulation, H^+ is transferred by various mechanisms such as migration, diffusion and Grotthuss mechanism (**figure 18**).[91]

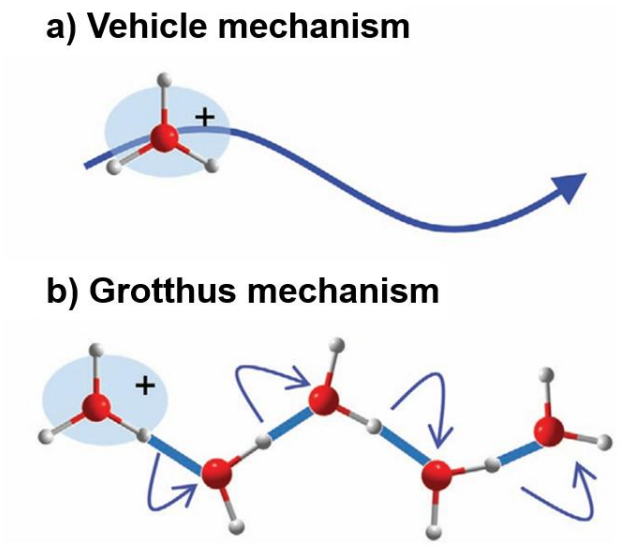

Figure 18 Proton (H^+) transfer mechanisms in water medium: (a) vehicle mechanism and (b) Grotthus mechanism. Adapted from ref. [92].

During discharge corresponding to OCP decay, $V_{interface}$ decays mono-exponentially, as described by eq. (2.65). When electrolytes containing abundant proton donors or acceptors are used, the interfacial H^+ concentration keeps constant over time while the OER proceeds, and depends on V_a.[59] Consequently, the pre-exponential factor in eq. (2.65) represents the V_a-

dependent $V_{interface}$. In the section 3.2, pre-exponential factors extracted from OCP decay under non-faradaic and faradaic conditions are assigned to V_{ct} and V_{pH}, respectively.

3. Results and discussion

3.1 Controlling degree of inversion in the $MgFe_2O_4$ film

3.1.1 Synthesis of single source precursor for $MgFe_2O_4$

For $MgFe_2O_4$ films with a narrow band gap value suitable for photoelectrochemical (PEC) water splitting, a single-source precursor, $[MgFe_2(O^tBu)_8]$, was synthesized for chemical vapor deposition (CVD). In CVD, a single-source precursor is advantageous for forming a phase-pure product because its molecular structure already contains the constituent elements of the desired compound. This structural pre-bonding lowers the molecular barrier compared to the use of multi-source precursors.[93] Therefore, a single-source precursor was selected for film growth to ensure compositional homogeneity and to enable accurate analysis of interfacial properties in PEC water splitting.

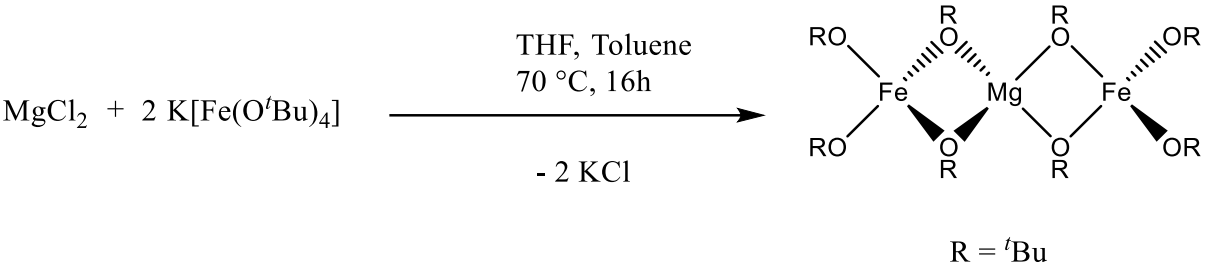

Figure 19 Salt metathesis reaction for the synthesis of heterometallic precursor $[MgFe_2(O^tBu)_8]$.

The heterometallic alkoxide precursor $[MgFe_2(O^tBu)_8]$ used for the deposition of $MgFe_2O_4$ films was synthesized following a previously reported salt metathesis reaction between $K[Fe(O^tBu)_4]$ and anhydrous magnesium chloride ($MgCl_2$) (**figure 19**).[94–96] The molecular structure of $[MgFe_2(O^tBu)_8]$ resembles the known heterometallic spiro-type complexes of the general formula $[M\{M'(O^tBu)_4\}_2]$ (M = Co, Zn, Ni, M' = Fe, Al),[94–97] featuring a divalent

central cation (Mg^{2+}) coordinated in a bidentate manner by two tert-butoxide ligands from the tetrahedral $Fe(O^tBu)_4\}^-$ alkoxometallate units.

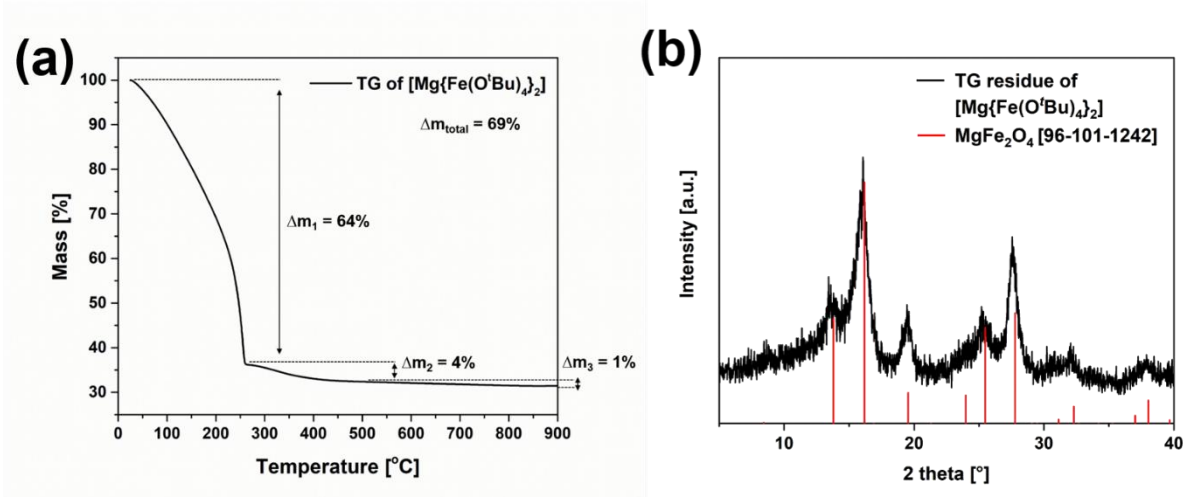

Figure 20 (a) Thermogravimetric measurement of $[Mg\{Fe(O^tBu)_4\}_2]$ (1) up to 900 °C with a heating rate of 10°C/min and (b) powder X-ray diffraction pattern of the TG residue with literature data shown as red vertical lines (JCPDS #96-101-1242)

Thermogravimetric analysis (TG) of precursor $[MgFe_2(O^tBu)_8]$ (**figure 20(a)**) revealed an initial mass loss attributable to instantaneous hydrolysis, a well-known phenomenon in metal alkoxides arising from their high intrinsic reactivity.[98–102] This property underscores their suitability as precursors for metal oxide formation. The decomposition proceeded in three distinct steps, resulting in a total mass loss of 69% (7.327 mg of the initial 10.6189 mg): (Δm_1 = 64% (6.796 mg) in the range 25 °C ~ 260 °C, Δm_2 = 4% (0.425 mg) in the range 260 °C ~ 500 °C and Δm_3 = 1% (0.106 mg) in the range 500 °C ~ 900 °C. This value is close to the theoretical mass loss of 72% expected for the formation of $MgFe_2O_4$, confirming that the observed decomposition pathway is consistent with the stoichiometric conversion to the spinel phase. The slight deviation from the theoretical value can be attributed to partial hydrolysis of the precursor which is unavoidable even under dry nitrogen conditions or to minor volatilization losses of the precursor during heating. No significant weight loss was detected

above 500 °C, indicating the formation of a thermally stable solid of defined composition. Consequently, this temperature was considered appropriate as the substrate temperature for subsequent CVD experiments.

The formation of the solid-state ternary compound $MgFe_2O_4$ was further confirmed by powder X-ray diffraction (XRD) analysis of the solid residue collected from the crucible, as shown in **figure 20(b)**. The measured mass loss, which is close to the theoretical mass loss expected for the transformation of the $[MgFe_2(O^tBu)_8]$ precursor to $MgFe_2O_4$ (**figure 20(a)**), supports the assignment of the XRD pattern to the $MgFe_2O_4$ spinel. Moreover, the observed XRD pattern matches the reference peaks of $MgFe_2O_4$. The formation of single phase $MgFe_2O_4$ demonstrates a key advantage of using a single source precursor. In contrast, Bloesser *et al.* synthesized $MgFe_2O_4$ nanoparticles via microwave-assisted reaction using separate elemental sources, $Mg(acac)_2$ and $Fe(acac)_3$.[41] Unless these two sources are mixed in an optimized ration, secondary phases inevitably form, even at reaction temperature lower than those required for $MgFe_2O_4$ segregation.

3.1.2 Characterization of $MgFe_2O_4$ films grown in magnetic field-assisted chemical vapor deposition (mfCVD)

In addition to confirming the formation of phase-pure $MgFe_2O_4$ through thermal decomposition (**figure 20**), it was verified that the films maintained phase purity under varying magnetic field conditions during magnetic field-assisted chemical vapor deposition (mfCVD). Although cation disorder exists within the $MgFe_2O_4$ spinel structure, maintaining constant phase purity ensures that the effects of inversion degree on photoelectrochemical (PEC) water splitting can be systematically investigated.

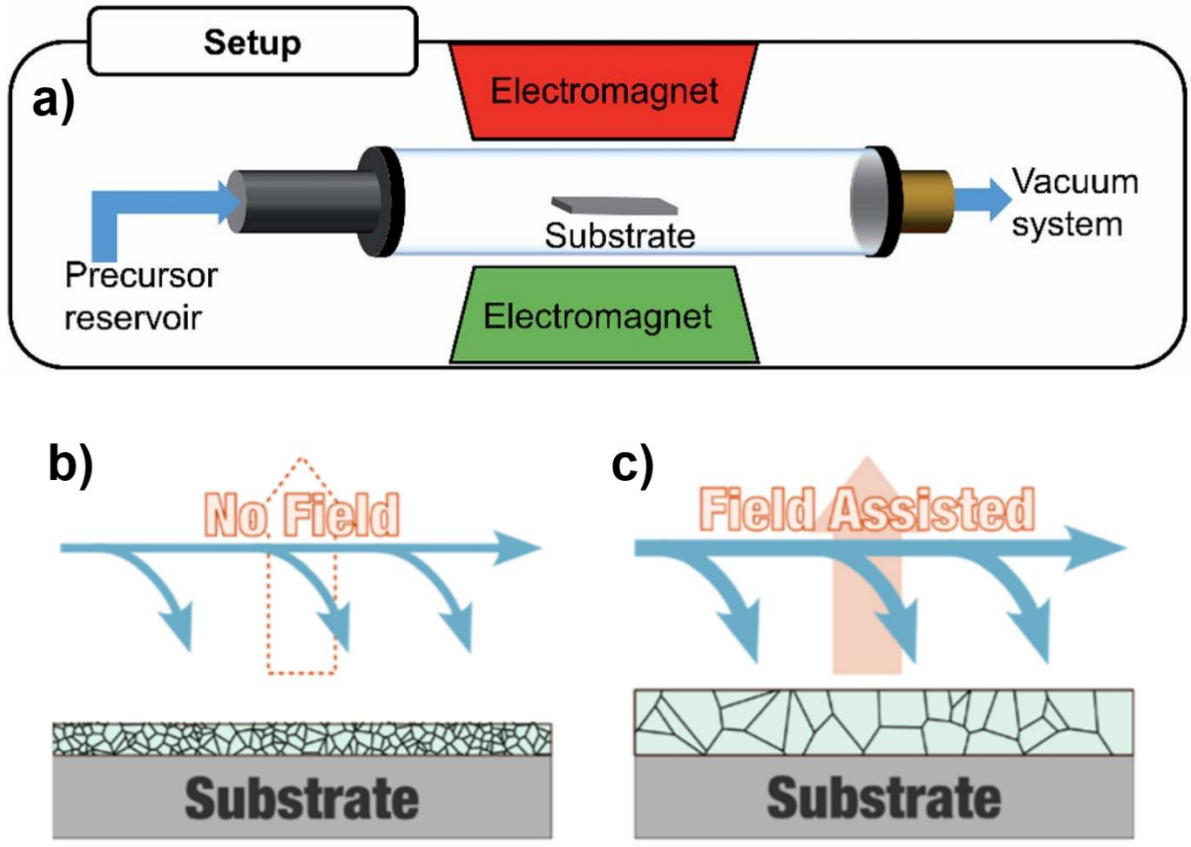

Figure 21 (a) Configuration of magnetic field-assisted chemical vapor deposition (CVD) setup. Thin film growth on the substrate in CVD (b) without and (c) with external magnetic field. Adapted from ref. [33] and [103].

Magnetic field-assisted chemical vapor deposition (mfCVD) was used to grow $MgFe_2O_4$ thin film using the heterometallic single-source precursor [$MgFe_2(O^tBu)_8$] in a cold-wall CVD reactor equipped with a perpendicularly aligned permanent magnet in **figure 21(a)**. The $MgFe_2O_4$ films were deposited on fluorine-doped tin oxide (FTO) substrates by heating the precursor to 180 °C and maintain the substrate temperature at 500 °C for 20 minutes. While the precursor flows and the $MgFe_2O_4$ film is deposited on the substrate, the external magnetic field is continuously applied until the substrate cools to room temperature after deposition. The application of an external magnetic field during CVD serves as a synthetic parameter that directs the movement of charged species in the precursor, thereby influencing nucleation and

growth rates and ultimately altering the microstructure and morphology of the film, as illustrated in **figure 21(b)** and **(c)**.[103]

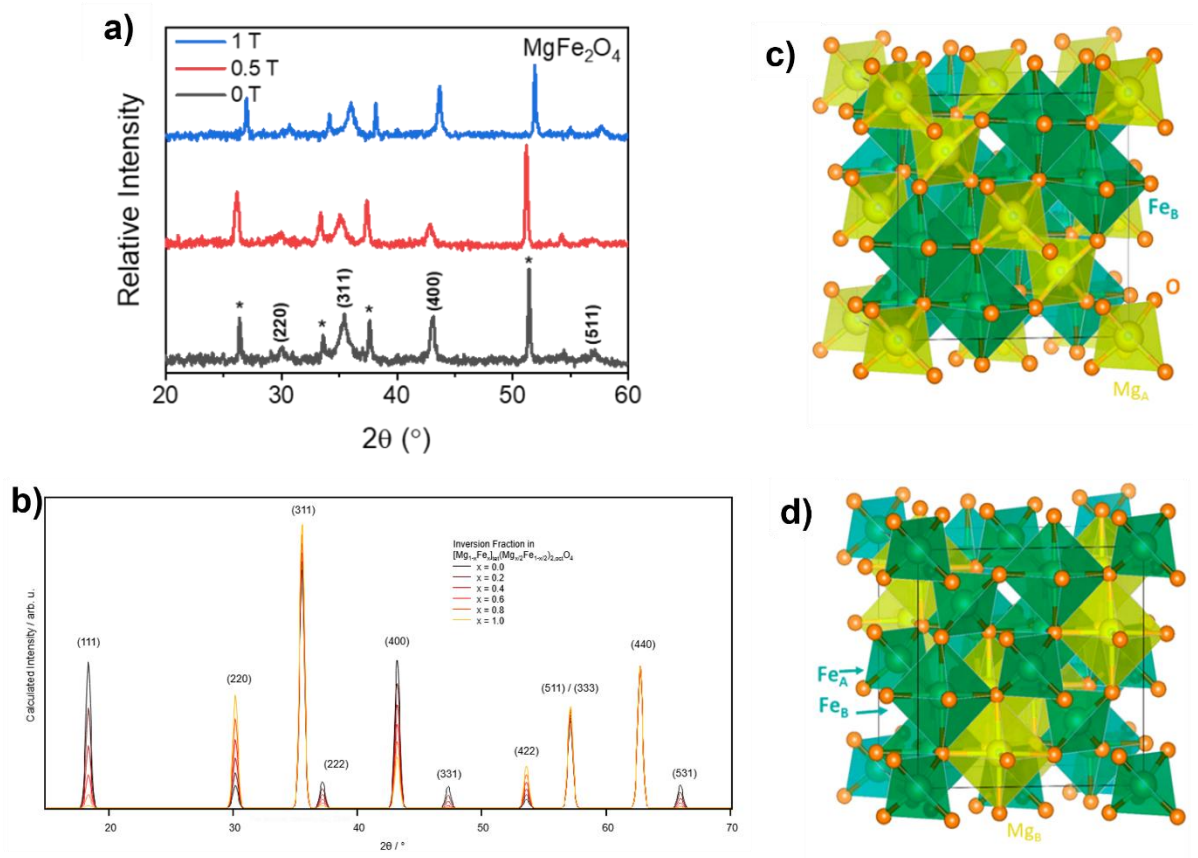

Figure 22 (a) XRD pattern of CVD grown $MgFe_2O_4$ under 0, 0.5 and 1 T magnetic field ($T_{substrate}$ = 500 °C, $T_{precursor}$ = 180 °C, $t_{deposition}$ = 20 min), (b) Simulated XRD pattern as a function of the degree of inversion Crystal structure of $MgFe_2O_4$ with (c) normal spinel and (d) inverse spinel structure.

The XRD patterns (**figure 22(a)**) demonstrated the successful deposition of $MgFe_2O_4$ thin films via the mfCVD technique, showing characteristic diffraction peaks at 30.01°, 35.46°, 43.14° and 57.04° corresponding to the (220), (311), (400) and (511) planes, respectively, in agreement with the reference data (JCPDS# 01-088-1938). All three films frown under different magnetic field strengths exhibited similar diffraction patterns and overall phase structures, suggesting that the spinel phase formation was favorable across all magnetic

intensities. However, a resilience in the (400) peak intensity was observed as the applied magnetic field increases up to 1.0 T.

For comparison, the simulated XRD patterns (**figure 22(b)**) displayed a systematic attenuation of the (400) peak as a function of the degree of inversion in the spinel lattice. Then comparing the experimental and simulated XRD data, the increased (400) intensity at 0 T and 1.0 T indicates a lower degree of inversion close to normal spinel structure in **figure 22(c)**. Whereas the reduced (400) peak intensity at 0.5 T represents a higher degree of inversion close to inverse spinel structure in **figure 22(d)**. This magnetic field-dependent tunability of the inversion degree is consistent with the X-ray magnetic circular dichroism (XMCD) results (discussed below), which show correlated variations in magnetic moment, further supporting the magnetic field-induced modulation of cation distribution within the $MgFe_2O_4$ spinel structure.

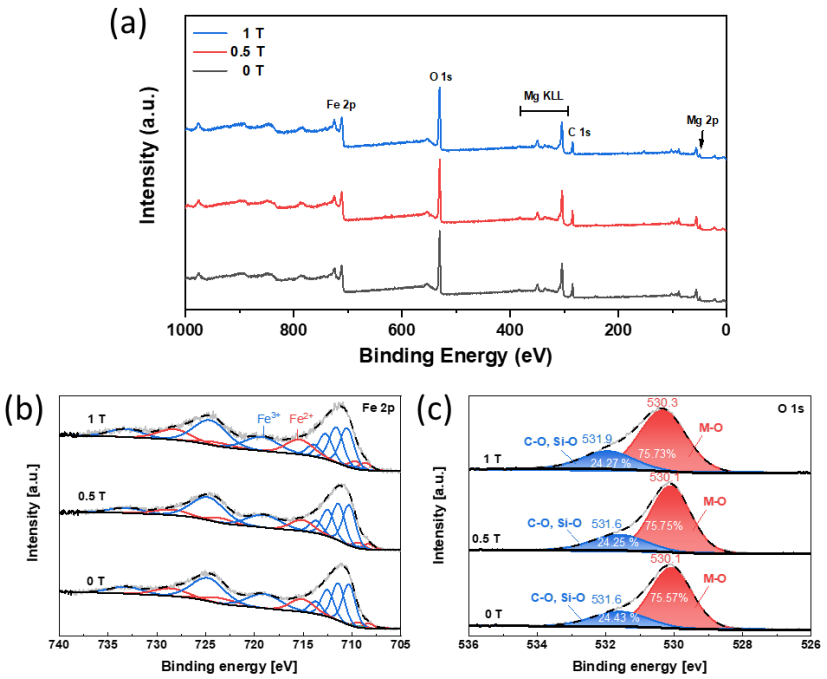

Figure 23 The X-Ray photoelectron spectroscopy (XPS) analytical data representing (A) a survey spectrum, (B) Fe 2p, and (C) O 1s of deposited $MgFe_2O_4$ films via mfCVD of precursor $[MgFe_2(O^tBu)_8]$ with different field strength (B = 0, 0.5, and 1 T).

The X-Ray photoelectron spectroscopy (XPS) analysis confirmed the presence of magnesium, iron and oxygen in all three $MgFe_2O_4$ samples, along with small amounts of carbon, which likely originated from residual precursors fragments deposited on the inner walls of the CVD chamber (**figure 23(a)**). The high resolution Fe 2p spectra exhibited a main peak centered at 710.3 eV, characteristic of Fe^{3+} species, accompanied by a satellite feature near 719 eV, further corroborating the dominant trivalent oxidation state of iron.

Additionally, a minor component at 708.3 eV corresponding to Fe^{2+} was detected, suggesting either a partial field-induced chemical reduction or the formation of antisite defects, where Fe^{2+} ions occupy Mg^{2+} lattice positions.[104]

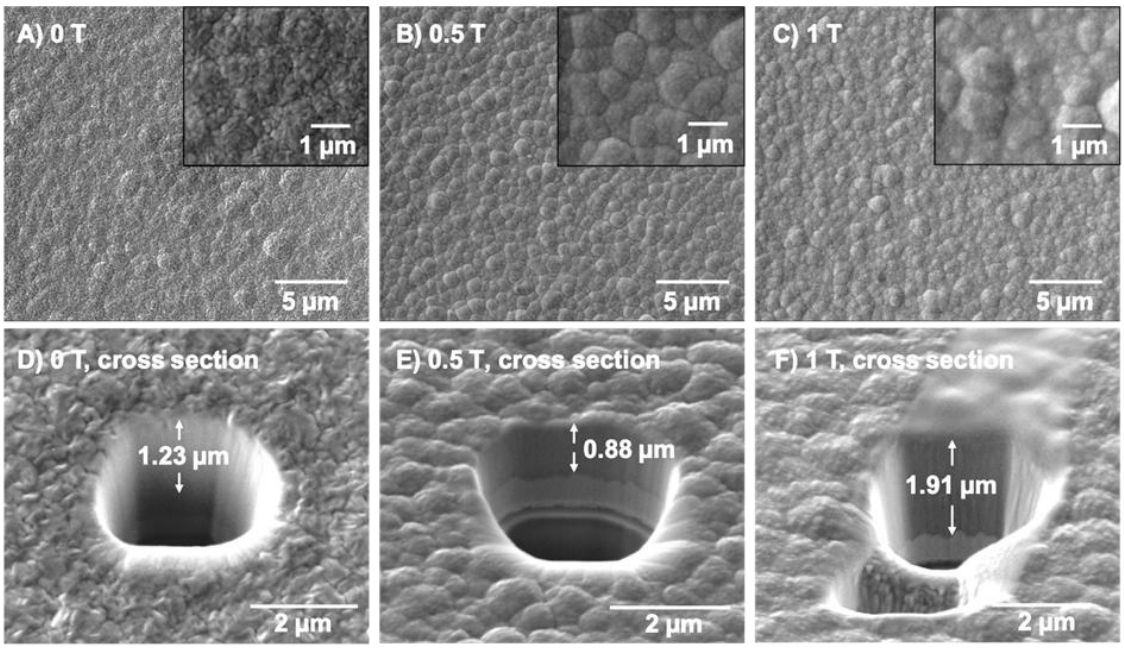

Figure 24 FIB-SEM images of deposited films using precursor $[MgFe_2(O^tBu)_8]$ in CVD with zero-field (A), 0.5 T (B), and 1 T (C) perpendicular to the precursor flow as well as a cross-section of $MgFe_2O_4$ films (D: 0 T, E: 0.5 T and F: 1 T).

The application of an external magnetic field significantly influenced the grain size, as analyzed by dual-beam focused ion beam scanning electron microscopy (FIB-SEM) (**figure 24**). The as-grown films exhibited uniform and continuous $MgFe_2O_4$ coverage on the FTO substrates. In contrast, the films deposited under a perpendicular magnetic field (**figure 24(b) and (c)**) displayed larger grain sizes and more distinct grain boundaries compared to the zero-field grown $MgFe_2O_4$ films (**figure 24(a)**). These observations suggest that the magnetic field influences surface diffusion and nucleation kinetics during film growth, leading to modified grain morphology. Across the various magnetic field intensities, the $MgFe_2O_4$ films uniformly spreads throughout the substrate. Such uniformity ensures intimate contact with the electrolyte, preventing partial exposure that could lead to inaccurate electrochemical measurements in PEC water splitting. Therefore, given that Fe_2O_3 films deposited by mfCVD under various magnetic field intensities have been successfully employed as photoanodes, the $MgFe_2O_4$ films are also expected to be suitable for PEC water splitting applications. While magnetic field-induced variations in grain density and crystallite size have been reported previously, the detailed mechanisms governing theses effects in mfCVD remain poorly understood.[100]

Quantitative surface analysis using ImageJ software revealed approximately 2-3% surface porosity in MFO films frown under zero-field conditions, whereas no detectable porosity was observed in the films deposited at 0.5 T and 1 T. Cross-sectional FIB-SEM images (**figure 24(d-f)**) did not show a clear trend in overall film thickness. However, the $MgFe_2O_4$ film deposited at 1 T exhibited the maximum thickness of 1.91 µm, compared to 1.23 µm at 0 T and 0.88 µm at 0.5 T.

3.1.3 Spectroscopic investigations of the effects of magnetic field on the $MgFe_2O_4$ film

According to Granone *et al.*[105] the degree of inversion in $ZnFe_2O_4$ spinel affects its optical properties. Their work demonstrated that $ZnFe_2O_4$ with a high degree of inversion exhibits a broader Raman feature around 176.5 cm^{-1}, corresponding to the vibration of tetrahedral site, compared to $ZnFe_2O_4$ with a low degree of inversion. This behavior was attributed to the occupation of the tetrahedral site by the lighter Fe atom rather than Zn. Likewise, $MgFe_2O_4$ films display distinct optical properties depending on degree of inversion as shown in **figure 25**.

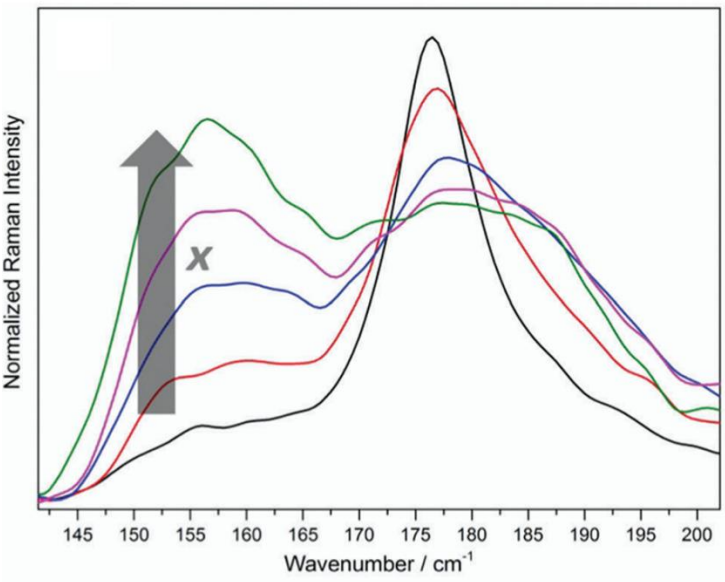

Figure 25 Raman spectra of $ZnFe_2O_4$ spinel with increasing degree of inversion (x). Adapted from ref. [105].

Figure 26 shows the UV-Vis absorption spectra of the $MgFe_2O_4$ (MFO) films as a function of the applied magnetic field. The all three samples represent same absorption response approaching to UV range. However, MFO – 0 T and MFO – 1.0 T show broader absorption spectra going further to visible light range. Based on the X-ray diffraction (XRD) results in **figure 22**, the UV-vis results indicate that $MgFe_2O_4$ close to normal spinel wider range of UV-

vis spectra than $MgFe_2O_4$ close to inverse spinel. Therefore, it is beneficial to let $MgFe_2O_4$ have low degree of inversion to develop functional $MgFe_2O_4$ for photoelectrochemical (PEC) water splitting.

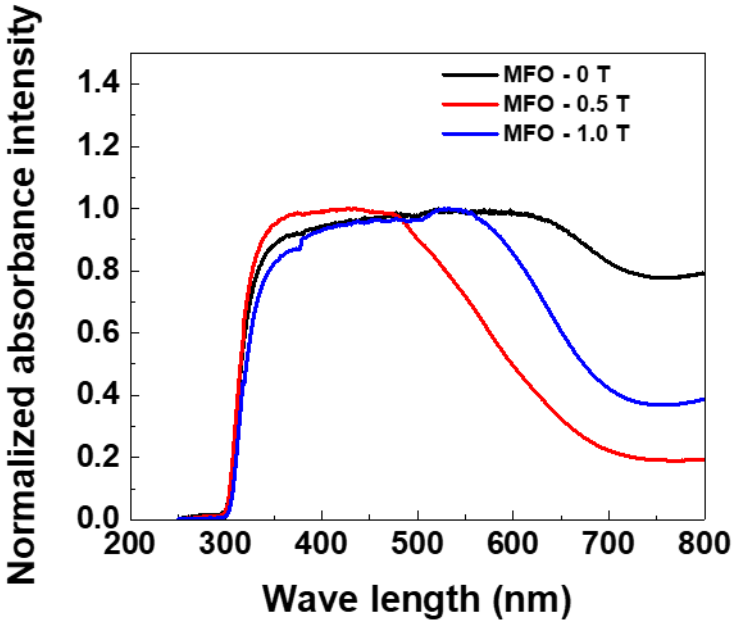

Figure 26 UV-vis absorption spectra of the $MgFe_2O_4$ films deposited on FTO substrate.

While both MFO – 0T and MFO – 1.0 T are relatively normal spinel as compared to MFO – 0.5 T based on the XRD results in **figure 22**, MFO – 1.0 T shows narrow absorption spectra than MFO – 0 T in **figure 26**. It might be attributed that although increasing magnetic field intensity over 0.5 T recover degree of inversion to normal spinel, the intensity is insufficient to completely form the initial normal spinel.

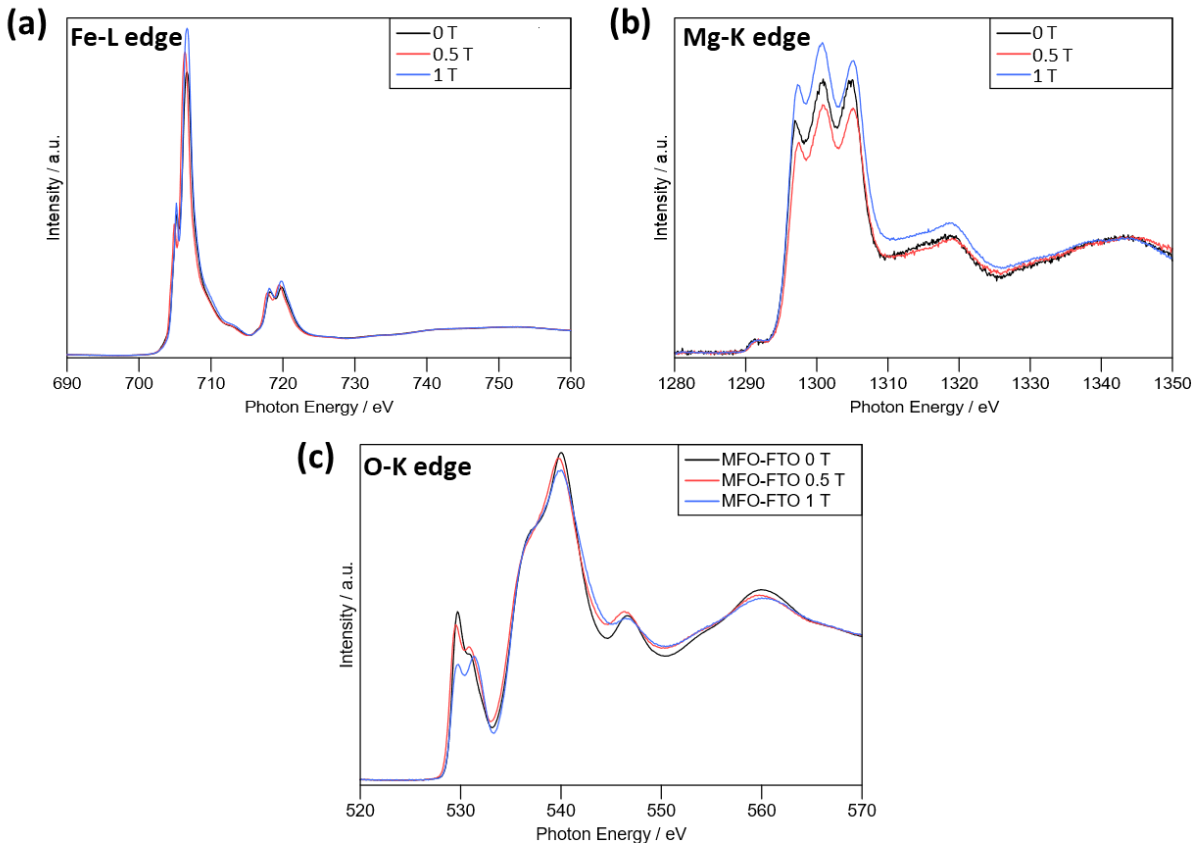

Figure 27 XAS results for Fe-L (a), Mg-K (b), and O-K (c) edges of $MgFe_2O_4$ deposited under different magnetic fields.

From the perspective of local atomic and electronic structure, investigated by X-ray absorption spectra (XAS), both the Fe-L and Mg-K edges (**figure 27(a) and (b)**) exhibited only minor variations with respect to the applied magnetic field during deposition. The changes in both the white line (maximum) intensity and energy of the Fe L3 edge (**figure 27(a)**) (~707 eV) could not be compared due to the charging of the samples, which leads to distortion at high-intensity levels. In general, the spectra are quite similar and are in line with a d5 electronic configuration (indicating Fe^{3+}).

The Mg-K edge spectra (**figure 27(b)**) displayed minimal field dependence. Apart from a change in the absolute intensity of the triplet feature near 1300 eV, no significant differences

were observed across the samples. The spectral characteristics, primarily determined by the local symmetry around Mg^{2+}, closely resembled those of enstatite and diopside, in which Mg occupies octahedral coordination sites. This observation supports that the $MgFe_2O_4$ films grown via mfCVD adopt a spinel structure with a substantial degree of inversion. The variation in inversion fraction with applied magnetic field suggested by the intensity changes of the (400) reflection in XRD appears to be only marginally supported by the XAS results, as the overall spectral profiles remained nearly unchanged. However, the most interesting aspect is the O-K-edge spectra (**figure 27(c)**) which showed a decrease in the pre-edge peak at ~529 eV in samples deposited under 1 T.

This region is related to the octahedral Fe-O environment, where the electronic states make up most of the region of the fermi level and are of O 2p origin constituted by nonbonding orbitals on O atoms to antibonding t_{2g} orbitals of Fe atoms. The decrease of the pre-peak feature, in simple terms, suggests a depletion of charge carries, as the lowest unoccupied molecular orbital (LUMO) that is accessed here is a direct measure of the hole concentration. The suppression of the (400) peak with increasing magnetic field strength, as observed in the XRD patterns, implies that the applied magnetic field influenced the crystal facet orientation and induced preferential lattice growth in the $MgFe_2O_4$ films. Alternatively, it could reflect field-dependent redistribution of Mg^{2+} and Fe^{3+} ions between tetrahedral and octahedral sites, consistent with an enhanced degree of inversion as also indicated by the simulated XRD date (**figure 22(b)**) at 0.5 T. These structural observations are in good agreement with the XAS and UV-Vis spectroscopy results, where the MFO – 0 T sample exhibited broader optical absorption across the visible region. This behavior is indicative of a higher population of Fe^{3+} ions octahedral coordination, corroborating the field-dependent inversion phenomena inferred from both structural and spectroscopic analyses.

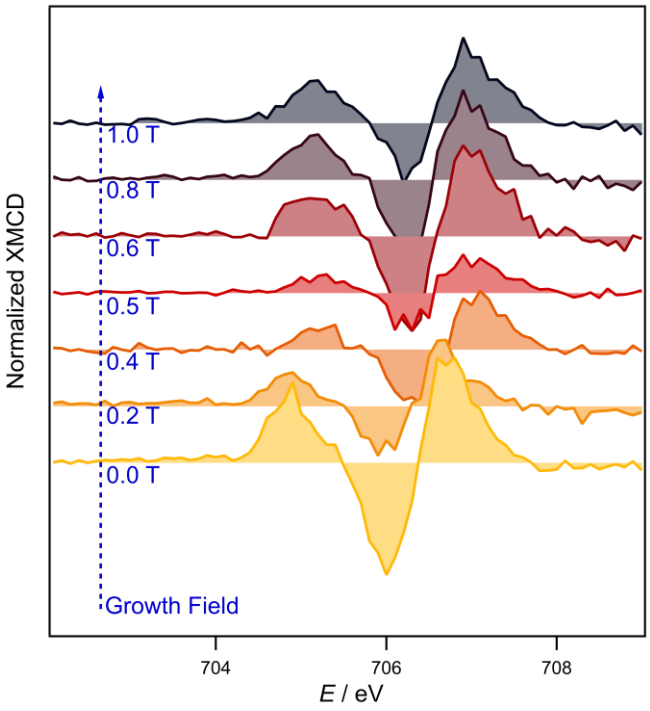

Figure 28 Normalized XMCD spectra of MFO thin films deposited under 0 T - 1 T magnetic fields.

Further insight into the element-specific magnetic properties of the $MgFe_2O_4$ films was obtained from X-ray magnetic circular dichroism (XMCD) measurements, which probe the spinel structure, the Fe 2p to 3d electronic transition is induced by X-ray photons of approximately 700 eV, providing direct information on the magnetic properties of the 3d states, which are responsible for the overall magnetic behavior of the material.

As shown in **figure 28**, the XMCD spectra revealed a progressive decrease in magnetic moment with increasing external magnetic field strength during deposition, up to 0.5 T. This reduction in magnetic moment correlates with the higher degree of inversion within the spinel lattice observed at the same field strength. Interestingly, at 1 T, the XMCD signal intensity increased again, indicating a partial recovery of the Fe magnetic moment.

These findings are consistent with previous reports, which showed, based on Fe-L edge spectra, that the occupancy of Fe^{3+} ions in octahedral sites differs between magnetized and non-magnetized films, implying that magnetization directly affects the cation distribution and degree of inversion in the spinel structure.

The observed non-linear dependence of the inversion degree on the applied magnetic field likely arises from the competition between two opposing mechanisms. On one hand, the applied magnetic field (1 T) influences film growth dynamics, for instance, though interactions with the precursor flux, absorbed species or nucleation intermediates, thereby modifying the cation arrangement. On the other hand, the field strength used here is insufficient to induce solid-state cation rearrangements, as expected during magnetic annealing. Achieving such effects might require stronger magnetic fields capable of overcoming ion migration barriers, which were beyond the capabilities of the present experimental setup.

3.2 Interfaical voltage drop ($V_{interface}$) characteristics in non-faradaic and faradaic reaction

In the previous chapter, cation disorder (indicating degree of inversion) in $MgFe_2O_4$ spinel was shown to be tunable by applying an external magnetic field during chemical vapor deposition, as evidenced by X-ray spectroscopic analyses. Moreover, the tunability in degree of inversion suggested the possibility of enhancing the photoelectrochemical (PEC) water splitting performance of $MgFe_2O_4$, as indicated by the expanded UV-vis absorption spectra toward the visible light rage for the normal spinel. Despite these efforts to improve PEC functionalities, an alternative strategy is needed to accurately evaluate a photoanode, accountinf for the underestimation of photocurrent caused by voltage losses in a PEC water splitting cell.

In a PEC water splitting cell, the photoanode is immersed in an electrolyte, forming the semiconductor/electrolyte interface, as illustrated in **figure 6**. When a voltage is applied by an external power source, an overall voltage drop ($V_{overall}$) develops across the PEC cell. The voltage drop at the semiconductor/electrolyte interface ($V_{interface}$) represents a fraction of $V_{overall}$ and serves as an output parameter in response to the applied voltage.

During non-faradaic reactions, where no chemical transformation occurs and only charge accumulation takes place, $V_{interface}$ corresponds to the charge transfer voltage drop (V_{ct}), which arises when charges transfer across the interface. In contrast, during faradaic reactions, where the oxygen evolution reaction (OER) given by eq. (1.1) occurs, $V_{interface}$ includes both V_{ct} and the pH-gradient voltage drop (V_{pH}) generated as a result of the reaction. Notably, when electrolytes containing abundant proton donors or acceptors are employed, the pH gradient is confined near the interface, facilitating quantification of V_{pH}, as described in the section 2.5.

In this section, the methods for estimating V_{ct} during non-faradaic reactions and V_{pH} during faradaic reactions are introduced. Furthermore, the evaluation of catalytic efficiency based on the measured V_{pH} is discussed.

3.2.1 $V_{interface}$ in non-faradaic reaction

The favorable energy band structure of TiO_2 enables its widespread application in photoelectrochemical (PEC) water splitting.[32,106,107] Park et al. confirmed that TiO_2 overlayer on photoanodes favors selective hole transfer to $WO_3/BiVO_4$ heterosturucture, thus improving photocurrent density. Furthermore, the TiO_2 as a passivation layer allows to keep the photocurrent density stable as shown in **figure 29**.[31] Therefore, TiO_2 is selected as a suitable photoanode in this work.

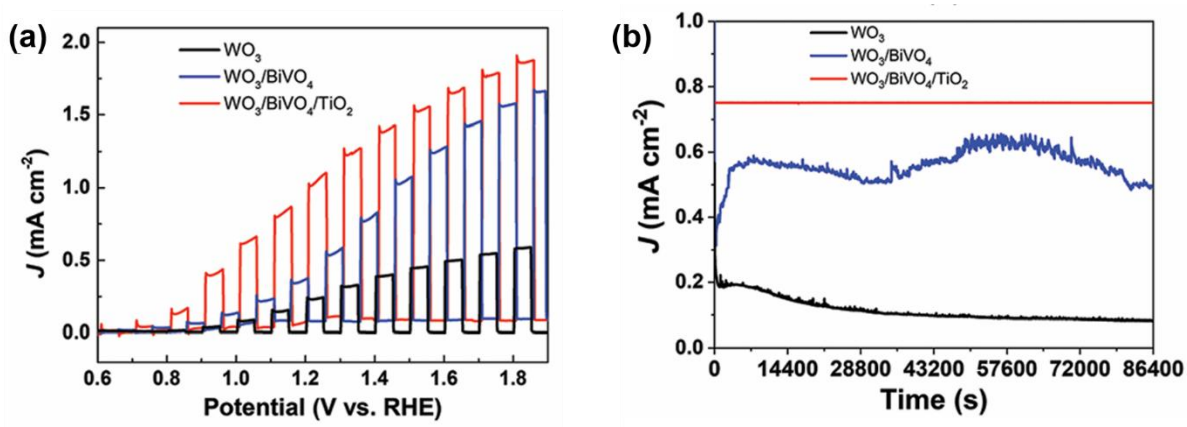

Figure 29 (a) Linear sweep voltammetry and (b) chronoamperometry curves of WO_3, $WO_3/BiVO_4$ and $WO_3/BiVO_4/TiO_2$ photoanodes. Adapted from ref. [31].

The uniform deposition of TiO_2 for a photoanode in **figure 30(a)** and **(b)** enables to form TiO_2/liquid interface in entire contact to electrolyte and water splitting throughout the interface under illumination.

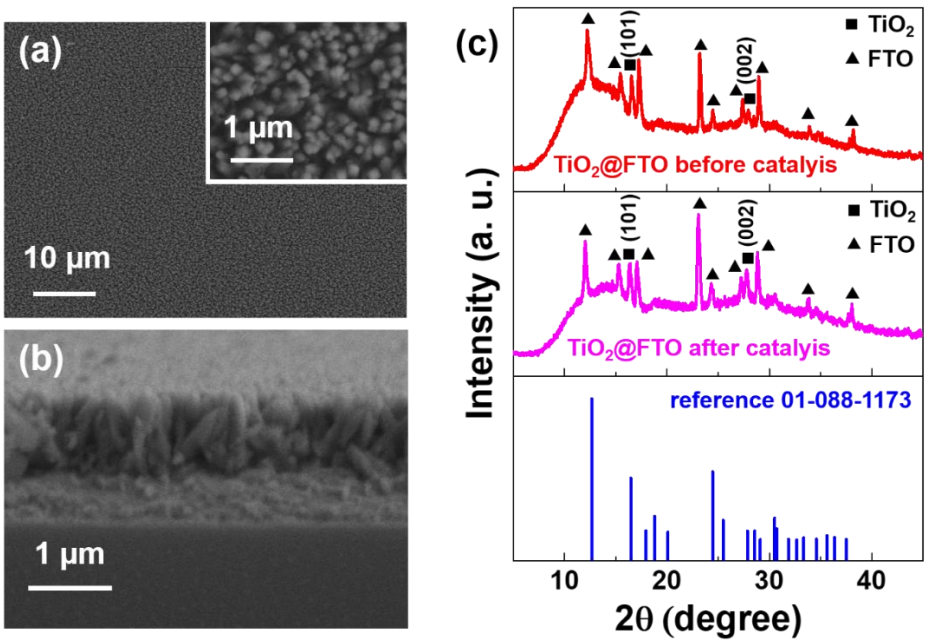

Figure 30 SEM images of (a) the top surface and (b) cross-sectional view of the deposited TiO_2 film. The inset is the enlarged top surface view. XRD patterns of the deposited TiO_2 film on FTO before and after catalysis (top and middle panel, respectively) and rutile TiO_2 reference (bottom panel). The XRD patterns in the middle panel are measured after the catalysis performed in this work.

Rutile TiO_2 is confirmed as the crystal structure of the deposited TiO_2 on FTO substrate by the X-ray diffraction (XRD) patterns in the top panel of **figure 30(c)**. The middle panel in **figure 30(c)** still shows rutile phase although it is measured after the catalysis which will be dicussed in the following sections. The structural consistency in the absence of residual phase proves chemical stability of the deposited TiO_2 film. Due to its stability, TiO_2 is widely used as a passivation layer. Therefore, parasitic voltage losses inducing phase transformation are not expected.[108,109] Despite the superior photoactivity of anatase TiO_2, the rutile phase exhibits greater chemical stability.[110–112]

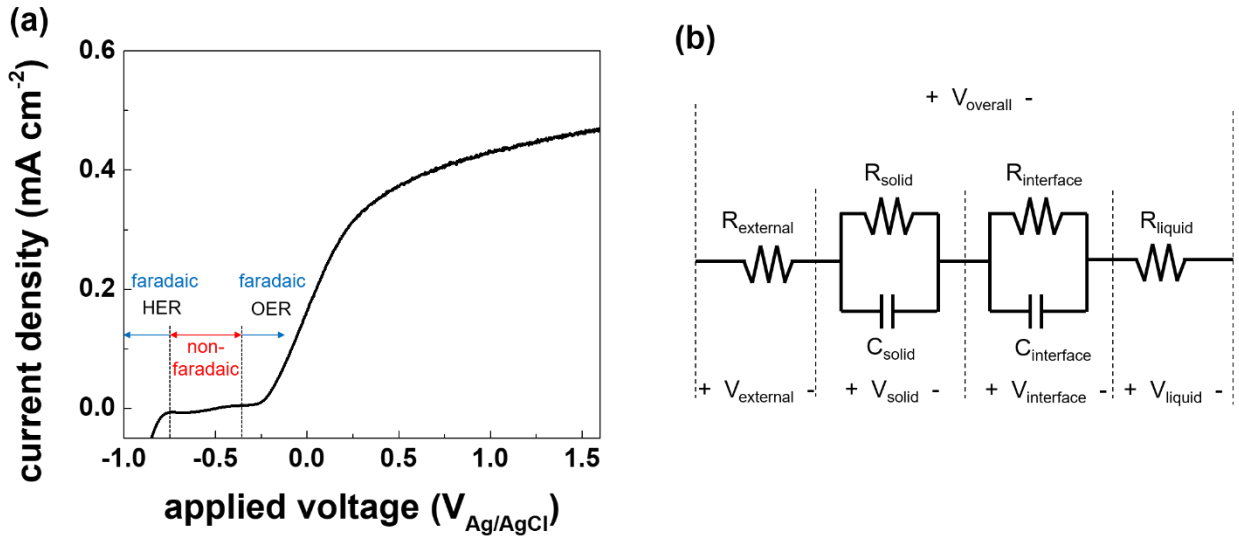

Figure 31 (a) Current-voltage characteristics of the TiO_2 film in 0.1 M sodium phosphate buffer (pH 7) under illumination and (b) a typical equivalent circuit of a photoelectrochemical water oxidation cell.

In PEC water splitting reaction, applied voltage (V_a) ranges are distinguished into the ranges inducing non-faradaic reaction and faradaic reaction represented as plateau and steep region, respectively in linear sweep voltammetry (LSV) curve.[68,113,114] In this context, non-faradaic reaction is shown at -0.7 V < V_a < -0.3 V where insignificant change in current density over V_a is evolved as shown in **figure 31(a)**. Hydrogen evolution reaction (HER) and oxygen evolution reaction (OER) before and after the plateau are evolved as faradaic reactions under -0.7 V and over -0.35 V, respectively.

Figure 31(b) shows an equivalent circuit model widely applied for a PEC water splitting cell operating half-cell reaction and employing a semiconductive metal oxide electrode. The equivalent circuit model consists of a series resistance and two parallel connected RC elements formed by charge transfer and accumulation at the bulk and solid/liquid interface.[24,115,116]

The measured current density in **figure 31(a)** represents current density consumed by the circuit elements where the voltage drops at solid bulk (V_{solid}) and series resistance (V_{series}) are formed.[82,117] As seen in **figure 31(a)**, because the insignificant change in current density over the plateau region indicates non-faradaic reaction, the voltage drop at the semiconductor/electrolyte interface, $V_{interface}$ is replaced by the charge transfer voltage drop, V_{ct}. In contrast, because the steep change in current density indicates faradaic reaction that protons are produced by OER following eq. (1.1), the pH-gradient voltage drop (V_{pH}) is contributing to $V_{interface}$ in addition to V_{ct}.

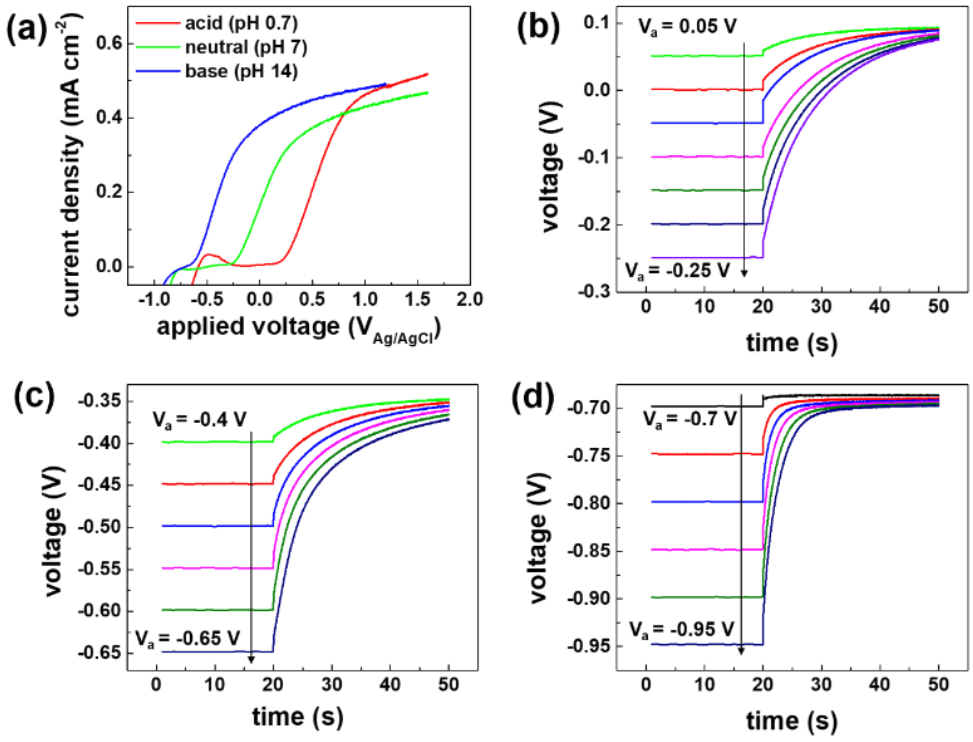

Figure 32 (a) LSV curves of the TiO_2 film measured in acidic (0.1 M H_2SO_4, pH 0.7), neutral (0.1 M sodium phosphate buffer, pH 7) and basic (0.1 M KOH, pH 14) under illumination. Voltage drop decays of the TiO_2 film resulting from non-faradaic reaction in (b) acid, (c) neutral and (d) base under illumination.

To investigate characteristics of the voltage drop components, LSV curves are measured at different pH values and the V_a ranges for non-faradaic reaction are determined by finding plateau regions in **figure 32(a)**. The proton extraction is reported to be observed at -0.6 V with respect to the saturated hydrogen electrode (approximately -0.4 $V_{Ag/AgCl}$) in 0.1 M H_2SO_4.[118] Therefore, the current bump in the LSV curve measured in acidic condition is attributed to electrochromic effect occurred by proton extraction in TiO_2 lattice.[68]

The voltages corresponding to the plateau regions are applied and voltage drop decay curves induced by non-faradaic reaction are obtained at the individual pH until the system is re-

equilibrated in **figure 32(b-d)**. Since electron is the majority charge carrier of n-type semiconductor (TiO_2 in this case), its mobility and diffusion are in charge of polarization and polarization decay.

Diffusion coefficient of electron in TiO_2 reaches ~10^{-4} cm^2 s^{-1} under well-crystallized and continuous photo-excitation conditions.[119] Diffusion coefficient of proton in aqueous solution is ~10^{-5} cm^2 s^{-1}, the highest value among ionic species and therefore, proton transport is primarily considered in electrolyte.[55,120] The higher diffusion coefficient of a charge carrier is, the faster polarization decays. Regarding equivalent amount of counter charges is formed at the interface of both solid and liquid, the overall re-equilibration at the solid/liquid interface is predominantly governed by the slower transport characteristics of the liquid side.[121] It is concluded that because re-equilibration from polarization in bulk region of TiO_2 is faster than that of the solid/liquid interface, the tail part of the voltage drop decay curve corresponds to $V_{interface}$ which is replaced by V_{ct} in non-faradaic reaction (**figure 32(b-d)**).[122]

In this context, the voltage drop decay in basic condition approaches to the open circuit voltage (V_{oc}) faster than in neutral and acidic condition, meaning $V_{interface}$ barely forms in basic condition. The insignificant $V_{interface}$ in basic condition results from the formation of a weak electrical double layer due to low H^+ concentration. While the voltage drop decay in basic solution reaches V_{oc} within 10 seconds, the voltage drop decay in neutral and acidic solution keeps approaching to V_{oc} beyond this time. Therefore, the voltage drop decay after t = 30 s is assigned to $V_{interface}$. Since the formation of the insignificant $V_{interface}$ indicates most of voltage drop is assigned to V_{solid}, and the voltage drop sharply decays within 2 seconds, the voltage drop during 2 seconds after the initial instant voltage drop corresponds to V_{solid}.

The bulk region of the semiconductor is typically regarded as a neutral region, where charge carriers are counterbalanced and no internal electric field exists. Consequently, photogenerated

carriers are expected to recombine almost instantaneously. However, when an external bias is applied, an electric field is established across the bulk region, enabling the separation of photogenerated electrons and holes. This separation gives rise to a measurable voltage drop. Once the external bias is removed, the stored potential gradually dissipates as the separated charges recombine. This decay process is observed as the OCP decay transient.

Table 2 Voltage drop values selected from figure 32.

pH	V_{oc}	V_a	$\Delta V = V_a - V_{oc}$	V_{solid}
0.7 (acidic)	0.100	0.000	-0.100	-0.016
7.0 (neutral)	-0.350	-0.450	-0.100	-0.021
14.0 (basic)	-0.700	-0.800	-0.100	-0.081

The V_{solid} values in all solutions are obtained at the same formed voltage with respect to V_{oc} (ΔV) in table 2. It is found that the V_{solid} in basic solution is the highest and close to ΔV, indicating that most of the voltage drop forms in the solid phase because ΔV means apparent voltage drop formed by applied voltage.

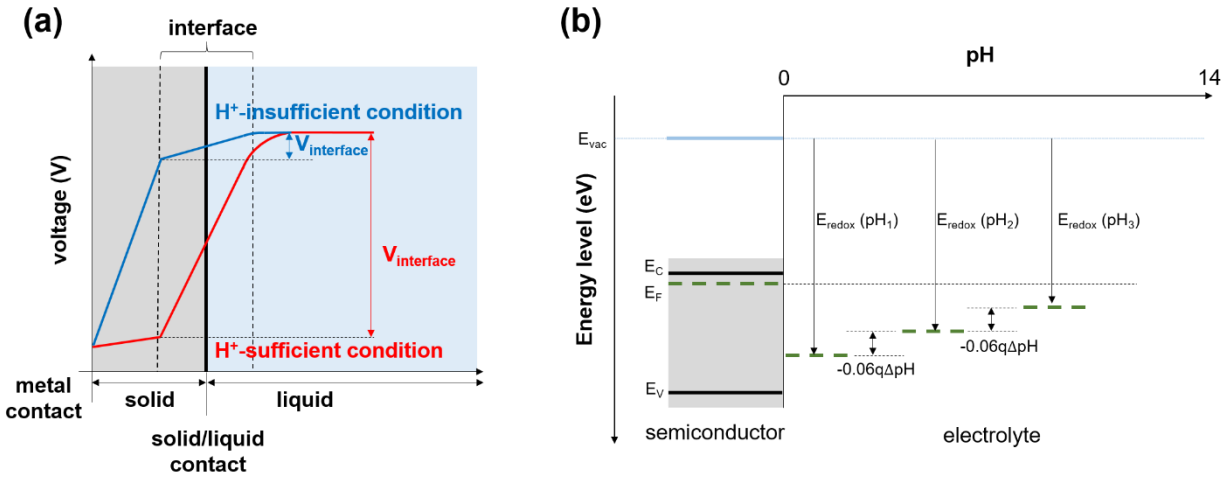

Figure 33 (a) Schematic image of voltage drop distributions depending on H^+ concentration and (b) energy band diagram of an n-type semiconductor as a photoanode and electrolyte depending on pH in a PEC water splitting system before equilibrium without illumination. E_{vac} is vacuum energy level. E_c and E_v are energy levels of conduction and valence band edges. E_F is Fermi level of the n-type semiconductor E_{redox} is redox level of the electrolyte.

The investigations in **figure 32** enables to qualitatively determine voltage drop distribution depending on H^+ concentration and decouple the overall voltage drop decay transients into the voltage drop components at the equivalent circuit in **figure 31(b)**. The H^+ concentration is distinguished as H^+-insufficient and sufficient condition. While V_{solid} is small as compared to $V_{interface}$ in H^+-sufficient condition, V_{solid} remains more predominant than $V_{interface}$ in H^+-insufficient condition (**figure 33(a)**). It is attributed to the variable redox level of solution depending on pH. Due to the increasing difference between E_F and E_{redox} approaching to acidic condition in **figure 33(b)**, while $V_{interface}$ to be formed in contact with solid and liquid keeps increasing, V_{solid} keeps decreasing.[68]

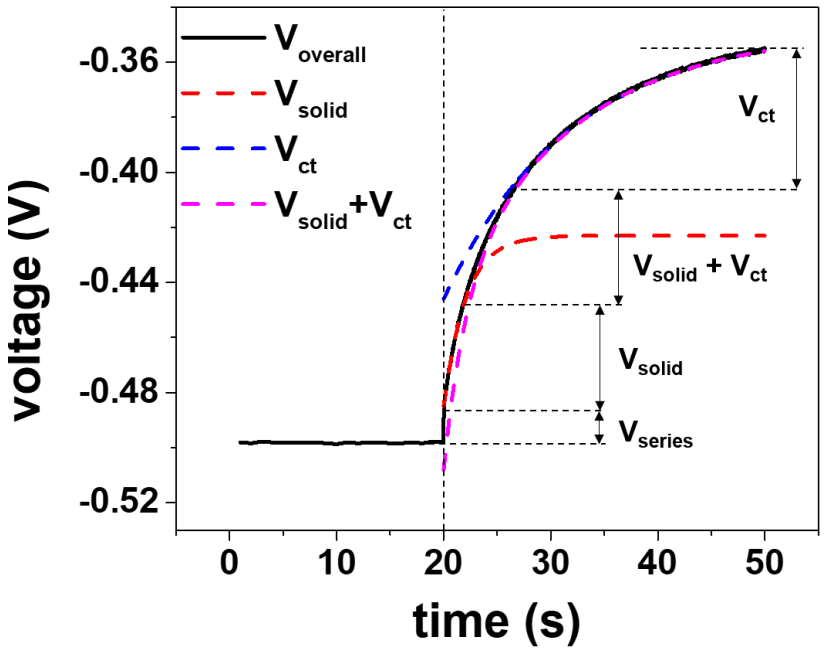

Figure 34 The voltage drop decay curve resulting from non-faradaic reaction measured at -0.5 V in figure 32(c).

The overall voltage drop decay resulting from non-faradaic reaction is expressed by contributions of each part of the voltage drop components in **figure 34**. The vertical decrease immediately after the constant voltage is assigned to the voltage drop (V_{series}) formed at the series resistance. Since voltage drop at series resistance is governed by Ohm's law and time-independent factor, the V_{series} instantaneously responds to change in applied voltage.[45] The V_{solid} and $V_{interface}$ correspond to voltage drops formed at the RC elements of the system, and both exhibit mono-exponential decay over time. V_{solid} is dominant within the first 2 seconds starting the decay. As previously defined, in the case of a non-faradaic reaction, $V_{interface}$ is replaced by V_{ct}, and the voltage drop observed after t = 30 s corresponds to the V_{ct}. The characterization of these components is confirmed by the fact that the sum of V_{solid} and $V_{interface}$ (a bi-exponential decay curve) closely matches the experimentally observed $V_{overall}$ curve. The

small deviation approaching to $t_d = 0$ from the tail part is attributed to the contribution of V_{solid} fitting alone to $V_{overall}$ at the beginning part of the decay where both V_{solid} and V_{ct} affect. Nevertheless, the small deviation indicates larger V_{ct} forms than V_{solid} due to the H^+-sufficient condition, which aligns with **figure 33(a)**.

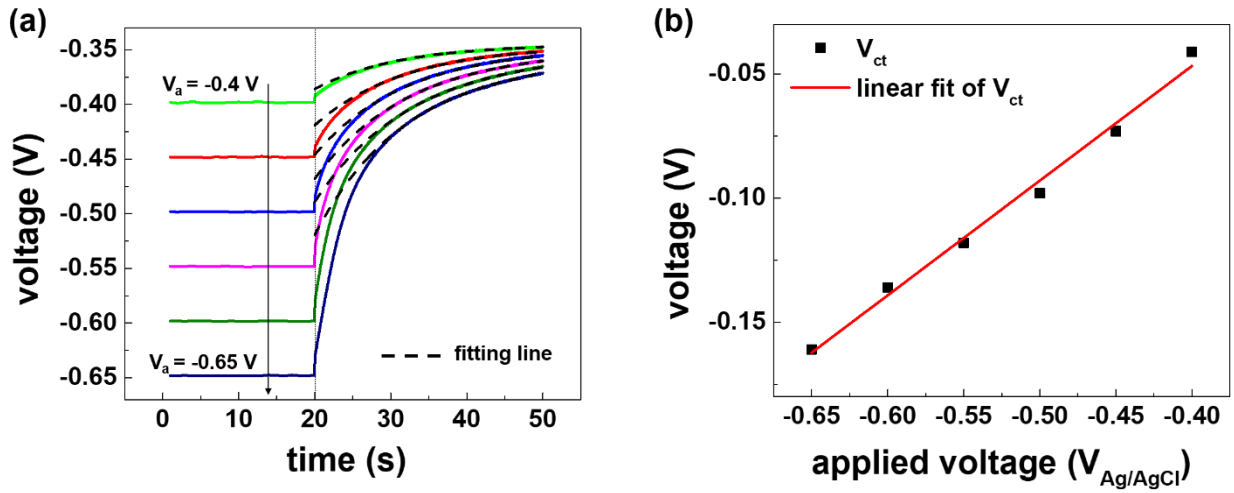

Figure 35 (a) Voltage drop decays of the TiO_2 film resulting from non-faradaic reaction depending on applied voltage in 0.1 M sodium phosphate buffer (pH 7) under illumination and (b) estimated charge transfer voltage drop.

The time-dependent V_{ct} follows an exponential decay with a characteristic time constant, as described by the following equation:

$$V_{ct}(V_a, t_d) = V_{ct}(V_a)e^{-t_d/\tau} + V_{oc} \qquad (3.1)$$

where t_d denotes the decay starting time ($t_d = t - 20$). Eq. (3.1) accurately reproduces the voltage drop decay curve obtained from the non-faradaic reaction after t = 30 s, as shown in **figure 35(a)**. Extrapolation of the fitted curve enables quantitative analysis of the time-dependent

behavior of V_{ct}. The pre-exponential factor in eq. (3.1) corresponds to the V_a-dependent V_{ct} at t_d = 0 s, which represents the formed V_{ct} when voltage is applied. Extraction of these factors from decay curves recorded at various V_a values reveals a clear linear dependence, as shown in **figure 35(b)**. This relationship is expressed as V_{ct} = 0.462 V_a + 0.138 by fitting a linear curve to the data.

Under open circuit condition, no voltage forms at the solid/liquid interface. Substituting V_{ct} =0 V into the V_{ct}-V_a equation gives V_a = -0.3 V, which corresponds to V_{oc}. This calculated value deviates by only 0.05 V from the measured V_{oc} (-0.35 V, the converged value in **figure 35(a)**), thereby confirming the accuracy of the V_{ct}-V_a relationship. The reliability of this equation validates its use for subsequent derivation of V_{pH}. Verification of V_{oc} through this approach is therefore an essential step in establishing the methodology.

3.2.2 Time constant in discharging process

Time constants of the bulk in solid and interface part during the open circuit potential (OCP) decay are investigated to quantitatively determine the time when either voltage drop at semiconductor bulk (V_{solid}) or charge transfer voltage drop (V_{ct}) is dominant. The time constant measured during voltage drop decay is defined as decay time constant, τ_d. Since the bulk in solid and interface part form RC circuits as shown in **figure 31(b)**, the two parts represent each τ_d during discharging process as described in **figure 17**.[49]

The meaning of τ_d is understood based on the following derivation. When the voltage drop formed at RC circuit is v_c, as explained in **figure 17**, the voltage drop decay transient is

$$v_c(\mathrm{t}) = V_0 e^{-t/\tau_d} \qquad (3.2)$$

where V_0 is pre-exponential factor corresponding to $v_c(\mathrm{t})$ at $\mathrm{t} = 0$. The differential form of eq. (3.2) is

$$v_c'(t) = -\frac{V_0 e^{-t/\tau_d}}{\tau_d} = -\frac{v_c(t)}{\tau_d} \qquad (3.3)$$

Eq. (3.3) indicates the slope of $v_c(\mathrm{t})$ at any t. Therefore, the denominator means time when $v_c(\mathrm{t})$ decays. The larger τ_d is, the longer $v_c(\mathrm{t})$ decays.

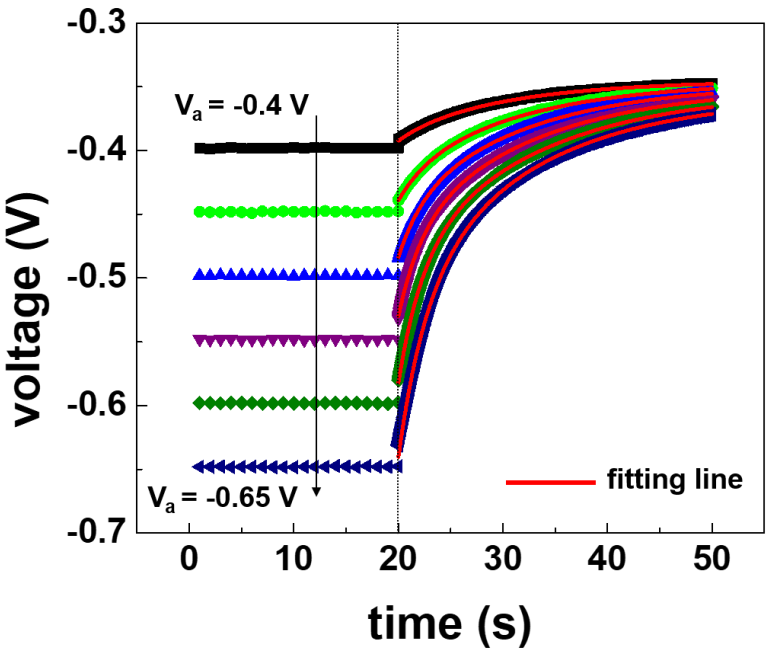

Figure 36 Bi-exponential fitting (eq. (3.4)) of the curves in figure 35(a).

The overall voltage drop decay curves resulted from non-faradaic reaction in **figure 35(a)** are bi-exponential forms consisting of $V_{solid}(\mathrm{t})$ and $V_{ct}(\mathrm{t})$

$$V_{overall}(\mathrm{t}) = V_{solid}(\mathrm{t}) + V_{ct}(\mathrm{t}) = V_{solid}(0)e^{-t/\tau_{d,solid}} + V_{ct}(0)e^{-t/\tau_{d,ct}} \qquad (3.4)$$

The beginning part of the decay showing sharp decrease includes contributions of both $V_{solid}(t)$ and $V_{ct}(t)$. Therefore, the approximation of the summation curve of $V_{solid}(t)$ and $V_{ct}(t)$ in **figure 34(b)** shows small deviation approaching to the beginning part of the decay from the tail part. To obtain correct fitting curve corresponding to $V_{solid}(t)$ from the overall voltage drop decay curve in non-faradaic reaction, the already obtained $V_{ct}(t)$ in **figure 35(a)** is substituted in eq. (3.4) and subsequently the overall voltage drop decay curve is fitted to the bi-exponential form. As a result, all the decay curves are completely fitted to eq. (3.4) as shown in **figure 36**.

Table 3 τ_d values of $V_{solid}(t)$ and $V_{ct}(t)$ obtained from figure 36

V_a [$V_{Ag/AgCl}$]	$\tau_{d,solid}$ [1/s]	$\tau_{d,ct}$ [1/s]
-0.40	2.747	10.870
-0.45	2.525	11.765
-0.50	2.193	11.905
-0.55	2.137	12.346
-0.60	2.268	12.821
-0.65	2.597	12.195

Table 3 shows τ_d values of $V_{solid}(t)$ and $V_{ct}(t)$ obtained from the fitted curves of eq. (3.4). It is found that $\tau_{d,solid}$ is 10^{-1} times smaller than $\tau_{d,ct}$, which means $V_{ct}(t)$ decays 10 times longer than the time when $V_{solid}(t)$ decays. Therefore, the beginning part of the decay curve corresponds to $V_{solid}(t)$ and the tail part corresponds to $V_{ct}(t)$. The τ_d of each part supports the distribution of the dominant time of $V_{solid}(t)$ and $V_{ct}(t)$.

3.2.3 $V_{interface}$ in faradaic reaction

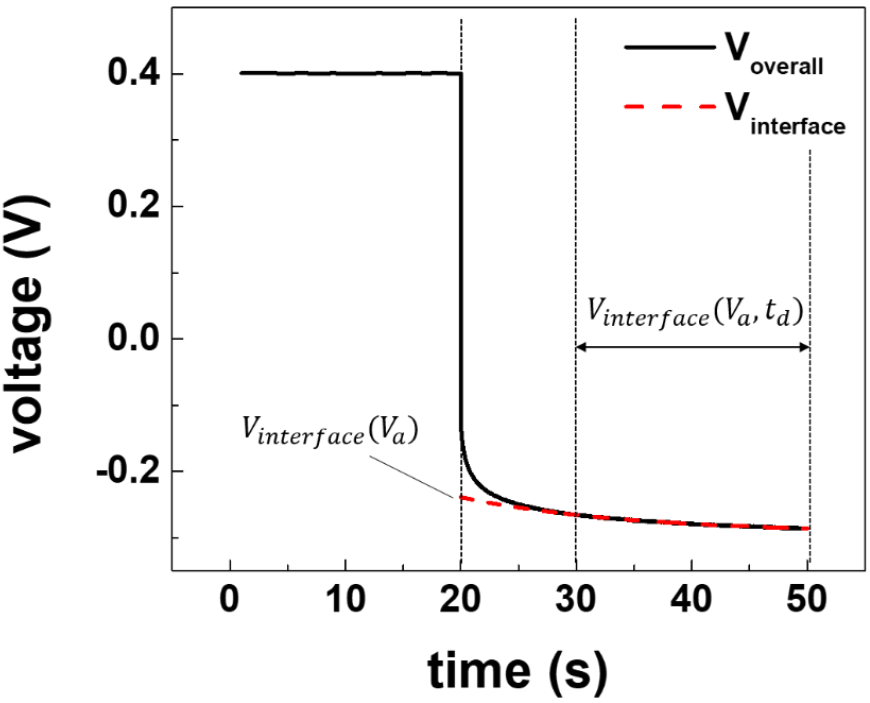

Figure 37 Voltage drop decay measurement of the TiO_2 film resulting from faradaic reaction in 0.1 M sodium phosphate buffer (pH 7) under illumination. (a: pre-exponential factor of the time-dependent $V_{interface}$, b: $V_{interface}$-dominant region)

The characteristics of the voltage drop components identified in non-faradaic reaction provide a framework for estimating the corresponding voltage drops in faradaic reaction. In the open circuit potential (OCP) decay transients of hydrogen evolution reaction (HER) on Pt, the large exchange current density enables a rapid and reversible transition between HER and hydrogen oxidation reaction (HOR), resulting in a fast OCP decay.[52]

In contrast, oxygen evolution reaction (OER) exhibits a much smaller exchange current density due to sluggish kinetics, leading to an essentially irreversible process and a markedly slower

OCP decay. Thus, the OCP decay observed in photoelectrochemical OER is primarily governed by the diffusion-driven dissipation of protons generated during the reaction.

As shown in **figure 37**, interfacial voltage drop ($V_{interface}$) becomes the predominant component after t = 30 s and exhibits a mono-exponential decay, consistent with the behavior observed in non-faradaic reaction. The time dependence of $V_{interface}$ is expressed by eq. (3.5):

$$V_{interface}(V_a, t_d) = V_{interface}(V_a)e^{-t_d/\tau} + V_{oc} \qquad (3.5)$$

According to eq. (3.5), the applied voltage (V_a)-dependent $V_{interface}$ corresponds to the pre-exponential factor at t_d = 0 s, representing the formed voltage when voltage is applied. Based on the relation, $V_{interface}$ = charge transfer voltage drop (V_{ct}) + pH-gradient voltage drop (V_{pH}) in faradaic reaction, V_{pH} is obtained by subtracting eq. (3.1) from eq. (3.5) at t_d = 0, as expressed in eq. (3.6):

$$V_{pH}(V_a) = V_{interface}(V_a, 0) - V_{ct}(V_a, 0)$$

$$= V_{interface}(V_a) - V_{ct}(V_a) \qquad (3.6)$$

Here, $V_{interface}(V_a)$ is the pre-exponential factor of the fitted curve in **figure 37**, and $V_{ct}(V_a)$ is determined from the V_{ct}-V_a relationship established in non-faradaic reaction. Accordingly, V_{pH} is expressed as $V_{interface} - 0.462V_a - 0.138$.

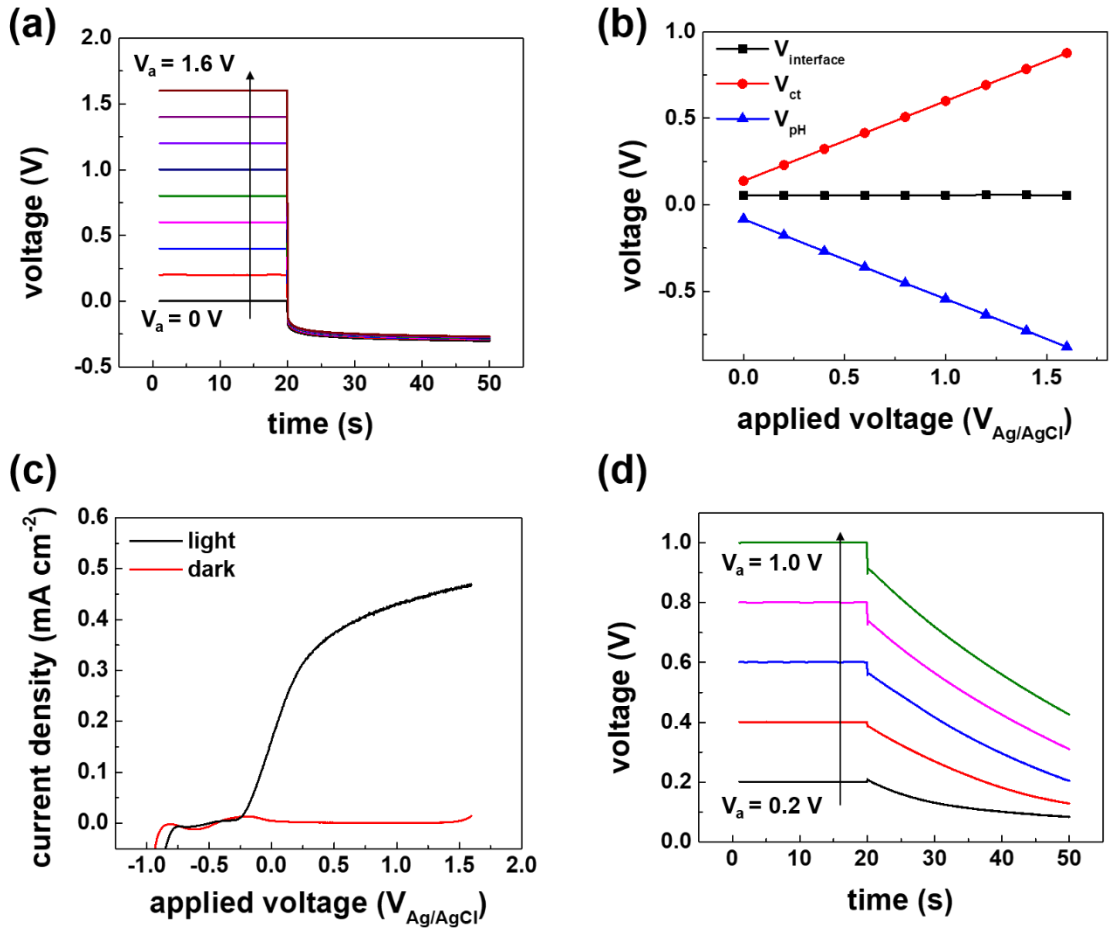

Figure 38 (a) Voltage drop decays of the TiO_2 resulting from faradaic reaction depending on applied voltage in 0.1 M sodium phosphate buffer (pH 7) under illumination and (b) estimated voltage drop components. (c) LSV measurement under illumination (black) and in dark (red), and (d) Voltage drop decays in dark with the same sample and electrolyte.

The V_{pH} values as a function of V_a are obtained by repeating the procedure described in **figure 37**, using the voltage drop decay curves shown in **figure 38(a)**. In contrast to the non-faradaic decay curves (**figure 35(a)**), the tail regions of the decay curves corresponding to eq. (3.5) overlap, indicating that the pre-exponential factors ($V_{interface}$) remain constant with respect to V_a, as shown in **figure 38(b)**. The calculated V_{pH} values decrease systematically, reflecting the subtraction of the increasing V_{ct} from the constant $V_{interface}$, consistent with the trend predicted

by eq. (1.19). This decrease is attributed to the fact that higher V_a leads to a lower pH_{final} while $pH_{initial}$ remains unchanged.

The presence of faradaic reaction is evidenced by the overlapping tail regions and the constant behavior of $V_{interface}$. When the reaction switched from faradaic to non-faradaic, the overlapping disappears. Specifically, turning off the light reduces the current density from high to near-zero values, confirming the transition from faradaic to non-faradaic behavior (**figure 38(c)**). Under dark condition, voltage drop decays measured over the same voltage range as the illuminated faradaic reaction (**figure 38(d)**) show no overlapping, indicating the absence of V_{pH} under non-faradaic condition. Additionally, the linear behavior of V_{ct} depending on V_a is validated across non-faradaic and faradaic reaction in **figure 38(b)**. Due to series connection of depletion region and Helmholtz later, the total interfacial capacitance is given by

$$\frac{1}{C_{interface}} = \frac{1}{C_{SC}} + \frac{1}{C_H} \qquad (3.7)$$

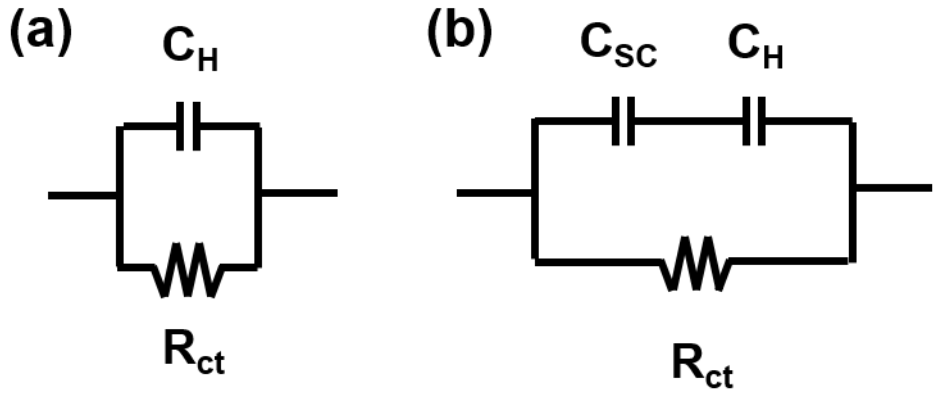

Figure 39 Equivalent circuit models representing the solid/liquid interface in (a) non-faradaic reaction and (b) faradaic reaction.

Since the V_a range for non-faradaic reaction is lower than V_{oc} (or V_{fb}), depletion region does not form and only Helmholtz later constructs the solid/liquid interface as shown in **figure 39(a)**. The total interfacial capacitance is

$$C_{interface} = C_H \qquad (3.8)$$

In contrast, the V_a range for faradaic reaction is higher than V_{fb}. Both depletion region and Helmholtz layer form at the solid/liquid interface as shown **figure 39(b)**. In faradaic reaction, the total interfacial capacitance is expressed as eq. (3.9). Voltage drop at depletion region is much larger than voltage drop at Helmholtz layer, which causes $C_H \gg C_{SC}$. In this case, $C_{interface}$ is given by

$$C_{interface} = C_{SC} \qquad (3.9)$$

Depending on non-faradaic and faradaic reaction, $C_{interface}$ is governed by either C_H or C_{SC}. However, regarding differential capacitance given by

$$C = \frac{dQ}{dV} \qquad (3.10)$$

$C_{interface}$ is constant because C_{SC} increases as much as C_H decreases and vice versa.

Figure 40 The equivalent circuit model expressed as impedance form of the model shown in figure 31(b). Z_{series}, Z_{solid} and $Z_{interface}$ are equivalent impedances representing each part of the model in figure 31(b)

As an impedance form of the circuit elements, the equivalent circuit model in **figure 31(b)** is expressed in **figure 40**. The distributed voltage drop at the solid/liquid interface is

$$V_{interface} = \frac{Z_{interface}}{Z_{series}+Z_{solid}+Z_{interface}} V_a \qquad (3.11)$$

Because all impedances are connected in series, the distributed voltage drop at the solid/liquid interface is expressed as a form of the ratio of total impedance and impedance at the interface to V_a.

3.2.4 V_{pH} estimation in various conditions with TiO_2

To validate the applicability of the developed methodology under different operating conditions, V_{pH} is evaluated at various pH levels and illumination intensities. In addition, the voltage drop components at the semiconductor/electrolyte interface such as V_{ct}, V_{pH} and $V_{interface}$ are systematically compared across these conditions, and the influence of each condition on the respective components is analyzed in this section.

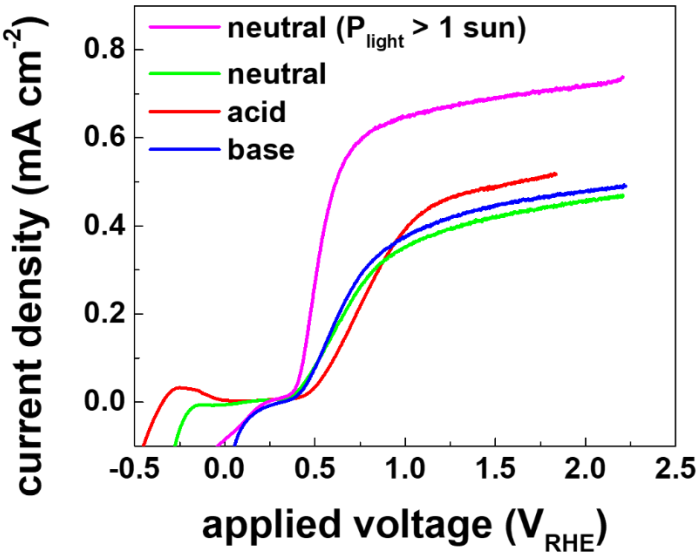

Figure 41 LSV curves of the TiO_2 in acidic (0.1 M H_2SO_4, pH 0.7), neutral (0.1 M sodium phosphate buffer, pH 7) and basic (0.1 M KOH, pH 14) under various illumination conditions (The green, red and blue curves are measured under 1 sun. Whereas the magenta curve is measured under the intensity exceeding 1 sun).

Figure 41 compares the linear weep voltammetry (LSV) curves from **figure 32(a)** with the curve measured in neutral condition under illumination intensity exceeding 1 sun. In both neutral conditions, the onset voltage remains unchanged even as light intensity increases, but the photocurrent density rises across the entire applied voltage range. Because the applied bias is identical, the higher photocurrent demonstrates that the additional charge carriers generated by enhanced light improve charge transfer at the semiconductor/electrolyte interface.[123]

To investigate the applied voltage (V_a)-dependent V_{ct} separately under acidic condition and enhanced illumination, in addition to the neutral condition at 1 sun, the V_a ranges for non-faradaic reaction are defined from the corresponding LSV curves in **figure 41**, and the voltage drop decay curves are measured as shown in **figure 42(a)** and **(b)**.

The decay curves beyond t = 30 s are fitted to eq. (3.1), which describes time-dependent V_{ct} in non-faradaic reaction, and extrapolated following the procedure in **figure 35**. From these fits, the pre-exponential factors representing the V_a-dependent V_{ct} are obtained at decay time (t_d) = 0 s and further fitted to linear equations, as presented in **figure 42(c)** and **(d)**.

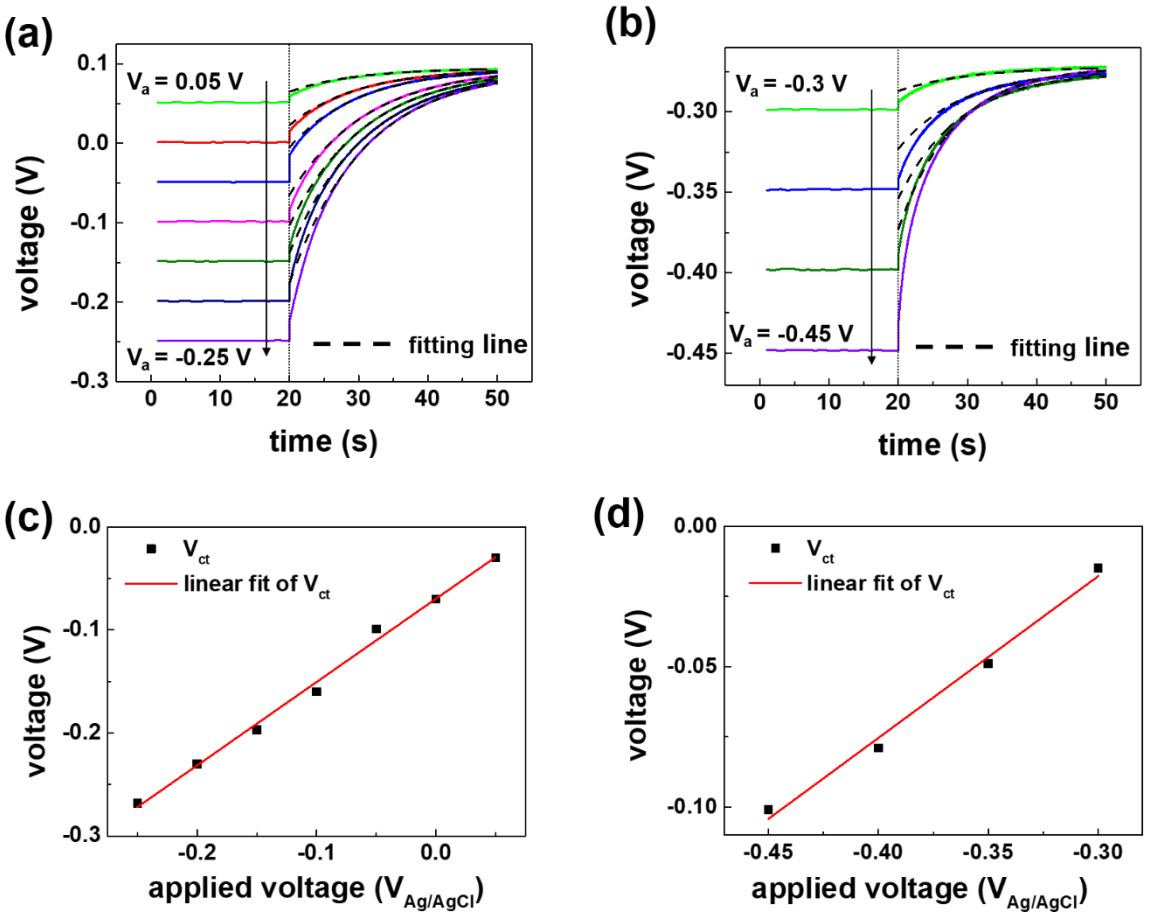

Figure 42 Voltage drop decays of the TiO_2 film resulting from non-faradaic reaction depending on applied voltage in (a) acidic (0.1 M H_2SO_4, pH 0.7) and (b) neutral (0.1 M sodium phosphate buffer, pH 7) solution under 1 sun and more than 1 sun illumination, respectively. (c) and (d) are the estimated charge transfer voltage drops of (a) and (b).

The validity of the V_a-dependent V_{ct} equations is verified by calculating open circuit voltage (V_{oc}) from the equations and comparing the values with the measured V_{oc} in **figure 42(a)** and **(b)**. The derived equations are $V_{ct} = 0.809V_a - 0.07$ under acidic condition (**figure 42(c)**) and $V_{ct} = 0.576V_a + 0.155$ under enhanced illumination (**figure 42(d)**). Substituting 0 V into V_{ct} yields calculated V_{oc} values of 0.087 V and -0.269 V, which deviates by only 0.006 V and 0.004 V, respectively, from the measured V_{oc} values.

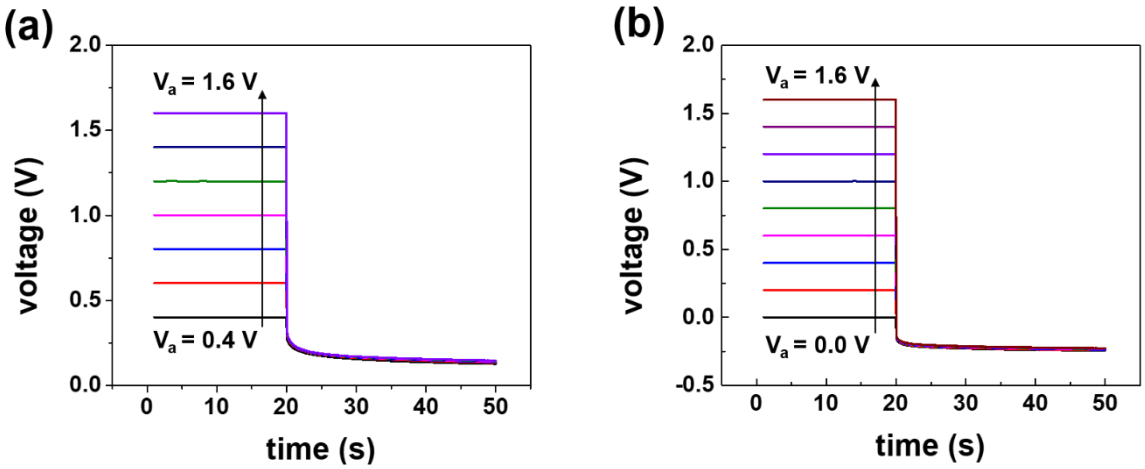

Figure 43 Voltage drop decays of the TiO_2 film resulting from faradaic reaction depending on applied voltage in (a) acidic (0.1 M H_2SO_4, pH 0.7) and (b) neutral (0.1 M sodium phosphate buffer, pH 7) solution under 1 sun and more than 1 sun illumination, respectively.

Voltage drop decay curves induced by applying the V_a ranges for faradaic reaction, as defined from the corresponding LSV curves in **figure 41**, are presented in **figure 43**. The portions of the curves after t = 30 s are fitted to eq. (3.5), which describes time-dependent $V_{interface}$ in faradaic reaction, following the same procedure in **figure 37**. From these fits, the pre-exponential factors representing the V_a-dependent $V_{interface}$ are extracted at decay time (t_d) = 0 s. Subsequently, V_{pH} is determined by subtracting the V_a-dependent V_{ct} values obtained in **figure 42** from the corresponding $V_{interface}$ values in faradaic reaction.

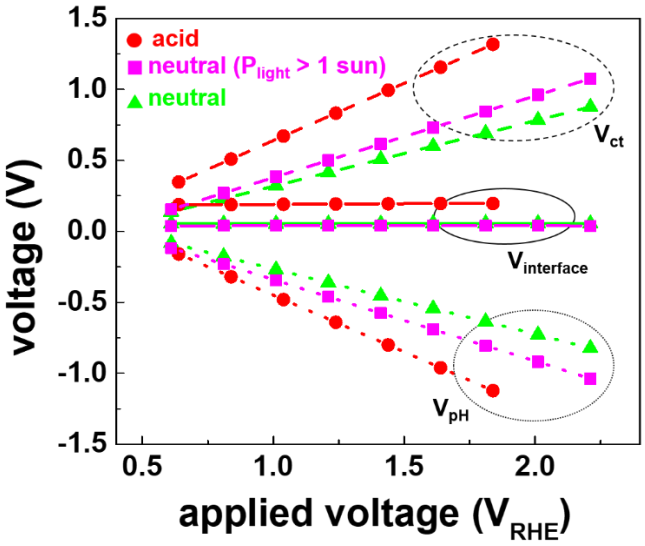

Figure 44 Voltage drop components of the PEC water splitting cell with the TiO_2 in neutral solution (0.1 M NaP_i, pH 7) under 1 sun and more than 1sun, and in acidic solution (0.1 M H_2SO_4, pH 0.7) under 1 sun.

Figure 44 compares the voltage drop components at the solid/liquid interface with respect to the reversible hydrogen electrode (V_{RHE}) under different pH levels and illumination intensities. As described in **figure 33(a)**, the weak formation of the electrical double layer in basic condition prevents the estimation of V_{ct} and V_{pH}. In contrast, the steeper slope and larger magnitudes of V_{ct} and V_{pH} observed in acidic condition compared to neutral condition are attributed to the stronger electrical double layer formation.

Although higher light intensity increases photocurrent density, indicating enhanced generation of charge carriers at the solid/liquid interface compared to the 1 sun condition (**figure 41**), both the slope and magnitude of V_{ct} and V_{pH} under neutral condition with P_{light} > 1 sun remain similar to those under neutral condition at 1 sun, and still lower than in acidic solution. This confirms that voltage formation at the solid/liquid interface is governed more by intrinsic junction

properties, such as Fermi level and redox level, than by concentration of photogenerated carriers.[124] Moreover, the symmetrical behavior of V_{ct} and V_{pH} with respect to $V_{interface}$ demonstrates that V_{pH} evolves proportionally to V_{ct}, maintaining electroneutrality at the solid/liquid interface.

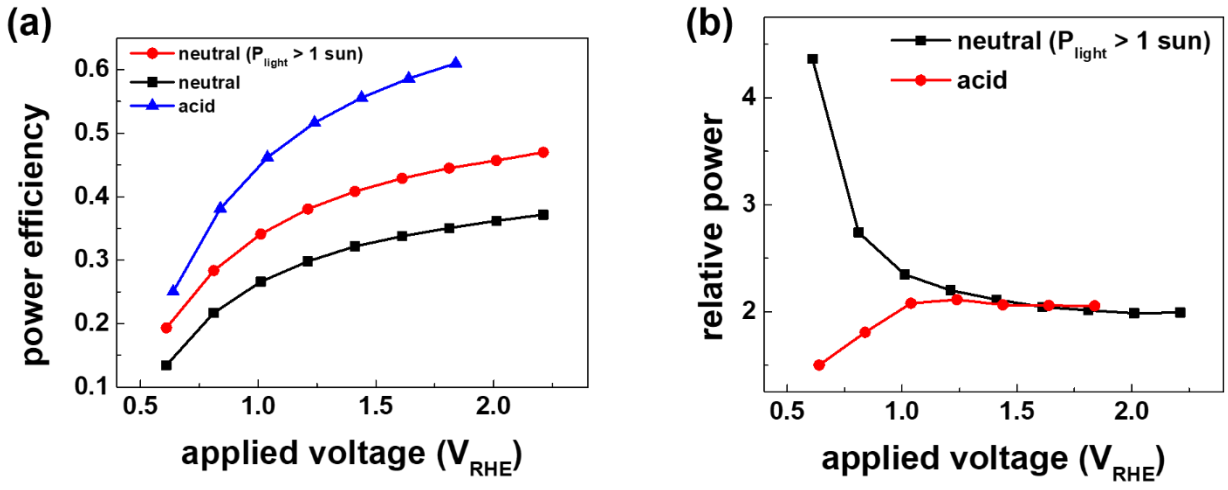

Figure 45 (a) power efficiency of PEC water splitting representing the ratio of V_{pH} to V_a and (b) Relative power of PEC water splitting, referenced to neutral electrolyte under 1 sun, comparing neutral electrolyte under P_{light} > 1 sun and acidic electrolyte under 1 sun.

Since the V_{pH} curves under neutral conditions show minimal change before and after increasing illumination intensity, the proton generation behavior appears to remain consistent. Although V_{pH} reflects proton generation during PEC water splitting and serves as a useful reaction indicator, it alone does not represent the overall catalytic performance. Therefore, a comprehensive evaluation incorporating V_{pH} and current density is required.

The interfacial power efficiency of the PEC water splitting is evaluated using the extracted V_{pH} values, as shown in **figure 45(a)**. Because the equivalent circuit consists of series-connected

voltage drop components, the power efficiency of the catalytic process is expressed as the ratio of V_{pH} to V_a

$$\text{power efficiency} = \frac{P_{output}}{P_{input}} = \frac{V_{output}(=V_{pH})I}{V_{input}(=V_a)I} \qquad (3.12)$$

Eq. (3.7) emphasize that the magnitude of V_{pH} plays a decisive role in determining power efficiency. Consequently, under acidic conditions where V_{pH} is higher than in neutral, the system exhibits the greatest efficiency across the entire range of V_a.

To further assess the impact of operating parameters, the relative power is compared as defined in eq. (3.8)

$$\text{relative power} = \frac{P_1}{P_2} = \frac{V_{1,pH}I_1}{V_{2,pH}I_2} \qquad (3.13)$$

Figure 45(b) compares the effects of illumination intensity and pH on PEC water splitting power, calculated according to eq. (3.8) and normalized to unity for the neutral condition under 1 sun illumination. Both increased illumination and decreased pH raise the relative power above 1. However, at low V_a, stronger illumination tends to reduce relative power, whereas acidic conditions enhance it.

These results demonstrate that interfacial voltage drops provide complementary insights beyond current-based parameters, which primarily describe catalytic rate. By extracting V_{pH} and V_{ct}, power is able to be determined in conjunction with current density, enabling a more device-relevant evaluation. Such analysis is crucial for practical PEC system design.[125]

3.2.5 Estimation of charge transfer voltage drop (V_{ct}) and V_{pH} using WO_3 as a photoanoode

The thermally grown WO_3 layer (the detailed synthesis is mentioned in Material and methods section) uniformly extends across the entire W metal substrate, as shown in **figure 46(a)**. The complete coverage of WO_3 ensures intimate contact between the WO_3 film and the electrolyte in the PEC water splitting cell.

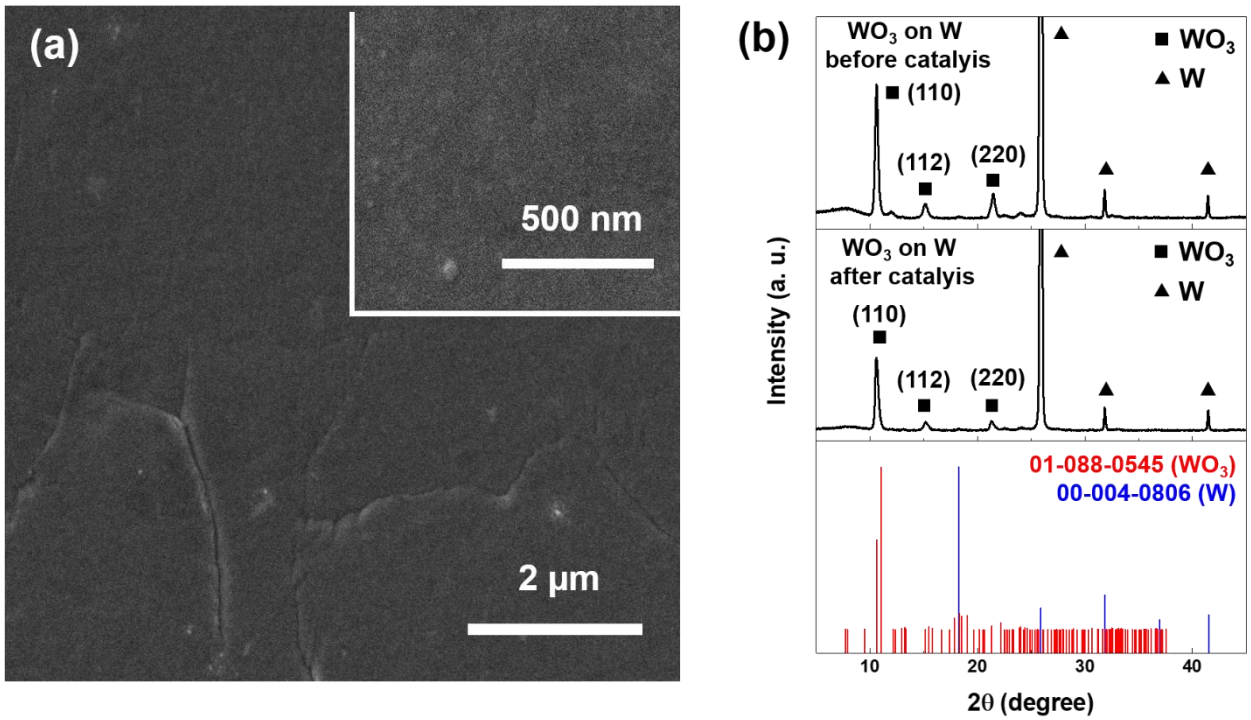

Figure 46 (a) SEM images of the synthesized WO_3 film and the enlarged image in the inset. (b) XRD patterns of the synthesized WO_3 on W metal before and after catalysis (top and middle panel, respectively) and monoclinic WO_3 reference (bottom panel). The XRD patterns in the middle panel are measured after the catalysis performed in this work.

The formed crystal structure of the synthesized WO_3 is characterized to be monoclinic WO_3, confirming that the peak in X-ray diffraction (XRD) at 11.04°, 15.51° and 22.18° correspond to (110), (112) and (220), respectively, as described in **figure 46(b)**. No evolution of any

secondary phases of other tungsten oxides (W_xO_y) indicates that there is no parasitic voltage loss resulting from phase transformation of the WO_3 during electrochemical measurements.

Charge transfer voltage drop (V_{ct}) and pH-gradient voltage drop (V_{pH}) in the photoelectrochemical (PEC) water splitting cell employing the synthesized WO_3 as the photoanode are obtained by applying the same analytical principle used for TiO_2 in the previous section. V_a ranges causing non-faradaic and faradaic reaction are identified from the linear sweep voltammetry (LSV) curve for the synthesized WO_3 measured in acidic condition (0.1 M H_2SO_4, pH 0.3) and under 1 sun illumination (**figure 47(a)**).

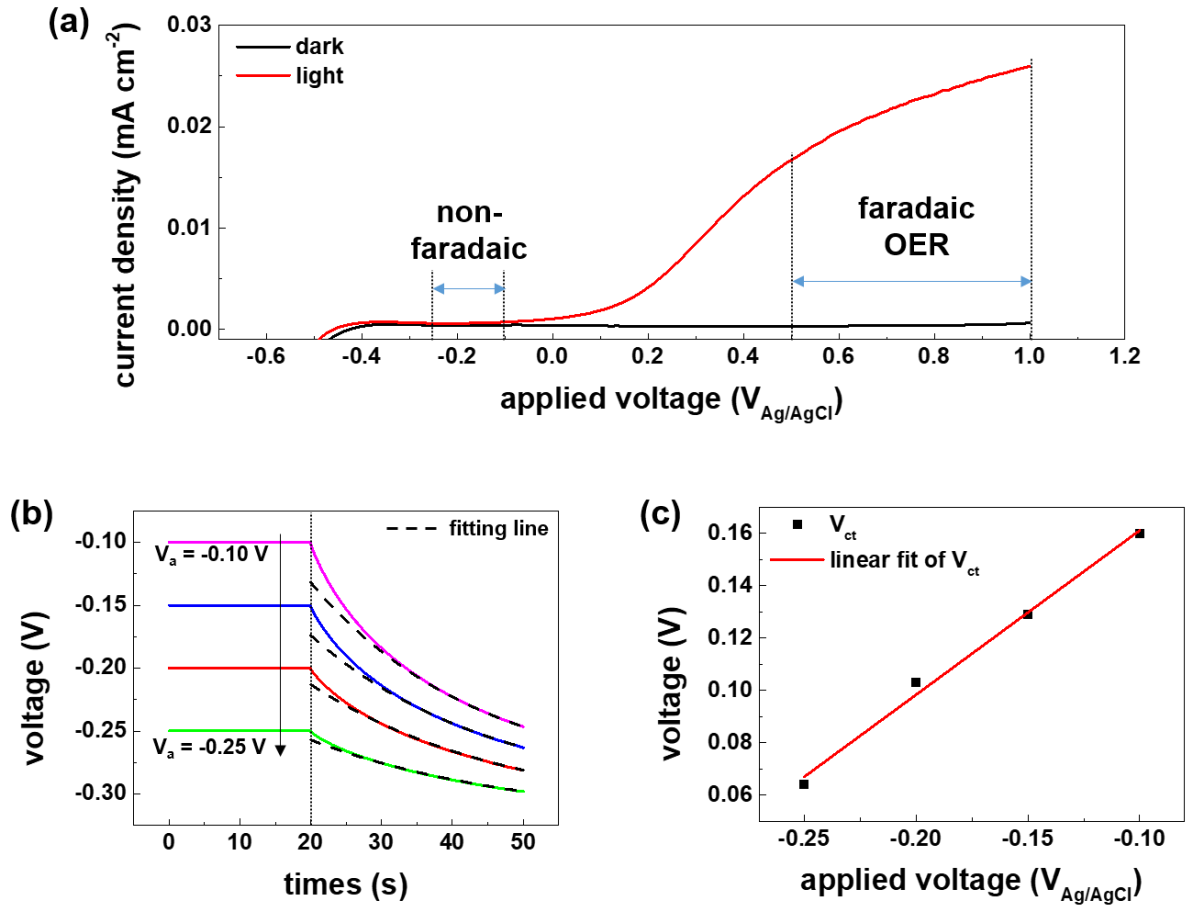

Figure 47 (a) current-voltage characteristics, (b) voltage drop decay curves resulting from non-faradaic reaction and (c) estimated V_{ct} depending on V_a of the synthesized WO_3 in 0.1 M H_2SO_4 under illumination.

After applying constant voltages for non-faradaic reaction, time-dependent overall voltage drop decay curves are measured in **figure 47(b)**. Consistent with the observations for TiO_2 (**figure 32**), the interfacial voltage drop ($V_{interface}$) becomes dominant after t = 30 s and is represented by a mono-exponential fitting line. In this region, $V_{interface}$ corresponds to V_{ct}. The pre-exponential factor obtained from each fitted curve reflects the applied voltage (V_a)-dependent V_{ct}, as shown in **figure 47(c)**. Validity of the V_a-dependent V_{ct} curve is confirmed by obtaining open circuit voltage (V_{oc}) from the linear equation, $V_{ct} = 0.628V_a + 0.224$. Since no voltage drop forms at the solid/liquid interface under open-circuit condition, meaning $V_{ct} = 0$ in the linear relationship, V_a corresponds to V_{oc}. The calculated V_{oc} of -0.357 V shows a small deviation (0.057 V) compared with the experimentally measured V_{oc} (the converged value in **figure 47(b)**), confirming the accuracy of the extracted relationship.

In contrast to the overall voltage drop decay curves for the TiO_2 in **figure 32(b-d)**, the decay curves in **figure 47(b)** are showing downward. It is attributed that the selected V_a range for non-faradaic reaction is located between the measured V_{oc} and onset potential. While applying the selected V_a range causes non-faradaic reaction based on the fact that the selected V_a range is lower than the onset potential, downward voltage drop decay curves form in discharge process because the V_a range is higher than the measured V_{oc}. In case of the TiO_2, the measured V_{oc} values (the converged values from the voltage drop decay curves in **figure 32(b-d)** and **figure 42(a-b**) are equal to the onset potentials observed in the LSV curves in **figure 32(a)** and **figure 41**. Thus, the selected V_a ranges for non-faradaic reaction are lower than the V_{oc} and the corresponding voltage drop decay curves are upward. In this way, measuring voltage drop decay curves resulting from non-faradaic reaction enables to find the relation between V_{oc} and onset potential.

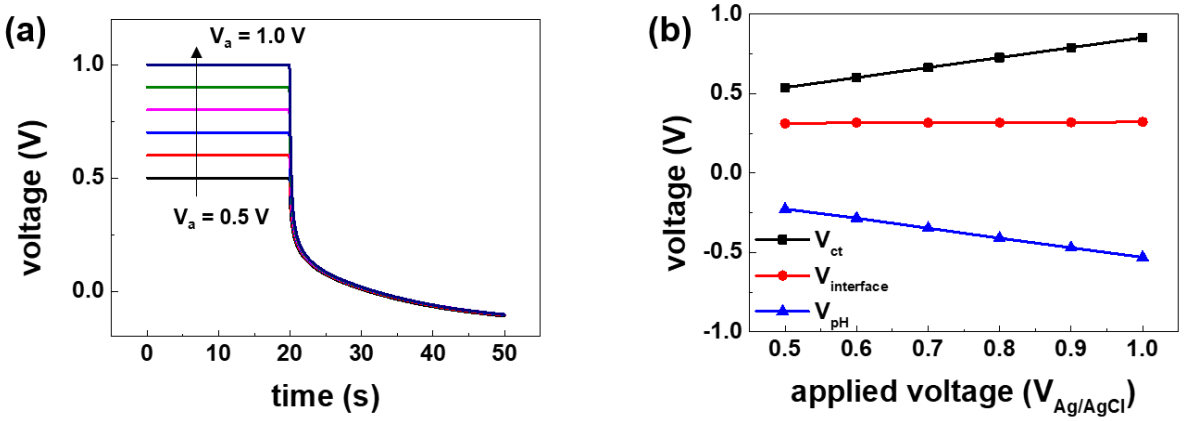

Figure 48 (a) voltage drop decay curves resulting from faradaic reaction and (b) estimated voltage drop components of the synthesized WO_3 in 0.1 M H_2SO_4 under illumination.

To investigate $V_{interface}$ in faradaic reaction, the selected V_a range for faradaic reaction in the LSV curve in **figure 47(a)** is applied and the corresponding voltage drop decay curves are measured in **figure 48(a)**. The V_a-dependent $V_{interce}$ in faradaic reaction is yielded by obtaining the pre-exponential factor of the extrapolated fitting line representing the mono-exponential form (eq. (3.5)) as performed in **figure 37**. By substituting the V_a-dependent $V_{interface}$ and V_{ct} behavior obtained in faradaic and non-faradaic reaction, respectively in eq. (3.6), V_{pH} is estimated in **figure 48(b)**. Due to the symmetry tendency of the V_{ct} and V_{pH}, the $V_{interface}$ is constant. Therefore, the developed V_{pH} and V_{ct} estimation in TiO_2 photoanode system can be applied to the WO_3 photoanode system.

4. Conclusions&Outlook

X-ray absorption spectra (XAS) and X-ray magnetic circular dichroism (XMCD) confirmed that applying an external magnetic field during chemical vapor deposition (CVD) enables modulation of cation disorder (degree of inversion) in $MgFe_2O_4$ spinel. Variations in the (400) peak intensity in X-ray diffraction (XRD) analysis served as an indicator of this degree of inversion. According to XAS and XMCD results, the reduced (400) peak intensity in $MgFe_2O_4$ grown at 0.5 T corresponds to an inverse spinel (high degree of inversion), whereas the increased intensity observed in films grown at 0 T and 1 T is consistent with a normal spinel (low degree of inversion). While the preferred growth behavior under increasing magnetic field strength reported for Fe_2O_3 (Pyeon *et al.*[32] and Stadler *et al.*[33]) was not reproduced in $MgFe_2O_4$, the (400) peak intensity decreased at 0.5 T and recovered at 1 T toward the value measured at 0 T. This resilience of the crystal structure was also reflected in the UV-vis spectra. The 0 T sample (normal spinel) showed the broadest absorption range, the 0.5 T sample exhibited significantly narrowed absorption, and the spectra broadened again at 1 T, though not fully to the level of the 0 T sample. This suggests that a 1 T magnetic field is insufficient to fully reverse the degree of inversion induced at 0.5 T.

Future work should determine whether magnetic fields stronger than 1 T can fully restore the inverse spinel back to the initial normal spinel configuration. Beyond optical characterization, it is also necessary to assess whether the tunability of the degree of inversion influences photoelectrochemical (PEC) performance. The catalytic efficiency as a function of degree of inversion can further be examined using the developed method for estimating the pH-gradient voltage drop (V_{pH}).

One of the major advantages of the pH-gradient voltage drop, V_{pH} and charge transfer voltage drop, V_{ct} estimation method proposed in this work is that interfacial characteristics is

quantitatively analyzed only through electrochemical measurements, without requiring any additional instrumentation, as discussed in the introduction part. The voltage drop decay curves, also referred to as open-circuit potential (OCP) decay, are readily obtained by applying a bias that induces either non-faradaic or faradaic reaction, followed by recording the transient response under open circuit condition. Accurate interpretation of these decay curves requires careful consideration of the voltage drop components defined in the equivalent circuit model.

The key assumption for estimating V_{pH} and V_{ct} is that the decay profiles of voltage drop at semiconductor bulk (V_{solid}) and interfacial voltage drop ($V_{interface}$) in the overall voltage drop decay curve must be separable. In a PEC water splitting system, absorbed incident photons generate electron-hole pairs, which are subsequently separated under applied bias, even across the bulk region of the semiconductor. Once the bias is removed, these photogenerated charge carriers begin to redistribute to reach equilibrium, undergoing recombination according to their respective lieftimes. During this process the voltage drop formed by the external bias gradually dissipates. The decay rate of V_{solid} is governed by the mobility of electron in the semiconductor. Simultaneously, the $V_{interface}$ begins to decay once the bias is removed. Although this semiconductor/electrolyte interface involves both the semiconductor and electrolyte phases, the rate of decay is influenced by the diffusion of ionic species in the electrolyte, whose mobility is significantly lower than that of electron in the solid. Under illumination, the charge redistribution within the semiconductor becomes more pronounced due to the carrier lifetime associated with recombination. In contrast, during electrocatalytic oxygen evolution reaction (OER) where photogeneration does not occur, such recombination-driven dynamics are absent. Consequently, clear separation between V_{solid} and $V_{interface}$ components in the voltage decay curve is not expected. This behavior is evident in **figure 38(b)**, where the potential range corresponding to faradaic reaction is switched to non-faradaic range after the illumination is

turned off. The resulting voltage decay curves exhibit an elongated, indistinct exponential profile, indicating overlap between the dominant regions of V_{solid} and $V_{interface}$.

Estimation of V_{pH} and V_{ct} provides a pathway toward evaluating the power efficiency required for scaling PEC water splitting system. Conventional metrics such as faradaic efficiency and incident photon-to-current efficiency express catalytic rate but do not capture the power efficiency between input power and output power. For practical device implementation, this power efficiency becomes critical as a catalyst that delivers high current density may still be unsuitable if its power efficiency is low. Overall, this study demonstrates that simultaneous determination of V_{pH} and V_{ct} offers an effective means to identify optimal operating conditions in PEC water splitting, including applied bias, illumination intensity and electrolyte pH.

5. Methods and materials

5.1 Synthesis of [Mg{Fe(O^{t}Bu)$_4$}$_2$] precursor

The precursor synthesis was carried out under an inert atmosphere (nitrogen gas) using a *Stock* glass vacuum line. All used reagents were used without further purification and the solvents were freshly distilled over sodium. TG analysis was performed by a TG/DSC1 (Mettler Toledo GmbH, Germany) apparatus using nitrogen gas and a heating rate of 10 °C/min.

[Fe(O^{t}Bu)$_3$]$_2$: A suspension of anhydrous $FeCl_3$ (5.78 g, 36 mmol) in dry toluene (50 mL) was cooled using liquid nitrogen and dry THF (150 mL) was slowly added. After the mixture was thawing, a solution of fresh sublimed KO^{t}Bu (12.09 g, 108 mmol) in dry THF (150 mL) was added and the suspension was stirred for 24 h at 80 °C. The solvent was removed under reduced pressure and the product was obtained after sublimation at 90 °C in vacuo ($p = 10^{-2}$ mbar) as a green solid, yielding 7.15 g (26 mmol, 72%). Molar mass of the [Fe(O^{t}Bu)$_3$]$_2$ compound is calculated to be 550.38 g mol^{-1}.

[Mg{Fe(O^{t}Bu)$_4$}$_2$]: For the synthesis of [Mg{Fe(O^{t}Bu)$_4$}$_2$], KO^{t}Bu (2.0 equivalents of [Fe(O^{t}Bu)$_3$]$_2$) in dry THF (25 mL) was added to a solution of [Fe(O^{t}Bu)$_3$]$_2$ (1.23 g, 2.24 mmol) in 40 mL toluene. Afterward, anhydrous $MgCl_2$ (0.11 g, 1.12 mmol) in 25 mL dry THF was added and the reaction was stirred overnight at 70 °C. The formed KCl was removed by extraction with pentane (2x15 mL) and the product was obtained as a green-yellow solid by sublimation ($T_{sublimation}$ = 140 °C, $p = 10^{-2}$ mbar). Molar mass of the [Mg{Fe(O^{t}Bu)$_4$}$_2$] precursor is 720.38 g mol^{-1}.

5.2 magnetic field-assisted chemical vapor deposition

To investigate the effect of an external magnetic field on the growth of $MgFe_2O_4$ thin films, a magnetic field-assisted chemical vapor deposition (mfCVD) system was constructed as shown in **figure 49**. For the deposition of $MgFe_2O_4$ films, a cold-wall system with an external horizontal magnetic field (2×2 cm^2, DC current), produced by an electromagnet (MagMess EM- 2), was used. FTO substrates (1 cm x 1.5 cm) were heated to 500 ℃ using a DC Joule heater and 100 mg of the precursor in a 10 mL flask was implemented by a glass flange into the system.

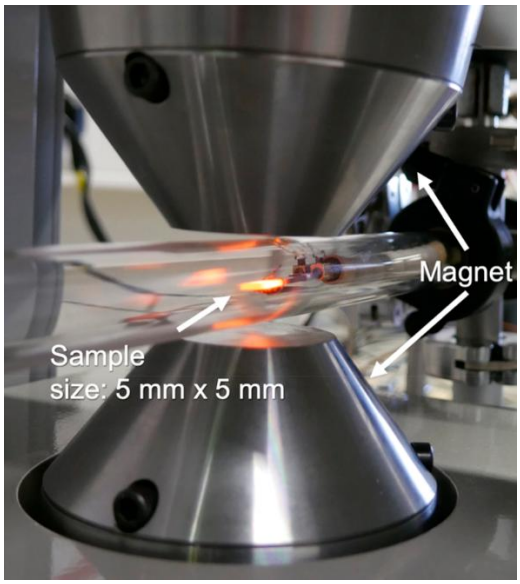

Figure 49 A photograph of magnetic field-assisted chemical vapor deposition setup. Adapted from ref. [126].

The deposition was performed by a precursor temperature of 180 ℃ and a deposition time of 20 min. During film deposition, the precursor flux of $[MgFe_2(O^tBu)_8]$ was directed toward the substrate while the electromagnets applied a magnetic field. The external magnetic field was maintained until the substrate cooled to room temperature. This deposition process was repeated under varying magnetic field intensities.

5.3 Physicochemical characterization of the $MgFe_2O_4$ films

The X-Ray diffraction characterization of the synthesized powders and films was measured on a STOE diffractometer with STADI MP system (Cu Kα= 1.54178 Å, 40 kV, 40 mA). FIB-SEM images of MFO films were measured using a Strata Dual Beam 235 from FEI. Chemical analysis of the surfaces was performed by using X-Ray Photoelectron Spectroscopy (XPS) utilizing an ESCA M-Probe spectrometer from SSI (Surface Science Instruments), which is equipped with a monochromatic Al Kα (1486.6 eV) X-Ray source. All recorded spectra were referent to a binding energy of 284.8 eV based on the C 1s signal from adventitious carbon. Compositional calculations were performed using CasaXPS. X-ray absorption spectra (XAS) and X-ray magnetic circular dichroism (XMCD) were recorded with synchrotron radiation (BESSY-II, HZB) and normalized typically with the two-point method (at the far lowest and highest energy points of each edge).

5.4 Photoanodes TiO_2 and WO_3 synthesis and characterization

Fluorine-doped tin oxide (FTO) substrates were sequentially cleaned in acetone, ethanol and deionized (DI) water using an ultrasonicator for 10 min in each solvent, followed by drying under a stream of N_2 gas. A TiO_2 layer was deposited onto the FTO via a hydrothermal method. For the precursor solution, 30 mL of hydrochloric acid (HCl, 37%), 30 mL of DI water and 3 mL of titanium butoxide ($C_6H_{36}O_4Ti$, 97%) were mixed and stirred for 5 min. The FTO substrate was then placed in a Teflon-lined autoclave containing 30 mL of the precursor solution. The autoclave was heated at 150 ℃ for 30 min and allowed to cool naturally to room temperature. The treated substrate was rinsed with DI water and subsequently annealed in air at 500 ℃ for 3 h.

Tungsten (W) metal substrates were sequentially cleaned in acetone, ethanol and deionized (DI) water using an ultrasonicator for 10 min in each solvent, followed by drying under a stream of N_2 gas. Subsequently, the substrates were annealed at 500 ℃ for 3 h to grow WO_3 layer.

The crystal structure was characterized using X-ray diffraction (XRD, STADI MP, STOE) with a Mo-Kα radiation source. The surface morphology was observed by a field-emission scanning electron microscope (Zeiss, Sigma 300 VP Rise).

5.5 Electrochemical measurements

Photoelectrochemical measurements were performed using a potentiostat (VersaSTAT 4, AMETEK) in combination with a solar simulator (Newport, model 66902) providing an illumination intensity of 100 mW cm^{-2} with an AM 1.5G filter.

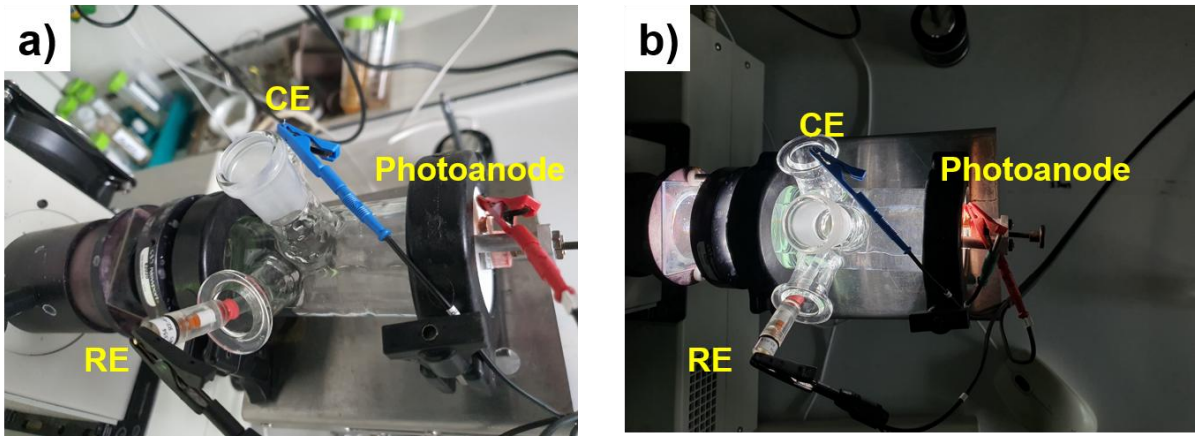

Figure 50 Photographs of PEC water splitting cells (a) without and (b) with illumination.

A conventional three-electrode configuration was employed, consisting of the synthesized TiO_2 and WO_3 photoanode, a Pt coil counter electrode (CE), and an Ag/AgCl reference electrode (RE) in **figure 50**. Electrolytes included 0.1 M H_2SO_4 (pH 0.3), 0.1 M KOH (pH 13), and a sodium phosphate buffer solution (pH 7) prepared from 0.1 M NaH_2PO_4 and 0.1 M

$Na_2HPO_4 \cdot 3H_2O$. Linear sweep voltammetry (LSV) curves were recorded at a scan rate of 50 mV s^{-1}, and voltage drop decay transients were measured with a detection interval of 0.01 s.

6. References

[1] M. Balat, *Int. J. Hydrogen Energy* **2008**, *33*, 4013–4029.

[2] V. Dhiman, S. Singh, V. Srivastava, S. Garg, A. D. Saran, *Environ. Sci. Pollut. Res.* **2025**, *32*, 13299–13312.

[3] V. Ramanathan, Y. Feng, *Atmos. Environ.* **2009**, *43*, 37–50.

[4] W. He, X. Li, C. Tang, S. Zhou, X. Lu, W. Li, X. Li, X. Zeng, **2023**, DOI 10.1021/acsnano.3c08450.

[5] H. Hu, X. Wang, J. P. Attfield, M. Yang, *Chem. Soc. Rev.* **2024**, *53*, 163–203.

[6] S. Vitta, *RSC Sustain.* **2024**, *2*, 3202–3221.

[7] J. Chi, H. Yu, *Cuihua Xuebao/Chinese J. Catal.* **2018**, *39*, 390–394.

[8] L. Lin, K. Wei, X. Wang, W. Ma, C. Bian, J. Ge, *J. Mater. Chem. A* **2024**, *12*, 17958–17972.

[9] Akira Fujishima, Kenichi Honda, *Nature* **1972**, *238*, 37–38.

[10] K. Lee, A. Mazare, P. Schmuki, *Chem. Rev.* **2014**, *114*, 9385-9454

[11] W. H. Lee, C. W. Lee, G. D. Cha, B. H. Lee, J. H. Jeong, H. Park, J. Heo, M. S. Bootharaju, S. H. Sunwoo, J. H. Kim, K. H. Ahn, D. H. Kim, T. Hyeon, *Nat. Nanotechnol.* **2023**, *18*, 754–762.

[12] H. Song, C. Li, Z. Lou, Z. Ye, L. Zhu, **2017**, DOI 10.1021/acssuschemeng.7b01774.

[13] T. Hisatomi, K. Takanabe, K. Domen, *Catal. Letters* **2015**, *145*, 95–108.

[14] Y. Yan, C. Liu, H. Jian, X. Cheng, T. Hu, D. Wang, L. Shang, G. Chen, P. Schaaf, X. Wang, E. Kan, T. Zhang, *Adv. Funct. Mater.* **2021**, *2009610*, 1–13.

[15] J. Wei, M. Zhou, A. Long, Y. Xue, H. Liao, C. Wei, Z. J. Xu, *Nano-Micro Lett.* **2018**, *10*, 1–15.

[16] T. Kosaka, Y. Teduka, T. Ogura, Y. Zhou, T. Hisatomi, H. Nishiyama, K. Domen, Y. Takahashi, H. Onishi, *ACS Catal.* **2020**, *10*, 13159–13164.

[17] Q. Li, H. Meng, P. Zhou, Y. Zheng, J. Wang, J. Yu, J. Gong, *ACS Catal.* **2013**, *3*, 882-889

[18] G. Zhou, M. Li, Y. Li, H. Dong, D. Sun, X. Liu, L. Xu, Z. Tian, Y. Tang, *Adv. Funct. Mater.* **2020**, *30*, 1–8.

[19] X. Li, S. Guo, C. Kan, J. Zhu, T. Tong, S. Ke, W.C.H. Choy, B. Wei, *Nano Energy*, **2016**, *30*, 549–558.

[20] D. Yokoyama, H. Hashiguchi, K. Maeda, T. Minegishi, T. Takata, *Thin Solid Films* **2011**, *519*, 2087–2092.

[21] G. Segev, H. Dotan, K. D. Malviya, A. Kay, M. T. Mayer, M. Grätzel, A. Rothschild, *Adv. Energy Mater.* **2016**, *6*, 1–7.

[22] S. Nurul, F. Moridon, M. Ikhmal, M. Azuwa, K. Arifin, *Int. J. Hydrogen Energy* **2019**, *44*, 25495–25504.

[23] S. Corby, L. Francàs, A. Kafizas, J. R. Durrant, *Chem. Sci.* **2020**, *11*, 2907–2914.

[24] Y. Makimizu, J. E. Yoo, M. Poornajar, N. T. Nguyen, H. J. Ahn, I. Hwang, S. Kment, P. Schmuki, *J. Mater. Chem. A* **2020**, *8*, 1315–1325.

[25] B. S. Kalanoor, H. Seo, S. S. Kalanur, *Mater. Sci. Energy Technol.* **2018**, *1*, 49–62.

[26] C. Liu, Y. Yang, J. Li, S. Chen, W. Li, X. Tang, *Chem. Eng. J.* **2017**, *326*, 603–611.

[27] K. Hatagami, F. Kishimoto, Y. Kawase, T. Higashi, V. Nandal, K. Seki, K. Takanabe, *Energy Technol.* **2022**, *10*, DOI 10.1002/ente.202100570.

[28] H. H. Huang, K. Obata, F. Kishimoto, K. Takanabe, *Mater. Adv.* **2022**, *3*, 9009–9018.

[29] P. Cendula, M. T. Mayer, J. Luo, M. Grätzel, *Sustain. Energy Fuels* **2019**, *3*, 2633–2641.

[30] Y. Park, K. J. Mc Donald, K. S. Choi, *Chem. Soc. Rev.* **2013**, *42*, 2321–2337.

[31] E. Park, S. S. Patil, H. Lee, V. S. Kumbhar, K. Lee, *Nanoscale* **2021**, *13*, 16932–16941.

[32] M. Pyeon, V. Rauch, D. Stadler, M. Gürsoy, M. Deo, Y. Gönüllü, T. Fischer, T. Hwang, S. Mathur, *Adv. Eng. Mater.* **2019**, *21*, 1–8.

[33] D. Stadler, T. Brede, D. Schwarzbach, F. Maccari, T. Fischer, O. Gutfleisch, C. A. Volkert, S. Mathur, *Nanoscale Adv.* **2019**, *1*, 4290–4295.

[34] W. Fan, M. Li, H. Bai, D. Xu, C. Chen, C. Li, Y. Ge, W. Shi, *Langmuir* **2016**, *32*, 1629–1636.

[35] P. Heidari, S. M. Masoudpanah, *J. Mater. Res. Technol.* **2020**, *9*, 4469–4475.

[36] D. S. Mathew, R. S. Juang, *Chem. Eng. J.* **2007**, *129*, 51–65.

[37] T. S. Herng, W. Xiao, S. M. Poh, F. He, R. Sutarto, X. Zhu, R. Li, X. Yin, C. Diao, Y. Yang, X. Huang, X. Yu, Y. P. Feng, A. Rusydi, J. Ding, *Nano Res.* **2015**, *8*, 2935–2945.

[38] E. K. Fodjo, K. M. Gabriel, B. Y. Serge, D. Li, C. Kong, A. Trokourey, *Chem. Cent. J.* **2017**, *11*, 1–9.

[39] V. Šepelák, K. Tkáčová, V. V. Boldyrev, S. Wißmann, K. D. Becker, *Phys. B Condens. Matter* **1997**, *234–236*, 617–619.

[40] X. Zhu, N. Guijarro, Y. Liu, P. Schouwink, R. A. Wells, F. Le Formal, S. Sun, C. Gao, K. Sivula, *Adv. Mater.* **2018**, *1801612*, 1–6.

[41] A. Bloesser, H. Kurz, J. Timm, F. Wittkamp, C. Simon, S. Hayama, B. Weber, U. P. Apfel, R. Marschall, *ACS Appl. Nano Mater.* **2020**, *3*, 11587–11599.

[42] R. Fan, S. Cheng, G. Huang, Y. Wang, Y. Zhang, S. Vanka, G. A. Botton, Z. Mi, M. Shen, *J. Mater. Chem. A* **2019**, *7*, 2200–2209.

[43] K. Oh, C. Mériadec, B. Lassalle-Kaiser, V. Dorcet, B. Fabre, S. Ababou-Girard, L. Joanny, F. Gouttefangeas, G. Loget, *Energy Environ. Sci.* **2018**, *11*, 2590–2599.

[44] W. Zheng, *ACS Energy Lett.* **2023**, *8*, 1952–1958.

[45] S. Anantharaj, S. Noda, *ChemElectroChem* **2020**, *7*, 2297–2308.

[46] S. Anantharaj, S. Noda, *J. Mater. Chem. A* **2022**, *10*, 9348–9354.

[47] S. Ravishankar, Z. Liu, Y. Wang, T. Kirchartz, U. Rau, *PRX Energy* **2023**, *2*, 1.

[48] S. Ravishankar, J. Bisquert, T. Kirchartz, *Chem. Sci.* **2022**, *13*, 4828–4837.

[49] S. Ravishankar, Z. Liu, U. Rau, T. Kirchartz, *PRX Energy* **2022**, *1*, 1.

[50] S. Ravishankar, L. Kruppa, S. Jenatsch, G. Yan, Y. Wang, *Energy Environ. Sci.* **2023**, *17*, 1229–1243.

[51] J. C. Fornaciari, L. Weng, S. M. Alia, C. Zhan, T. Anh, A. T. Bell, T. Ogitsu, N. Danilovic, A. Z. Weber, **2022**, *405*, DOI 10.1016/j.electacta.2021.139810.

[52] E. R. Sauvé, B. Y. Tang, N. K. Razdan, W. L. Toh, S. Weng, Y. Surendranath, *Joule*

2024, *8*, 728–745.

[53] Z. Wang, C. Li, K. Domen, *Chem. Soc. Rev.* **2019**, *48*, 2109–2125.

[54] Z. P. Ifkovits, J. M. Evans, M. C. Meier, K. M. Papadantonakis, N. S. Lewis, *Energy Environ. Sci.* **2021**, *14*, 4740–4759.

[55] F. F. Abdi, R. R. Gutierrez Perez, S. Haussener, *Sustain. Energy Fuels* **2020**, *4*, 2734–2740.

[56] M. C. O. Monteiro, X. Liu, B. J. L. Hagedoorn, D. D. Snabilié, M. T. M. Koper, *ChemElectroChem* **2022**, *9*, DOI 10.1002/celc.202101223.

[57] T. Hatsukade, M. Zorko, D. Haering, N. M. Markovic, *Electrochem. commun.* **2020**, *120*, 106785.

[58] B. Lei, D. Xu, B. Wei, T. Xie, C. Xiao, W. Jin, L. Xu, *ACS Appl. Mater. Interfaces* **2021**, *13*, 4785–4795.

[59] K. Obata, R. Van De Krol, M. Schwarze, R. Schomäcker, F. F. Abdi, *Energy Environ. Sci.* **2020**, *13*, 5104–5116.

[60] J. Cheng, M. Sprik, *Phys. Chem. Chem. Phys.* **2012**, *14*, 11245–11267.

[61] M. F. Lichterman, S. Hu, M. H. Richter, E. J. Crumlin, S. Axnanda, M. Favaro, W. Drisdell, Z. Hussain, T. Mayer, B. S. Brunschwig, N. S. Lewis, Z. Liu, H. J. Lewerenz, *Energy Environ. Sci.* **2015**, *8*, 2409–2416.

[62] T. Mayer, K. Schwanitz, B. Kaiser, A. Hajduk, M. V. Lebedev, W. Jaegermann, *J. Electron Spectros. Relat. Phenomena* **2017**, *221*, 116–133.

[63] A. J. Nozik, *J. Phys. Chem.* **1996**, *3654*, 13061–13078.

[64] S. Kumar, K. Ojha, A. K. Ganguli, *Adv. Mater. Interfaces* **2017**, *4*, DOI 10.1002/admi.201600981.

[65] M. Kumar, B. Meena, P. Subramanyam, D. Suryakala, C. Subrahmanyam, *NPG Asia Mater.* **2022**, *14*, DOI 10.1038/s41427-022-00436-x.

[66] R. Li, Y. Y. Wang, S. Weng, Z. Cai, S. B. Cronin, *ACS Electrochem.* **2025**, DOI 10.1021/acselectrochem.5c00156.

[67] K. Schwarzburg, F. Willig, *J. Phys. Chem. B* **1997**, *101*, 2451–2458.

[68] T. T. Hien, N. D. Quang, C. Kim, D. Kim, *Nano Energy* **2019**, *57*, 660–669.

[69] C. Ampelli, C. Genovese, G. Centi, R. Passalacqua, S. Perathoner, *Top. Catal.* **2016**, *59*, 757–771.

[70] A. Hankin, F. E. Bedoya-Lora, J. C. Alexander, A. Regoutz, G. H. Kelsall, *J. Mater. Chem. A* **2019**, *7*, 26162–26176.

[71] B. Miao, A. Iqbal, K. H. Bevan, *J. Phys. Chem. C* **2019**, *123*, 28593–28603.

[72] L. M. Peter, K. G. Upul Wijayantha, *ChemPhysChem* **2014**, *15*, 1983–1995.

[73] S. Saremi-Yarahmadi, K. G. U. Wijayantha, A. A. Tahir, B. Vaidhyanathan, *J. Phys. Chem. C* **2009**, *113*, 4768–4778.

[74] K. Sivula, *ACS Energy Lett.* **2021**, *6*, 2549–2551.

[75] W. J. Albery, G. J. O'Shea, A. L. Smith, *J. Chem. Soc. - Faraday Trans.* **1996**, *92*, 4083–4085.

[76] P. Cendula, S. David Tilley, S. Gimenez, J. Bisquert, M. Schmid, M. Grätzel, J. O. Schumacher, *J. Phys. Chem. C* **2014**, *118*, 29599–29607.

[77] P. Cendula, F. E. Bedoya-Lora, R. R. Prabhakar, *ACS Appl. Energy Mater.* **2022**, *5*, 14593–14604.

[78] H. Wang, Y. Xia, H. Li, X. Wang, Y. Yu, X. Jiao, D. Chen, *Nat. Commun.* **2020**, *11*, 1–11.

[79] T. Lana Villarreal, R. Gómez, M. Neumann-Spallart, N. Alonso-Vante, P. Salvador, *J. Phys. Chem. B* **2004**, *108*, 15172–15181.

[80] T. L. Villarreal, R. Gómez, M. González, P. Salvador, *J. Phys. Chem. B* **2004**, *108*, 20278–20290.

[81] A. T. Garcia-Esparza, K. Takanabe, *J. Mater. Chem. A* **2016**, *4*, 2894–2908.

[82] L. Bertoluzzi, P. Lopez-Varo, J. A. Jiménez Tejada, J. Bisquert, *J. Mater. Chem. A* **2016**, *4*, 2873–2879.

[83] L. Bertoluzzi, J. Bisquert, *J. Phys. Chem. Lett.* **2017**, *8*, 172–180.

[84] L. Bertoluzzi, J. Bisquert, *J. Phys. Chem. Lett.* **2012**, *3*, 2517–2522.

[85] E. Nurlaela, Y. Sasaki, M. Nakabayashi, N. Shibata, T. Yamada, K. Domen, *J. Mater. Chem. A* **2018**, *6*, 15265–15273.

[86] J. Reichman, *Appl. Phys. Lett.* **1980**, *36*, 574–577.

[87] P. Cendula, P. P. Sahoo, G. Cibira, P. Simon, *J. Phys. Chem. C* **2020**, *124*, 1269–1276.

[88] P. Cendula, A. Sancheti, P. Simon, *Adv. Theory Simulations* **2021**, *4*, 1–6.

[89] W. W. Gärtner, *Phys. Rev.* **1959**, *116*, 84–87.

[90] H. Zhang, H. Wang, J. Xuan, *J. Power Sources* **2020**, *462*, 228113.

[91] A. R. Zeradjanin, I. Spanos, J. Masa, M. Rohwerder, R. Schlögl, *J. Solid State*

Electrochem. **2021**, *25*, 33–42.

[92] K. Otake, H. Kitagawa, *Small* **2021**, *2006189*, 1–17.

[93] G. Karmakar, A. Tyagi, A. Y. Shah, *Coord. Chem. Rev.* **2024**, *504*, 215665.

[94] S. Mathur, C. Cavelius, H. Shen, *Zeitschrift fur Anorg. und Allg. Chemie* **2009**, *635*, 2106–2111.

[95] M. Veith, M. Haas, V. Huch, *Chem. Mater.* **2005**, *17*, 95–101.

[96] C. Gatel, B. Warot-Fonrose, S. Matzen, J. B. Moussy, *Appl. Phys. Lett.* **2013**, *103*, 092405.

[97] S. Mathur, C. Cavelius, K. Moh, H. Shen, J. Bauer, *Zeitschrift fur Anorg. und Allg. Chemie* **2009**, *635*, 898–902.

[98] H. Lu, D. S. Wright, S. D. Pike, *Chem. Commun.* **2020**, *56*, 854–871.

[99] V. Nahrstedt, D. Stadler, T. Fischer, T. Duchoň, D. N. Mueller, C. M. Schneider, S. Mathur, *Inorg. Chem.* **2021**, *60*, 3719–3728.

[100] J. Sun, Q. B. Wen, T. Li, L. Wiehl, C. Fasel, Y. Feng, D. De Carolis, Z. J. Yu, Q. G. Fu, R. Riedel, *J. Am. Ceram. Soc.* **2020**, *103*, 1436–1445.

[101] A. Jamil, J. Schläfer, Y. Gönüllü, A. Lepcha, S. Mathur, *Cryst. Growth Des.* **2016**, *16*, 5260–5267.

[102] M. Catauro, I. Blanco, D. Naviglio, G. D. Poggetto, *Macromol. Symp.* **2021**, *395*, 2000197(1)-2000197(3).

[103] B. Singh, T. Fischer, *J. Mater. Chem. A* **2025**, *13*, 20104–20142.

[104] M. C. Biesinger, B. P. Payne, A. P. Grosvenor, L. W. M. Lau, A. R. Gerson, R. S. C.

Smart, *Appl. Surf. Sci.* **2011**, *257*, 2717–2730.

[105] L. I. Granone, A. C. Ulpe, L. Robben, D. S. Klimke, M. Jahns, F. Renz, T. M. Gesing, D. T. Bredow, R. Dillert, D. W. Bahnemann, *Phys. Chem. Chem. Phys.* **2018**, *20*, 28267–28278.

[106] D. Barreca, G. Carraro, A. Gasparotto, C. Maccato, M. E. A. Warwick, K. Kaunisto, C. Sada, S. Turner, Y. Gönüllü, T. P. Ruoko, L. Borgese, E. Bontempi, G. Van Tendeloo, H. Lemmetyinen, S. Mathur, *Adv. Mater. Interfaces* **2015**, *2*, 1–11.

[107] A. Mettenbörger, Y. Gönüllü, T. Fischer, T. Heisig, A. Sasinska, C. Maccato, G. Carraro, C. Sada, D. Barreca, L. Mayrhofer, M. Moseler, A. Held, S. Mathur, *Nano Energy* **2016**, *19*, 415–427.

[108] A. J. Cowan, J. Tang, W. Leng, J. R. Durrant, D. R. Klug, *J. Phys. Chem. C* **2010**, *114*, 4208–4214.

[109] J. Ma, K. Oh, G. Tagliabue, *J. Phys. Chem. C* **2023**, *127*, 11–21.

[110] T. Luttrell, S. Halpegamage, J. Tao, A. Kramer, E. Sutter, M. Batzill, *Sci. Rep.* **2015**, *4*, 1–8.

[111] K. J. Kim, K. D. Benkstein, J. Van de Lagemaat, A. J. Frank, *Chem. Mater.* **2002**, *14*, 1042–1047.

[112] N. Park, J. Van De Lagemaat, A. J. Frank, *J. Phys. Chem. B* **2000**, *104*, 8989–8994.

[113] B. Liu, Z. Jin, L. Bai, J. Liang, Q. Zhang, N. Wang, C. Liu, C. Wei, Y. Zhao, X. Zhang, *J. Mater. Chem. A* **2016**, *4*, 14204–14212.

[114] A. Tsyganok, P. Monroy-Castillero, Y. Piekner, A. Yochelis, A. Rothschild, *Energy Environ. Sci.* **2022**, *15*, 2445–2459.

[115] J. U. Kim, H. S. Han, J. Park, W. Park, J. H. Baek, J. M. Lee, H. S. Jung, I. S. Cho, *J. Catal.* **2018**, *365*, 138–144.

[116] Z. S. Pourbakhsh, K. Mohammadi, A. Moshaii, M. Azimzadehirani, A. Hosseinmardi, *RSC Adv.* **2019**, *9*, 31860–31866.

[117] S. Anantharaj, S. Noda, M. Driess, P. W. Menezes, *ACS Energy Lett.* **2021**, *6*, 1607–1611.

[118] N. M. Vuong, D. Kim, H. Kim, **2013**, DOI 10.1039/C3TC30157E.

[119] P. S. Archana, R. Jose, C. Vijila, S. Ramakrishna, *J. Phys. Chem. C* **2009**, *113*, 21538–21542.

[120] K. Obata, F. F. Abdi, *Sustain. Energy Fuels* **2021**, *5*, 3791–3801.

[121] A. Hankin, F. E. Bedoya-Lora, J. C. Alexander, A. Regoutz, G. H. Kelsall, *J. Mater. Chem. A* **2019**, *7*, 26162–26176.

[122] F. Le Formal, N. Tétreault, M. Cornuz, T. Moehl, M. Grätzel, K. Sivula, *Chem. Sci.* **2011**, *2*, 737–743.

[123] K. G. Upul Wijayantha, S. Saremi-Yarahmadi, L. M. Peter, *Phys. Chem. Chem. Phys.* **2011**, *13*, 5264–5270.

[124] F. Le Formal, K. Sivula, M. Grätzel, *J. Phys. Chem. C* **2012**, *116*, 26707–26720.

[125] O. Astakhov, T. Cibaka, L. Wieprecht, U. Rau, T. Merdzhanova, *ChemSusChem* **2025**, *18*, DOI 10.1002/cssc.202402027.

[126] D. Stadler, D. N. Mueller, T. Brede, T. Duchon, T. Fischer, A. Sarkar, M. Giesen, C. M. Schneider, C. A. Volkert, S. Mathur, *J. Phys. Chem. Lett.* **2019**, *10*, 6253-6259